ABSTRACT

Title of dissertation: MICROSCOPIC REARRANGEMENTS WITHIN GRANULAR SHEAR FLOWS: SEGREGATION, SUBDIFFUSION, & ROTATION

Matthew John Harrington
Doctor of Philosophy, 2015

Dissertation directed by: Professor Wolfgang Losert
Department of Physics

Granular materials constitute a class of complex systems that can exhibit global behaviors that are reminiscent of solids, liquids, gases, or otherwise uniquely their own. The macroscopic size of individual grains tends to render the standard tools of thermodynamics and statistical mechanics inapplicable, while opening the possibility of directly measuring and probing individual particle motion. This thesis details three investigations in which the characterization of microscopic motion provides a bridge to understanding bulk phenomena.

The first study explores size-segregation in a cyclically shear-driven granular system, as observed using the refractive index matched scanning (RIMS) technique for three-dimensional (3D) imaging. While convective flows are implicated in many granular segregation processes, the associated particle-scale rearrangements are not well understood. A bidisperse mixture segregates under steady shear, but the cyclically driven system either remains mixed or segregates slowly. Individual grain

motion shows no signs of particle-scale segregation dynamics that precede bulk segregation. Instead, we find that the transition from non-segregating to segregating flow is accompanied by significantly less reversible particle trajectories, and the emergence of a convective flow field.

A granular system undergoing cyclic forcing is also seen to undergo subdiffusion beneath some threshold shear amplitude. The transition from subdiffusive to diffusive motion is rigorously tested in a simulated two-dimensional (2D) granular system. Motion in the subdiffusive regime is also seen to exhibit some behavior reminiscent of cage-breaking models, which had developed in the context of thermal systems. However, analysis of local displacements of a grain relative to its cage of neighbors reveals key distinctions from thermal systems.

Finally, we have made progress in the measurement of rotational motion of individual grains. While 2D experimental systems readily yield both translational and rotational motion, a challenge in 3D experiments is the tracking of rotational motion of spherically symmetric particles. We propose an extension of the RIMS technique as a method of simultaneously measuring particle-scale translation and rotation. Partial measurements of 3D rotations indicate that shear-driven rotational motion may stem from gear-like motion within the shear zone. This suggests that the prevalence of collective rotation between grains can play a significant role in dictating bulk phenomena such as reversibility and segregation.

MICROSCOPIC REARRANGEMENTS WITHIN GRANULAR SHEAR FLOWS: SEGREGATION, SUBDIFFUSION, & ROTATION

by

Matthew John Harrington

Dissertation submitted to the Faculty of the Graduate School of the
University of Maryland, College Park in partial fulfillment
of the requirements for the degree of
Doctor of Philosophy
2015

Advisory Committee:
Professor Wolfgang Losert, Chair/Advisor
Professor Michelle Girvan
Professor Edward Ott
Professor Christine Hartzell
Professor Derek Richardson, Dean's Representative

Preface

The content of this thesis is based on the following publications:

- **M. Harrington**, J.H. Weijs, and W. Losert, "Suppression and Emergence of Granular Segregation under Cyclic Shear," *Physical Review Letters* **111**, 078001 (2013).

- M. Mailman, **M. Harrington**, M. Girvan, and W. Losert, "Consequences of Anomalous Diffusion in Disordered Systems under Cyclic Forcing," *Physical Review Letters* **112**, 228001 (2014).

- **M. Harrington**, M. Lin, K.N. Nordstrom, and W. Losert, "Experimental measurements of orientation and rotation of dense 3D packings of spheres," *Granular Matter* **16**, 185-191 (2014).

Dedication

This dissertation is dedicated to Sister Catherine Martinelle "K-Mart" Harrington, OP, on the occasion of her 100th birthday.

Acknowledgments

No man is an island entire of itself; every man is a piece of the continent, a part of the main. —"Meditation XVII," John Donne

I must begin by acknowledging the contributions from my advisor and committee chair, Professor Wolfgang Losert. As a first-year graduate student, Professor Losert was willing to offer me the opportunity to join his granular group, along with the challenge of quickly rising to senior graduate student in the lab. Professor Losert's background and expertise has been invaluable to every aspect of my graduate training, from research design and analysis, to publications and presentations, to teaching and education.

I am also grateful to the other members of my committee, Professors Michelle Girvan, Edward Ott, Christine Hartzell, and Derek Richardson, who have been very gracious with their time and attention to ensure that this dissertation is completed to the very best of my ability.

As a member of Professor Losert's granular lab, I had the great fortune of working with bright, constructive, and diligent colleagues: postdoctoral researchers Mitch Mailman and Kerstin Nordstrom, graduate students Mark Herrera, Steven Slotterback, and Miguel González-Pinto, and undergraduate students Michael Lin, Emily Lim, Allyson Rice, and Shola Wylie. Collectively, they have taught me a great deal about the basics of granular physics, offered assistance with use of the lab equipment, and given important feedback on experiments, data, papers, talks, and posters.

I would also like to acknowledge the members of Professor Losert's biophysics lab. They provided helpful comments on my research and were willing to share lab equipment, particularly coffee. In addition, I would like to thank the Physics Education Research Group for giving me a second home during the latter portion of my graduate career, as well as valuable training and experience in teaching.

My research at the Institute for Research in Electronics and Applied Physics (IREAP) could not have been done without its incredible staff, especially Don Martin and Nolan Ballew who provided the necessary assistance and instruction that allowed the experiments to happen. I would also like to acknowledge Ed Condon who quickly responded to any technical issues with our computers.

I would be remiss to not include the staff in the Department of Physics, who have been instrumental in planning my graduate academic career, as well as readily addressing any questions and concerns that arose. In particular, I would like to thank former Program Assistants Jane Hessing and Linda O'Hara.

Financial support for the research presented in this dissertation came from the National Science Foundation (NSF) and the Defense Threat Reduction Agency (DTRA). I also received support from the Chateaubriand Fellowship from the Embassy of France in the US, Rennes Métropole, the Thomas Mason Fellowship for Interdisciplinary Research, and the National Institutes of Health BRAIN Initiative.

Lastly, above all of the supportive people and entities listed above, I could not have reached the conclusion of my doctoral studies without the unconditional love and support from my family: my father, Michael, my mother, Lana, and my sisters, Elizabeth and Amanda.

Table of Contents

List of Figures

List of Abbreviations

2D	Two-dimensional
3D	Three-dimensional
BNE	Brazil Nut Effect
CA	Cellular Automata
CCD	Charge-coupled Device
CTRW	Continuous-time Random Walk
DTRA	Defense Threat Reduction Agency
FBM	Fractional Brownian Motion
FTP	Fractional Time Process
IREAP	Institute for Research in Electronics and Applied Physics
MD	Molecular Dynamics
mMSD	Modified Mean-squared Displacement
MSD	Mean-squared Displacement
NSF	National Science Foundation
PCA	Principal Component Analysis
PDF	Probability Distribution Function
PIV	Particle Image Velocimetry
PMMA	Polymethyl Methacrylate
PTV	Particle Tracking Velocimetry
RIMS	Refractive Index Matched Scanning

Chapter 1

Introduction

Despite the ubiquity of granular materials in both nature and industry, much of the physics that drives their behavior is still not well understood. While there has been a great deal of progress in precisely understanding the behavior of typical solids, liquids, and gases, the same cannot be said of granular materials. Simply put, grains that are relatively large compared to molecules behave very differently on the microscopic scale (or particle-scale). This renders many of the analytic tools and models developed in the context of, for instance, molecules that exhibit thermal motion, difficult to apply to granular materials. An incomplete characterization of particle-scale dynamics makes the task of developing governing equations for granular materials virtually impossible.

This thesis summarizes studies that have been performed to better characterize the microscopic picture of granular flows. Specifically, this thesis describes particle-scale dynamics that have been observed to accompany segregation and subdiffusion. In addition, this thesis highlights progress toward characterizing three-dimensional (3D) rotational motion, allowing for the ability to characterize every mode of individual grain motion. This work was carried out using both experimental techniques and analysis of simulated systems.

In this chapter, the basic physics of granular materials are discussed, along

with other important definitions. This will provide background and motivation for the studies to be described in later chapters.

1.1 Motivation & Overview

A granular material, loosely speaking, is an ensemble comprised of many macroscopic discrete elements, which shall be referred to from here on as "grains." Granular materials constitute one of the most common classes of materials that people encounter in their everyday lives. Some common examples include the coffee beans we handle while preparing breakfast, the rice we cook for lunch or dinner, and the sand and pebbles all along our beaches and shores. Granular materials are also found in a wide variety of industrial settings, such as the manufacturing of pharmaceuticals, home insulation, and the production, storage, and transport of food.

In fact, granular materials are so commonplace, that some may overlook some of their unique behaviors and characteristics. This can lead to undesirable effects or, worse yet, catastrophic events. In late December 2014, the Morton salt company in Chicago had an accident at a storage facility, the aftermath of which is shown in Figure 1.1. A large pile of salt had burst through one of the walls, spilling salt out of the building and onto a parking lot belonging to a neighboring car dealership. This accident left the company with wasted inventory and property damage for both Morton and the car dealership.

However, some insights into physics of granular materials could have prevented

such an accident from occurring. Consider the hydrostatic pressure from a typical fluid. This pressure grows linearly with depth into the fluid and at a given depth, the pressure is the same through the fluid. However, pressure within a confined granular material tends to be strongest near the walls, away from the center of the container [1]. This is due to anisotropic force chains, which connect grains in contact with other in strings and cascade throughout the material, often terminating at the containing walls. In the case of the Morton salt plant, the salt pile was allowed to be built too high and the wall of the building could no longer contain the vast amount of pressure. Unfortunately, similar accidents are not uncommon and tend to happen to grain silos that are also packed beyond their structural capacity.

Recently, the study of granular materials has generated interest within academic fields outside of physics and engineering, which tend to constitute the traditional granular community. In particular, granular materials found in astrophysical applications is a sector of the field that has drawn burgeoning interest from many researchers, both those already established within the granular community and those who have crossed over from astronomy. A well-known example of an astrophysical granular material is regolith, the fine powder that provides the outer coating of asteroids, moons, and planets. A very recent discovery of astrophysical granular materials came from Rosetta's *Philae* probe, after it made its historic landing on comet C67P/Churyumov-Gerasimenko in November 2014. Shown in Figure 1.2, one can see not only that the comet appears to be covered with regolith just like asteroids, but it also has periodic dunes [2], similar to those found in the salt pile at the Morton plant. In fact, the formation of dunes is a very well known observation

Figure 1.1: The aftermath of a December 2014 accident at a Morton Salt building in Chicago, IL. Pressure emanating from a tall salt pile caused one of the walls to collapse, spilling salt onto cars belonging to a neighboring dealership. (Photo Credit: Zbigniew Bzdak, Chicago Tribune)

in granular materials [3].

This is just one example of reproducible behavior that is seen in granular materials across diverse applications. In order to better understand other common phenomena, we must describe in more detail some of the basic and defining traits of granular materials.

1.2 Physical Properties of Granular Materials

Up to this point, much of the background provided on granular materials has been very colloquial and anecdotal. Given the scientific interest in these materials and how they behave, there must be a more specific way of classifying granular materials.

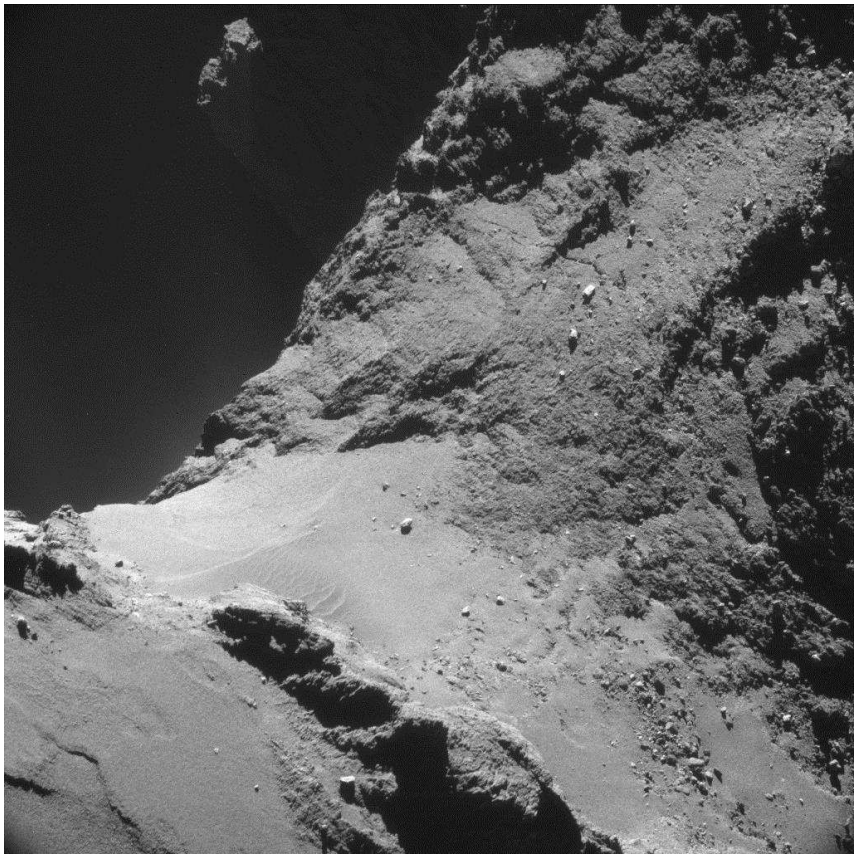

Figure 1.2: An image of the surface of comet 67P captured by *Philae*. This picture reveals what appear to be periodic dunes within the region covered by fine regolith. (Photo Credit: European Space Agency)

Fortunately, there are several specific defining characteristics that distinguish granular materials from other forms of matter. For one, the particle size, described previously as being macroscopic, must be large enough so that thermal fluctuations from its surrounding environment are negligible, implying that grains are athermal [4]. A quantitative way of describing this is that the work required to move one grain a distance equal to its diameter (hereafter referred to as a "grain diameter") against gravity must be much greater than characteristic thermal energies of its environment,

$$mgD \gg k_B T \tag{1.1}$$

where m is the mass of the grain, g is the gravitational field strength, D is the grain diameter, T is the temperature of the surroundings, and k_B is the Boltzmann constant. Consider a spherical polymethyl methacrylate (PMMA) bead of diameter 5 mm. These characteristics are chosen because they are similar to those of the experimental granular materials studied in this thesis. The work required to move one PMMA sphere of this size one grain diameter against gravity is of order 10^{-6} J. Meanwhile, thermal energies at room temperature, 300 K, are of order 10^{-21}, a difference of 15 orders of magnitude. In order for these two quantities to be comparable, one would need a PMMA grain diameter of about 1 μm. For grains composed of various glasses, plastics, and metals, a lower limit for D of about 10 μm is typical.

Another defining property is that grains primarily interact with each other

via repulsive contact forces. When grains collide or slide against each other, the interaction is always dissipative and inelastic. When granular materials are dry they are completely noncohesive with no attractive forces, perhaps except for electric forces resulting from triboelectric charging between grains [5].

1.3 Granular Phenomena

In the field of materials science, the defining properties of granular materials make them a unique class of material of their own with distinct and reproducible phenomena. Temperature does not play a role in how each grain behaves, in the sense that motion caused by collisions with thermal molecules in the surrounding environment is negligible. However, granular materials can, as a whole, behave similar to solids, liquids, and gases. This has led to several studies that explore the apparent phase transition between fluid-like and solid-like states, a so-called jamming transition [6], which has recently been expanded to include scenarios in which driving forces actually enhance jamming [7].

Ultimately, whether a granular material stands as a rigid structure or exhibits fluid-like flow depends heavily on the local structures formed by individual grains. This motivates the need to study granular materials not just at the aggregate scale, but with particular consideration of how individual grains influence each other on the microscopic scale. An important characteristic of microscopic motion is whether grains overall move in a reversible, or elastic, fashion, or if they tend to exhibit irreversible plastic deformations. The notion of microscopic reversibility is especially

apparent when considering any scenario in which a granular material is driven by some cyclic boundary force.

To provide further motivation for the work described in this thesis, two particular phenomena that arise from characteristics of microscopic (ir)reversibility are described in further detail below: segregation and compaction.

1.3.1 Granular Segregation

Segregation in the context of granular materials is defined as the spontaneous separation of granular mixtures by size and/or mass when driven by some kind of force [8]. At first glance, this seems to be counter-intuitive to the second law of thermodynamics, where entropy should tend to increase within a statistical ensemble, suggesting that the granular material should become increasingly mixed over time. However, one must recall that temperature, in the traditional sense, is effectively zero for granular materials, so the standard laws and techniques from statistical mechanics and thermodynamics no longer apply.

Segregation is widely observed in many natural and industrial settings, often leaving an undesired effect where the material becomes less mixed than before. A common result found in several systems is the so-called Brazil Nut Effect (BNE), named after the tendency of large grains to rise to the top of a shaken container of various sized grains [9]. This phenomenon is often associated with the presence of a convective flow of surrounding grains [10].

In fact, segregation and the BNE have even been observed in astrophysical

environments. Figure 1.2 shows that particle sizes on the surface of comet 67P vary greatly, from the fine powders that exhibit patterned dunes, to larger rocks and boulders. Similar distributions in size can also be found on the surface of the asteroid Itokawa, shown in Figure 1.3, where observed grain diameters range from order 1 cm to 10 m. Given the arrangement of large boulders upon fine powders, it is supposed that seismic vibrations, induced by impact, thermal cycling, and tidal forces, provide the primary mechanism for regolith to sort itself by size [11].

While it is impractical to actually track the motion of every grain of regolith on the surface of an asteroid or comet, segregation can overall be better understood, for instance, through experiments performed on Earth. While much of the local motion within a system that segregates under vibration is understood, the same cannot be said of dense shear-driven systems. Continuum gradient-based models have been proposed [12, 13, 14, 15], but do not account for convective flows that may be present within the system. Furthermore, while our understanding of vibro-excited segregation stems directly from cyclic forcing, the same attention has not given to cyclic shearing, in which kinetic gradients dictating segregation are invariant, while microscopic motion may become reversible [16, 17].

1.3.2 Compaction

When perturbed in a cyclic manner, granular materials may compact and settle into an increasingly confined state [18, 19]. The density of grains within their available space, or volume fraction, provides a direct measurement of the degree to

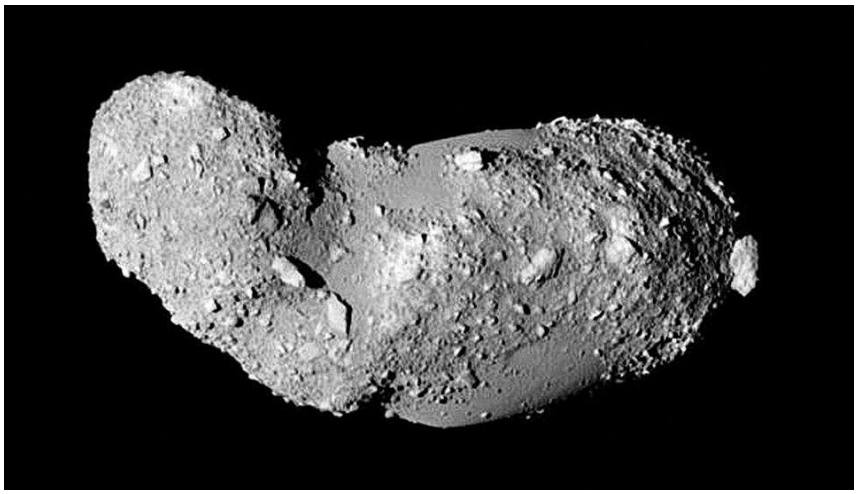

Figure 1.3: An image of the surface of the asteroid Itokawa captured by *Hayabusa*, showing regolith of various sizes distributed throughout. In particular, large boulders are found to primarily lay at the outer surface, on top of fine powders. (Photo Credit: Japanese Aerospace Exploration Agency)

which the material as a whole has compacted. Grains that are more closely packed together tend to behave more as a solid, which has important consequences for industry and infrastructure.

For instance, railroad ties are laid upon a ballast, which is a collection of rocks and minerals providing support for the ties, tracks, and occasional train that passes by. In order to provide a smooth, safe ride for the train, the ballast should be optimally compacted so that the bed does not significantly rearrange due to cyclic forcing from the weight of the train itself [20]. After a bed of ballast is laid down, it must be regularly maintained, which includes the use of a tamping machine, shown in Figure 1.4. This machine works by periodically inserting metal arms into the ballast and then drawing them back out, causing the rocks to tend to settle

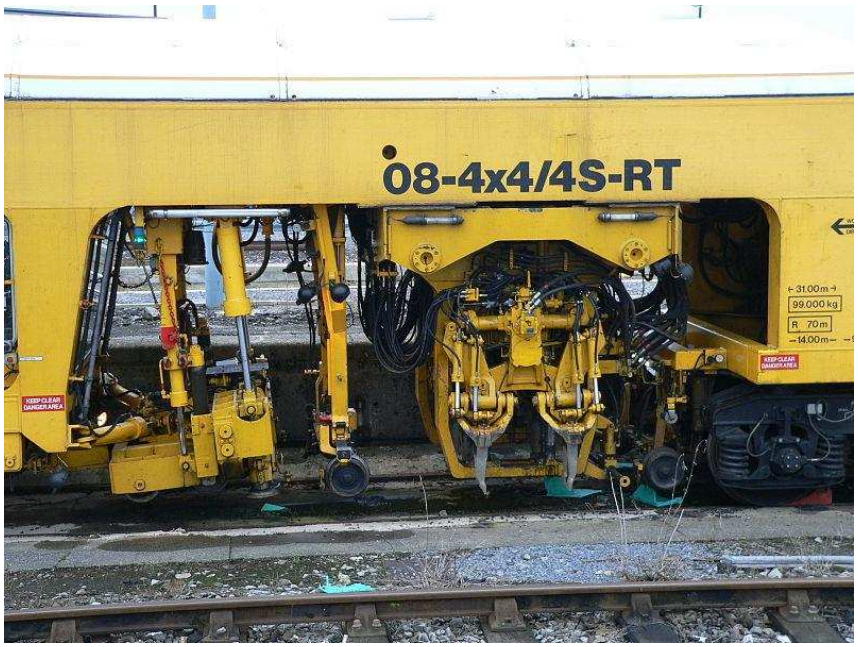

Figure 1.4: Plasser & Theurer 08-4x4/4S-RT Unimat 08-RT, a particular tamping machine model used for maintaining compacted track ballast. The material is driven by cyclic insertion and withdrawal of the metal arms found at the bottom of the machine. (Photo Credit: Chris McKenna)

downward.

A practical question to consider is that when using the tamping machine, how deep must the arms go to make sure the bed is maximally compacted? Also, what are properties to look for in the selection of a material to constitute a ballast? Such questions can be addressed by considering the combination of subdiffusive dynamics and particle-scale rotation, which can provide a microscopic basis for the macroscopic effect of a compacted material.

An ensemble exhibiting subdiffusion is one in which the constitutive elements have a mean-squared displacement (MSD) that varies with time as t^{β}, where $0 <$

$\beta < 1$. Systems that evolve subdiffusively include various complex and disordered systems [21], both driven [17, 22, 23] and active [24, 25]. When particle displacements grow as a power law that is weaker than linear, this indicates caged or confined motion. This could certainly be the case for a dense granular material, in which an individual grain motion can be confined by its nearest neighbors, particularly when grain trajectories are reversible under cyclic forcing. This is in stark contrast to truly diffusive (or random) systems which have MSDs that grow in a linear fashion with time.

Subdiffusion directly lends a mechanism for how translational motion is frustrated under compaction. However, another component that should be considered, given the macroscopic size requirement of granular materials, is how rotational motion is suppressed during compaction. It stands to reason that the structure of the contact network, that is, the topology of contact forces that grains exert on each other within a packing, can either facilitate or frustrate rotational motion. In particular, if an even number of frictional grains constitute a force loop, this can allow for gear-like motion, in which all grains cooperatively rotate with each other. On the other hand, force loops of odd numbers will necessarily have at least one sliding contact, possibly restricting rotational motion [26, 27]. In a real granular system, one can expect to find loops of both kinds, so one must also consider their spatial configuration to determine overall co-rotation and/or frustration.

There has also been some work to incorporate particle-scale rotations into generic models of granular flow. One approach uses the concepts of couple stresses, as proposed for continuous solids [28], but applied to granular systems [29, 30].

Couple stresses are typically ignored in elementary continuum mechanics [31], but they can provide a mechanism for internal rotations within a disordered system. Another approach is to model the granular material as a da Vinci fluid, in which solid friction provides a basis for fluid dissipation [32]. From here, there has also been interest in obtaining experimental measurements of particle-scale rotations, with which the validity of these models can be tested.

1.4 Scope of Thesis

Chapter 2 discusses techniques that are used by researchers to study granular materials at the microscopic scale, both experimentally and theoretically. A brief synopsis of various methods will be provided, with emphasis placed on the particular methods used in the studies discussed in later chapters.

Chapter 3 presents a study performed on size segregation in a granular material undergoing cyclic circular split-bottom shear. 3D images are captured using the refractive index matched scanning (RIMS) technique, which allows for the tracking of individual grains. We observe that, while a bidisperse system continually undergoes segregation when shear is applied in a constant direction, the same is not necessarily true when the shear is applied in an oscillatory manner. The bulk phenomena of segregation is also tied with distinct features of microscopic reversibility and convective flow.

Chapter 4 further explores the behavior of a cyclically shear-driven system, in the context of simulations where crossover behavior can be probed over several shear

amplitudes. A 2D bidisperse system of frictionless disks is generated and sheared using a molecular dynamics package. While segregation is not present in the absence of gravity, we find other distinct crossover behaviors, such as the transition from subdiffusive to diffusive motion with increasing shear amplitude. In the subdiffusive regime, grain motion can be described fairly well using a thermal cage-breaking model, but with key differences that are elucidated by a metric that extracts grain motion relative to its nearest neighbors.

Chapter 5 returns to an experimental study, where additional modifications to the RIMS technique allow for the study of granular rotational motion. In the context of 3D experiments, capturing characteristics of rotational motion is virtually impossible when using spherical grains. However, we have successfully taken measurements of a portion of particle-scale rotational motion in order to explore the prevalence of rolling within the fully developed shear-band.

Chapter 6 discusses progress toward measuring the full rotational motion of individual grains, and the difficulties inherent in terms of both imaging and analysis. Comparatively, translational motion is much easier to probe using 3D granular data. The desire to measure all rotational degrees of freedom has called for additional modifications to the experimental set-up, as well as new image-processing and analysis tools.

Finally, chapter 7 discusses additional future work that can be done to further the insights described in this thesis. This includes work that can be done with both experiments and simulations.

Chapter 2

Techniques for Granular Materials Research

This chapter discusses techniques that are used in experimental and theoretical studies of granular materials. Given the highly complex nature of granular materials, there are a wealth of approaches and apparatus that are used, so this is not intended to be a comprehensive list. Instead, this chapter focuses on techniques that are most relevant for characterizing particle scale motion in granular flows. The particular techniques that are used in the studies discussed in the thesis will be noted and emphasized.

2.1 Experimental Techniques

Many experimental studies of granular materials focus on bulk properties of a flowing granular material. A very common example of this is the use of rheometers to study stresses, often as a function of either strain or shear rate, in both dry [33] and wet [34] granular materials. A similar set of experiments explores the motion of an intruder in a granular, with interest in the motion and forces experienced by the intruder [35, 36]. These experimental tools aim to characterize the granular material as a whole, often measuring analogous physical properties that are inspired by typical solids and fluids, such as viscosity and sound speed.

Another experimental approach attempts to treat the granular material for

what it is: a collection of discrete athermal elements. While direct observation of bulk phenomena may be lost at times, this approach aims to link such phenomena to microscopic motion within the material. The following section describes such techniques.

2.1.1 Imaging Particle-scale Motion in 3D

Generally speaking, imaging the entirety of particle-scale motion can be readily done when studying 2D granular materials. A truly 2D system is one where the material is a single layer of grains with translational motion restricted to a two-dimensional plane with one perpendicular rotational degree of freedom. Typically, this implies that the material is a series of thin disks confined to move either on a horizontal plane or between two confining vertical plates. Since the entire system is visible by eye, individual grains can be readily identified, located, and tracked over time. If photoelastic grains are used in the experiment, a set of cross-polarizers will also yield information on the force chains that propagate throughout the material [37]. If the disks are labeled with unique patterns, one can also track the orientation in order to quantify rotational motion [38].

When dealing with a 3D granular material, the task of locating and tracking individual grain motion is less straightforward. For one, the material is often opaque. Even when the material is made up of glass or plastic grains that are themselves transparent, the grains will significantly refract light that enters from the surrounding air. As a result, individual grains are no longer distinguishable within just a few

grain diameters into the material. To overcome this challenge, several techniques have been developed to capture 3D images of granular materials.

One of the first techniques that captured granular flows in 3D is the use of magnetic resonance imaging (MRI) to acquire concentration images within a rotating tumbler [39]. Other methods of 3D imaging of granular materials, both static and flowing, include x-ray tomography [40] and confocal microscopy [41].

The imaging technique used in the experimental studies presented in this thesis is refractive index matched scanning (RIMS) [42]. The main idea behind RIMS is that a granular material made up of individually transparent grains will no longer be visible when immersed in a fluid of the same refractive index. In order for a dense 3D granular material to retain a high volume fraction, $\phi \approx 0.6$, the solid material should be denser than the fluid. If a fluorescent dye is added to the fluid, this allows a laser sheet at a fluorescing wavelength to illuminate a planar cross section within the pile, which can then be captured by a high-sensitivity charge-coupled device (CCD) camera. The principle of this technique is illustrated in Figure 2.1. If the laser source is moved, this allows a distinct cross section of the pile to be imaged. Consequently, a full 3D image of the granular pile can be captured over small increments in the laser and CCD camera positions using stepper motors.

Of course, some additional considerations besides matching refractive index are required when using this technique on any granular material. For instance, one must be conscious of whether the granular material and fluid are chemically inert. In other words, the presence of the fluid should not appreciably change the chemical structure of individual grains, possibly resulting in the material no longer behaving as discrete

grains that interact via repulsive contact forces. Furthermore, consideration must be given to the hydrodynamics effects of the fluid on the motion of individual grains. Otherwise, the system under study is no longer a purely granular system, but rather some form of dense suspension. In practice, when the granular material is driven by quasistatic forcing, a relatively viscous fluid allows the fluid-immersed system to retain frictional behavior reminiscent of a dry granular material [43]. On the other hand, if the driving force on the granular material is fast, as in the case of impact, a viscous fluid can have a prominent and adverse affect on the observed motion [44].

This technique is used in the experimental studies described in chapters 3, 5, 6, and 7, which utilize experimental design and code that were developed in-house [45]. The granular flow geometry that is studied using this technique is quasistatic circular split-bottom shear, depicted in Figure 2.2 along with much of the imaging apparatus. In this geometry, the granular material is driven from the bottom by a rotating disk, which is separate from the rest of the tank floor and given a roughened pattern to couple motion of the disk directly with the bottom layer of grains. This kind of geometry allows the system to be indefinitely sheared, with wide shear zones that are several grain diameters wide and far from the walls [46, 47]. The shear zone dimensions are determined by characterizing the azimuthal velocity profile at various heights z within the pile. For the split-bottom geometry, velocity profiles are well described by the cylindrically symmetric complementary error function,

$$\Omega(r) = A \operatorname{erfc}\left(\frac{r - R_c}{W}\right) \tag{2.1}$$

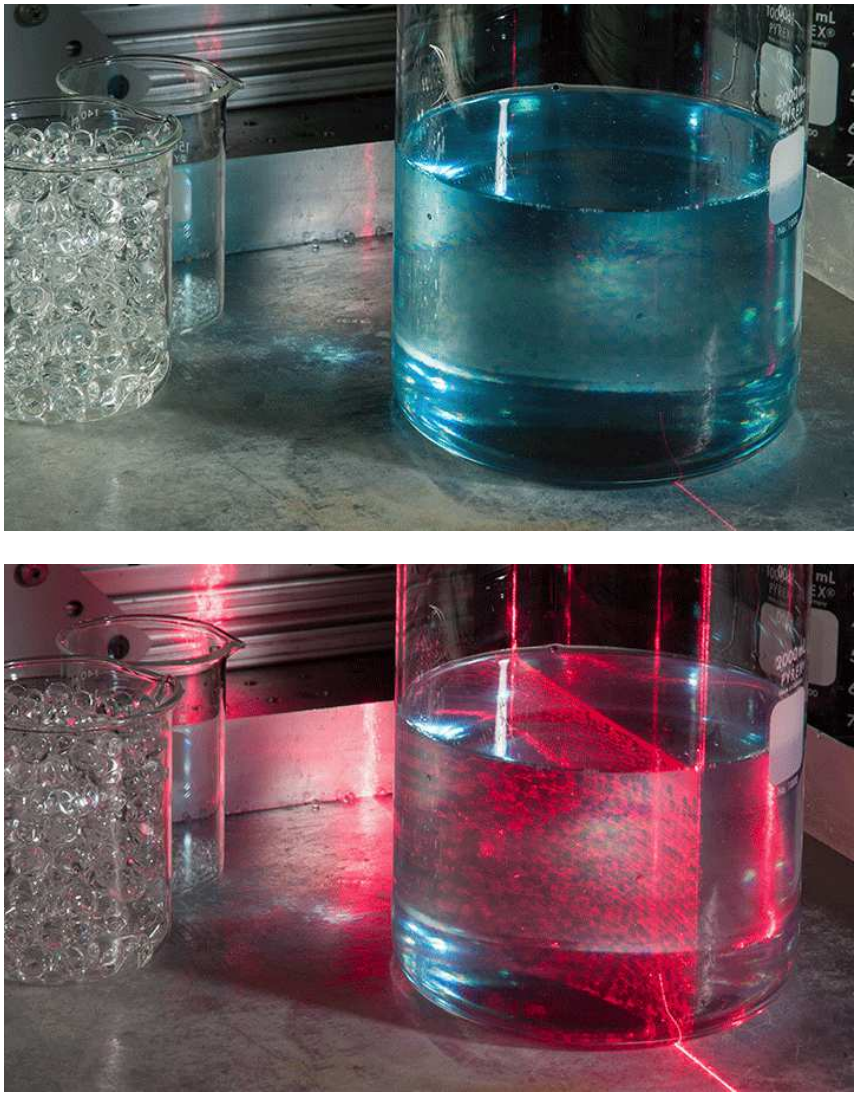

Figure 2.1: (Top) A beaker filled with PMMA beads and a fluorescently dyed index-matched fluid, which is almost entirely Triton X-100 with small amounts of hydrochloric acid and Nile Blue 690 Perchlorate. Because of the close index-matching, virtually nothing can be seen in the interior of the beaker by eye. (Bottom) Illumination from a 660 nm laser sheet causes the fluid to fluoresce, which also allows cross sections of the spheres to become visible. (Photo Credit: Earl Zubkoff, Essential Eyes Photographics)

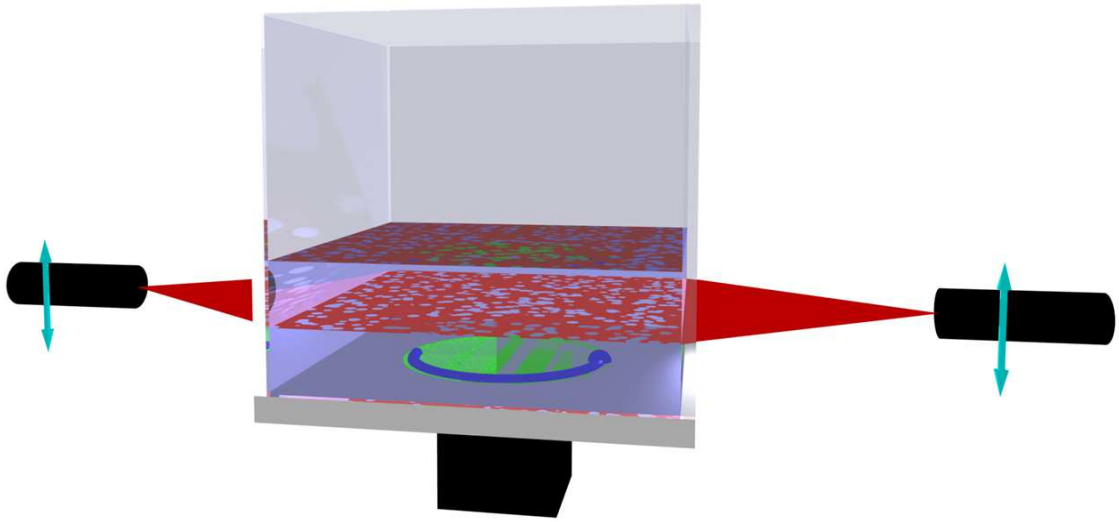

Figure 2.2: Illustration of the shear cell, with index-matching fluid and 3D imaging apparatus. A camera that captures horizontal cross sections from the top-down is not shown.

where r is the radial polar coordinate, A is a constant proportion with dimensions of angular velocity, and R_c and W are the center and width, respectively, of the shear zone at a given height z. This velocity profile can also be referred to as a primary flow profile, since the flow of the grains is directly driven in this direction. This will be an important distinction to make from the secondary flow profiles introduced in chapter 3.

The granular material is driven by the disk at a rate of 1 mrad/s. In order to capture images with maximum resolution, the forcing is not continuous. The disk rotates 2° (0.035 rad), stops, and waits for the camera and laser sheets to capture a full 3D image. Every component of the image acquisition system is controlled in an automated fashion by a computer and stepper motors. When a scan is complete,

the lasers and camera reset their positions while the disk slowly turns another 2°. This procedure repeats many times over the entire course of an experiment.

2.1.2 Analysis of 3D Motion

Once images are captured over the course of an experiment, they can be used to characterize the microscopic motion within the granular material. If one is interested in only the average flow of granular materials at the surface, or otherwise incapable of distinguishing individual grains, one could use particle image velocimetry (PIV). PIV is a common method used in experimental fluid dynamics and when applied to granular flows, yields a persistent average flow field. However, PIV fails to capture information about individual grain motion, since it relies on relative intensities in time series images rather than physical grain locations. If an imaging technique is used where discrete grains are visible, there are many image processing algorithms that can be used to locate the grains. These techniques include convolution, Hough transforms, and watershed algorithms. After the positions of individual grains are determined, they can be uniquely labeled to form grain trajectories using a particle tracking algorithm.

One method of tracking is particle tracking velocimetry (PTV) [48]. This method relies on stitching tracks together where the total squared displacement is minimized between subsequent frames. When going from an initial frame to the following frame, coordinates considered for stitching to a track must lie within some distance of the track's current position. This is a parameter that is provided by the

user, as well as whether particles are allowed to be missed for a certain number of frames and the minimum length, in terms of number of frames, of a valid track.

Another tracking algorithm is Lagrangian predictive tracking [49]. In this case, given tracks that are already started, it uses the average velocity between the current and previous frame to guess where the particle will end up in the following frame. This predictive component can cut down on the amount of time it takes to locate the coordinate that should be stitched to each track.

After the completion of a particle tracking algorithm, the final output is a list of coordinates and time frames, with unique particle identification numbers to distinguish individual grains. From here, further analysis of microscopic and mesoscopic motion can be performed, and will be described in further chapters. Both of these tracking algorithms are used in the studies described in this thesis. The specific tracking algorithm used will be identified in each case. In terms of overall performance, neither algorithm seems to stand out, so the choice mostly comes down to a matter of preference. For instance, the predictive tracker runs faster on large data sets, as it limits the number of possible trajectories a particle could go between subsequent frames. However, PTV does not assume local velocity fields so it is more robust under suddenly changing flow fields.

2.2 Theoretical & Simulation Techniques

In addition to experiments, there are a number of techniques used to study granular materials from a theoretical perspective. Despite being a statistical ensem-

ble, the athermal and non-Brownian nature of granular materials makes it difficult to apply the tenants of statistical mechanics and thermodynamics. There are, however, analogous definitions of thermodynamics quantities, such as temperature and entropy, that can be applied to granular systems [50]. Some approaches used to theoretically study complex systems and fluids, particularly granular materials, are described in the following sections.

2.2.1 Continuum Modeling

A common approach to modeling a granular material is to consider it not as a collection of $N > 1$ or $N \gg 1$ discrete elements, but rather as one continuous body. This kind of abstraction is apparent when picturing several bulk phenomena in which the granular material exhibits a high degree of collective behavior. A couple examples include the rigid structure of sand castles and the flow of small debris down an incline during an avalanche. A common approach used in early continuum models was to use the Mohr-Coulomb criterion for failure in a deformable solid as a starting point [51, 52].

Continuum modeling has also seen application in the prediction of bulk segregation [12]. Unfortunately, these and other models often fail to provide a widely applicable predictive model. The reason is that many of these models provide a system-specific justification for a bulk rearrangement without utilizing particle-scale dynamics. Currently, there is ongoing effort to incorporate particle-scale plasticity into new continuum models, which has already demonstrated success in faithfully

reproducing well-known flow profiles in 3D shear geometries [53].

2.2.2 Discrete Element Modeling

Some theoretical methods have been designed to embrace the discrete nature of granular materials. While this generally requires substantial computational resources, many simulation techniques have been developed to robustly test and verify the behavior of similar experimental systems, or otherwise probe conditions that are difficult to control in a laboratory.

Cellular automata (CA) has been successfully applied to a few simple granular systems. The basic premise of CA is to discretize the system in a way that the state of the system can be updated using very simple update rules. For instance, a 2D system can be simplified to be a lattice of sites that are either empty or occupied by a single grain with certain characteristics, such as velocity and local stress. One of the earliest physical systems studied using the framework of cellular automata was the simple building up and eventual avalanching of sandpiles [54, 55]. A similar technique was also developed in the context of gravity-driven hopper flows [56, 57].

Molecular dynamics (MD) is another approach that has been used for decades to simulate the dynamic behavior of entire granular systems [58]. Recent studies have used MD rather than CA, as improvements in computing have allowed researchers to make fewer simplifications in order to fully characterize the behavior of a complex granular system. MD simulations begin with the generation of a packing, generally one that is initially stable or jammed. All of the grains are uniquely

labeled from the beginning and kept track of over the course of the simulation. At periodic points in the simulation, the total force on each grain is computed by taking a superposition of pairwise forces exerted by neighboring grains. Depending on the system of interest, these forces are often conceptualized as either spring and dashpot interactions of soft spheres [58, 59] or colliding hard spheres [60]. These forces are then used to regularly update the positions and velocities of each grain.

Chapter 4 describes a study of a granular material undergoing cyclic shear in a MD simulation. The simulated system is a 2D box of bidisperse frictionless soft disks, with shear applied at opposite ends of the containing box using periodic boundary conditions. The simulation begins with the generation of a collectively stable packing of bidisperse disks. The procedure for generating this packing is similar to the one described by Nu, Blawzdziewicz, and O'Hern [61]. The packing is initialized by randomly selecting grains positions within the simulation box. An initial pair of diameters is picked for the grains, such that it satisfies the prescribed size ratio of large grains to small grains ($D_L/D_S = 1.4$) with initial overlap between disks at some area fraction well below the jamming point $\phi_J \approx 0.84$. An example of an initial configuration, before any other modification is made, is shown in the left side of Figure 2.3. At this point, disk positions are modified using a conjugate gradient algorithm to locate a local minimum in average configurational energy per grain [62]. This energy is determined by the aggregate linear spring potential energy of overlapping grains, with the contribution from an overlapping pair i and j given by

$$V_{ij}\left(r_{ij}\right)=\frac{1}{2}\left(1-\frac{r_{ij}}{D_{ij}}\right)^{2}\Theta\left(1-\frac{r_{ij}}{D_{ij}}\right) \tag{2.2}$$

where D_{ij} is the average diameter of the two grains,

$$D_{ij}=\frac{D_i+D_j}{2} \tag{2.3}$$

and r_{ij} is the distance between the centroid positions of i and j,

$$r_{ij}=|\boldsymbol{x}_i-\boldsymbol{x}_j| \tag{2.4}$$

Θ is the Heaviside function, which reinforces that contributions to the total energy only come from grain pairs that overlap, $r_{ij}\leq D_{ij}$. The total configurational energy is then given by summing over all pairs of grains, with the average energy per grain given by

$$\bar{V}=\frac{\sum_{i=j+1}^{N}\sum_{j=1}^{N}V_{ij}}{N} \tag{2.5}$$

Once a local minimum in $\bar{V}$ has been found, the grain sizes themselves are uniformly modulated while preserving the prescribed size ratio between large and small grains. For instance, an early cycle of energy minimization will likely produce a packing with some grains that are "floaters" with no contacts at all. The average interaction energy would then fall below a desired threshold $T=5\cdot10^{-9}$. To increase the total energy, disk diameters are increased at a predetermined scaling, and the system is relaxed to a new interaction energy minimum. Later on in the process, grains may become too big, such that they exceed the upper bound in tolerance for

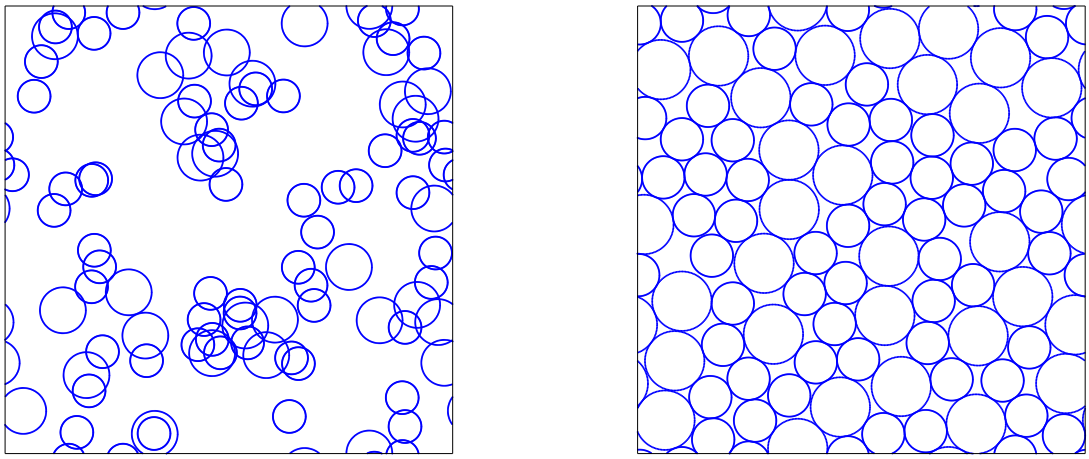

Figure 2.3: (Left) An initial random packing generated with 90 bidisperse grains. There are 60 small grains and 30 large grains, with a size ratio of 1.4. (Right) The final stable packing for these grains, after 45 iterations of energy minimization and grain size modulation. Compared to the initial configuration, this is much denser, yet contains a very small amount of disk overlap.

the interaction energy ($2T = 10^{-8}$). In this case, grain sizes are uniformly decreased, with subsequent increases at a smaller scaling. This procedure is repeated several times, until the average energy per grain $\bar{V}$ falls within the range $T < \bar{V} < 2T$. This procedure results in a dense stable packing, similar to one shown in the right side of Figure 2.3, which is characterized by negligible grain overlaps, as well as few grains with zero contacts.

Once a stable packing has been generated, the next matter is to drive the system. Shear is applied to the top and bottom of the simulation box using the procedure of Lees-Edwards periodic boundary conditions [63]. Copies of the simulation window on the top and bottom are shifted horizontally, in small steps up to

a reversal amplitude, at which point they switch direction and move toward their original positions.

Within the simulation windows, the position and velocity of each grain must be updated at each step of the simulation. This is done using a velocity Verlet procedure [64]. Suppose that at an initial time t, the position, velocity, and acceleration of grain i are all known. The new position of grain i after a time interval δt is given by

$$\boldsymbol{x}_i\left(t+\delta t\right)=\boldsymbol{x}_i\left(t\right)+\dot{\boldsymbol{x}}_i\left(t\right)\delta t+\frac{1}{2}\ddot{\boldsymbol{x}}_i\left(t\right)\delta t^2 \tag{2.6}$$

where a dot above a variable denotes a derivative with respect to time. The next step is to update the velocity of the grain, but in a way that allows for a refined estimate of velocity-dependent forces. In that case, the velocity is updated over just half the time interval,

$$\dot{\boldsymbol{x}}_i\left(t+\frac{\delta t}{2}\right)=\dot{\boldsymbol{x}}_i\left(t\right)+\ddot{\boldsymbol{x}}_i\left(t\right)\frac{\delta t}{2} \tag{2.7}$$

Now consider the total force acting on grain i, as a means of calculating the acceleration. In the simulated granular system, grain i will feel a force from grain j if the two overlap, just as in the stable packing generation. The force on each grain is determined by two interactions: a restoring linear spring force that is proportional to the amount of overlap and a dissipative force that is proportional to the difference in the grains' velocities. Specifically, the force on grain i due to grain j is given by

$$\boldsymbol{F}_{ij} = \left[\frac{1}{D_{ij}}\left(1 - \frac{r_{ij}}{D_{ij}}\right) - \gamma\left(\dot{\boldsymbol{x}}_i - \dot{\boldsymbol{x}}_j\right)\cdot\hat{r}_{ij}\right]\Theta\left(1 - \frac{r_{ij}}{D_{ij}}\right)\hat{r}_{ij} \tag{2.8}$$

where $\gamma = 50$ is the damping coefficient and $\hat{r}_{ij}$ is the unit vector toward i from j,

$$\hat{r}_{ij} = \frac{\boldsymbol{x}_i - \boldsymbol{x}_j}{r_{ij}} \tag{2.9}$$

The total force that grain i then feels is given by summing over all neighboring grains,

$$\boldsymbol{F}_i = \sum_j \boldsymbol{F}_{ij} = m\ddot{\boldsymbol{x}}_i \tag{2.10}$$

It should be noted that in these simulations, there is no interstitial fluid to add any component of Brownian motion, nor is there an affine field to couple grain motion to, aside from the shear provided at the boundaries. To minimize computation time, candidate neighboring grains to i, which are within 2 grain diameters of the surface of i, are previously identified with periodic updates. Equation 2.10 loops over these candidate neighbors rather than over all other $N-1$ grains. The acceleration of grain i is then given by

$$\ddot{\boldsymbol{x}}_i\left(t+\delta t\right) = \frac{1}{m}\sum_j \boldsymbol{F}_{ij}\left[\boldsymbol{x}_i\left(t+\delta t\right), \boldsymbol{x}_j\left(t+\delta t\right), \dot{\boldsymbol{x}}_i\left(t+\frac{\delta t}{2}\right), \dot{\boldsymbol{x}}_j\left(t+\frac{\delta t}{2}\right)\right] \tag{2.11}$$

where $m = 1$ for both grain species. Finally, the velocity update for the second half of the time interval δt is completed,

$$\dot{\boldsymbol{x}}_i\left(t+\delta t\right)=\dot{\boldsymbol{x}}_i\left(t+\frac{\delta t}{2}\right)+\ddot{\boldsymbol{x}}_i\left(t+\delta t\right)\frac{\delta t}{2} \tag{2.12}$$

As the simulation goes on, total pressure, which is determined by the cumulative amount of compressive force in the system, is kept constant through further small modulations of the grain diameters.

Chapter 3

Shear-driven Size Segregation

This chapter is based on work contained in the publication: Suppression and Emergence of Granular Segregation under Cyclic Shear. M. Harrington, J.H. Weijs, and W. Losert, *Phys. Rev. Lett.* **111**, 078001 (2013), ©2013 by the American Physical Society. I performed all experiments and analysis used in this study, following initial experiments performed by Joost Weijs.

3.1 Introduction

When mixtures of granular materials are continuously disturbed by external forcing, such as vibration, gravity, rotation, or shear, the grains often separate based on their species properties, such as size or density [10, 13, 14, 65, 66, 67, 68, 69, 70, 71]. This phenomenon, known as *segregation*, has been a subject of scientific interest for several decades because of its widespread applicability in both nature and industry, from stratification of avalanche deposits to the non-uniform settling of mixed nuts and cereals.

Previous studies look at the onset and patterns of segregation, and several theoretical models have been proposed [12, 13, 14, 15]. A universal feature of the models is gradient-driven segregation flux. In the specific case of dense shear-driven segregation, however, the relative contributions of gradients in friction, shear, and

average kinetic energy (or, kinetic temperature) are not well established. In addition, most candidate models for shear-driven segregation are linear [12, 72]. A key nonlinearity missing from the current models is granular convection, which can play a vital role in the segregation process [10, 70, 73]. Indeed, the behavior of experimental shear-driven systems deviates from what current models predict [71].

In particular, convective flows can lead to the rise of large particles in vibrated beds [10]. Even under quasistatic vibrations with very low kinetic temperature and convection, critical size ratios for the rising of large intruders have been observed [65, 74]. While this has inspired further work on vibro-excited systems, there is little discussion in the current literature about shear-driven segregation in the absence of kinetic temperature.

One distinguishing feature of shear-driven flows is that, unlike vibro-excited systems, they can exhibit flow driven by bulk shear forces, with particle-particle interaction potential energies that are orders of magnitude larger than kinetic energies [75]. Driven slowly, granular shear flows can then exhibit close to reversible particle trajectories under oscillatory driving [16, 17]. Continuum models of segregation are based on gradients, therefore invariant under reversal of shear direction, and predict the same segregation flux for both steady and oscillatory shear. Indeed, the absolute size of individual particles relative to the amount of shear does not enter into these models, nor does a characteristic length scale over which gradient-induced segregation manifests.

In this chapter, we provide insight into these challenges by presenting experimental results from a dense three-dimensional (3D) shear-driven bidisperse granular

material. Using the refractive index matched scanning (RIMS) imaging technique [42], we are able to experimentally determine the trajectories of almost all particles in the mixture as the system is slowly sheared, both steadily and cyclically, in a split-bottom geometry. We directly measure the bulk segregation patterns under steady and cyclic shear, and characterize segregation at the micro- and mesoscale by quantifying the reversibility of particle rearrangements and examining the resulting secondary flows of the system.

3.2 Setup & Procedure

The granular system is a dense bidisperse mixture of polymethyl methacrylate spheres, with small and large diameters of $D_S = 3.2$ mm and $D_L = 4.8$ mm, respectively. The mass ratio between the two species of grains ($\frac{M_S}{M_L} = \frac{16}{27}$) is selected such that the number ratio of small to large grains $\frac{N_S}{N_L} = 2$. The sides of the square tank containing the pile are 15 cm long and the pile height is 4.6 cm, approximately equal to the radius of the shearing disk, $R_s = 4.5$ cm, as well as $10D_L$.

The grains are immersed in an index-matched interstitial fluid, Triton X-100. The index-matching allows light from two laser sheets, mounted on either side of the tank, to pass through undeflected. We also add a laser dye, Nile Blue 690 Perchlorate, that fluoresces at the laser wavelength (635 nm), as well as a small amount of hydrochloric acid to stabilize the mixture. With the laser sheets aligned at a particular height, a high-sensitivity Sensicam camera captures a horizontal cross section of the pile from the top-down. The laser sheets and camera move

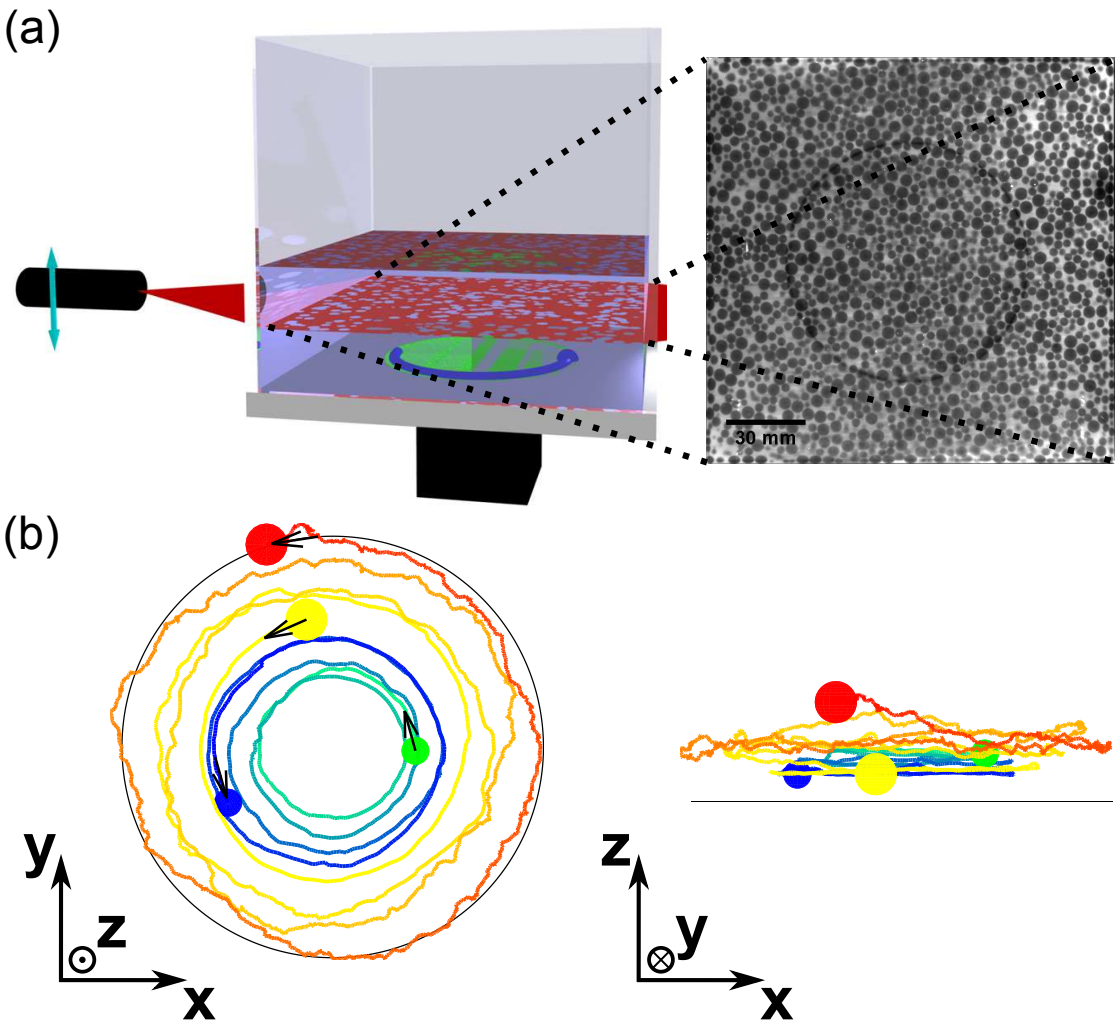

Figure 3.1: (a) The split-bottom shear cell and a sample horizontal cross section (an aligned second laser sheet and a high sensitive camera that captures images from the top-down are not pictured). (b) Sample trajectories of a small (light green to dark blue) and large (light yellow to dark red) grain under steady shear. The black circle represents the shearing disk.

incrementally along stepper motors, with cross sections taken about every 200 μm in height. All of the cross sections together construct a full 3D image of the pile. An illustration of our setup is shown in Figure 3.1(a).

We consider the response of the granular system to both steady and cyclic shear, with amplitudes of 10° and 40°. The shearing disk is separated from the rest of the tank floor and rotates at a rate of 1 mrad/s, with static 3D images captured every 2°. At this shearing rate, the flow profiles of the pile resemble that of a dry pile and are also rate-independent [43]. In addition, the circular split-bottom geometry allows for the formation of wide and robust shear zones far from the system walls [46, 47].

When an experiment is complete, particle center positions are determined using a 3D-adapted convolution kernel [76], which also distinguishes between large and small grains. In each frame, we are capable of extracting the position of at least 95% of particles, with a particle center resolution of about 100 μm. Then, a Lagrangian predictive particle tracking algorithm [49] identifies individual particles and their trajectories. Examples of individual particle trajectories, for a large and small grain under steady shear, are shown in Figure 3.1(b).

3.3 Results

3.3.1 Bulk Segregation

A standard segregation pattern that is seen in many polydisperse mixtures is the Brazil Nut Effect (BNE), in which large particles rise to the top of the pile,

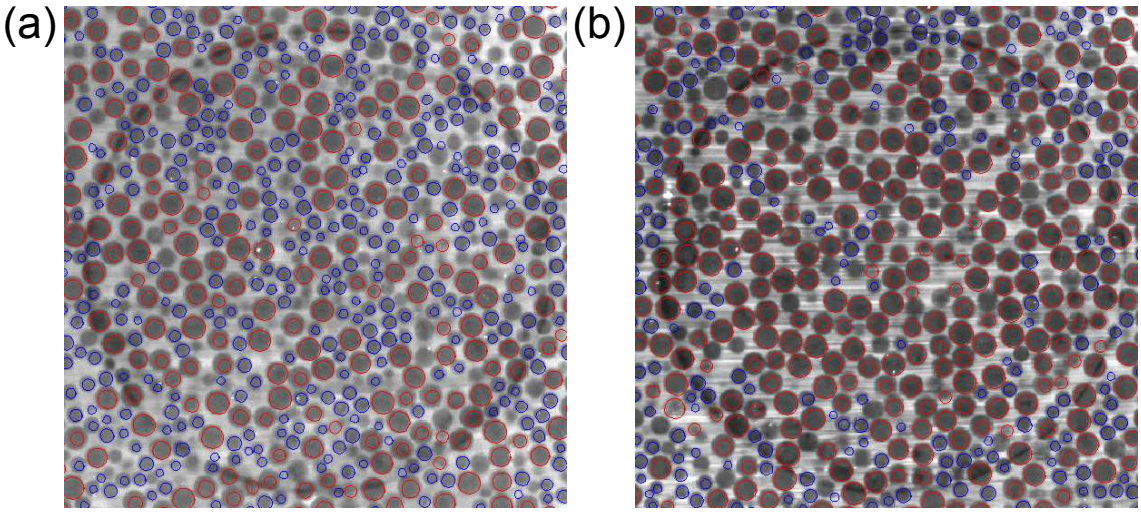

Figure 3.2: Cross sections of the granular pile at 3.8 cm above the shearing disk, or about 2 large grain diameters from the free surface, (a) in the initial mixed state (b) after 29.3 revolutions of the shearing disk. Large red and small blue circles represent large and small grains, respectively.

leaving smaller sizes to settle toward the bottom. In this slowly sheared system, a pattern similar to the BNE is observed under steady shear. Figure 3.2 shows how a cross section at a height of 3.8 cm (8 large grain diameters) becomes primarily populated with large particles after almost 30 revolutions of steady shear. This height is close to the free surface of the pile, only two large grain diameters away. This effect is also indicated by the sample trajectories shown in Figure 3.1(b). The pile as a whole rearranges such that large particles inhabit a cylindrical region at the top 60% ($\approx V_L/V_{total}$, where V_L is the total volume of large grains and V_{total} is the total volume of *all* grains) of the pile, directly above the shearing disk. To quantify bulk segregation, we calculate the volume fraction of large and small grains in this region of interest. The inset of Figure 3.3(a) illustrates that over about 30 rotations

of the shearing disk, the pile is continually segregating, with a total volume fraction that remains consistent throughout.

Under oscillatory shear, however, segregation is not necessarily observed. The results for bulk segregation under steady shear and the two oscillatory amplitudes considered are summarized in Figure 3.3. When the amplitude is 10°, the volume fractions of large and small particles appear to remain constant throughout. This indicates that the system is not segregating over the time interval measured. Individual particle trajectories are consistent with this observation, as discussed in the following section.

For sufficiently large amplitudes of oscillatory shear, the pile does slowly segregate. For an amplitude of 40°, the rate of segregation is smaller than under steady shear. However, segregation is apparent over the measured time period and the associated changes in volume fraction are in accord with BNE.

3.3.2 Microscopic Reversibility

The RIMS technique allows us to also probe segregation microscopically by considering particle contact networks and mean squared-displacements (MSDs) within the shear zone of the split-bottom geometry, where most rearrangements occur [17, 46, 47].

In order to verify that the granular material is segregating, we must see that grain motion is irreversible in terms of both grain-to-grain contacts and displacements. The pile starts in a highly mixed state, so each individual grain touches a

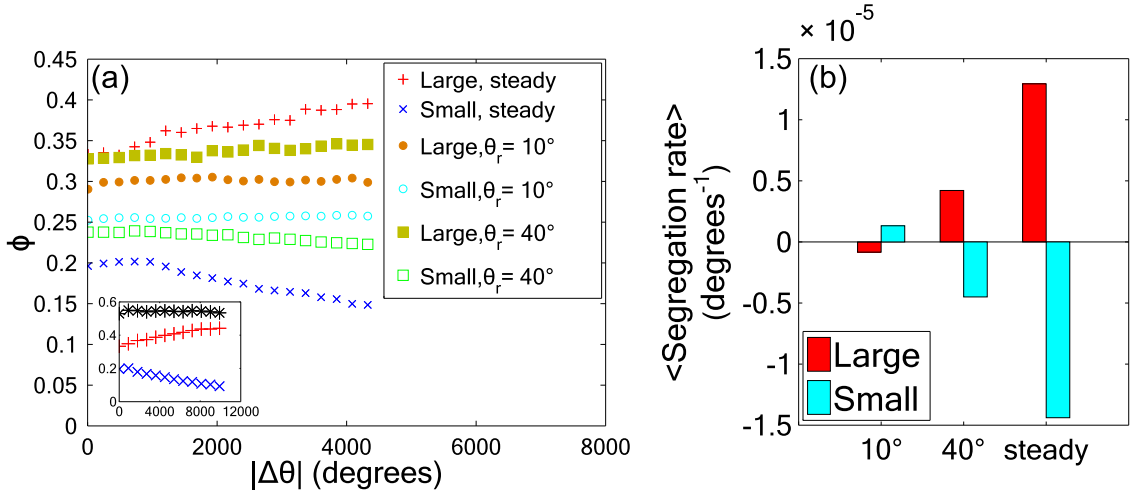

Figure 3.3: (a) Volume fractions of large and small grains under all shearing procedures considered: steady (red +'s and blue x's), $\theta_r = 10°$ (filled orange and empty cyan circles), and $\theta_r = 40°$ (filled gold and empty green squares) in the top 60% of the pile, directly above the shearing disk. Inset: Same as (a), but showing only steady shear and including total volume fraction (black asterisks). (b) The average rate of change of ϕ of large and small grains for $|\Delta\theta| \geq 1000°$.

combination of small and large grains. Under segregation, particle contacts must be constantly changing, in order to form new contacts with similar particles. At the same time, segregation requires significant and irreversible motion within the pile, so that an increasingly segregated state develops.

We determine grain contacts by finding particle pairs that, within some distance cutoff, are increasingly likely to move perpendicular to each other by sliding or rolling, as described by Herrera, *et al* [77]. Three contact length cutoffs are defined: large-large, large-small, and small-small. MSDs are simply calculated from the average square-displacement of grains from an initial reference state to a new state at a later time.

Figure 3.4(a) shows the fraction of broken links at the end of a single shear cycle, with respect to the reference network taken at the end of the previous cycle. For all three contact types, there is a decreasing fraction of contacts that are broken over time for the 10° experiment; however, the fraction of broken links for the 40° experiment remains fairly steady from cycle to cycle. Similar trends are observed if we measure MSDs of large and small grains over individual cycles, as shown in Figure 3.4(b). This distinguishing behavior of reversible and irreversible flows was also seen by Slotterback, *et al* in a monodisperse system with particle size D_L, with the same shear amplitudes [17]. This indicates that in this split-bottom geometry, there is a connection between a shear-driven granular material undergoing irreversible flows and having the capacity to segregate.

We have described the bulk segregation patterns we see under steady and cyclic shear, and linked our segregating and nonsegregating regimes to changes in

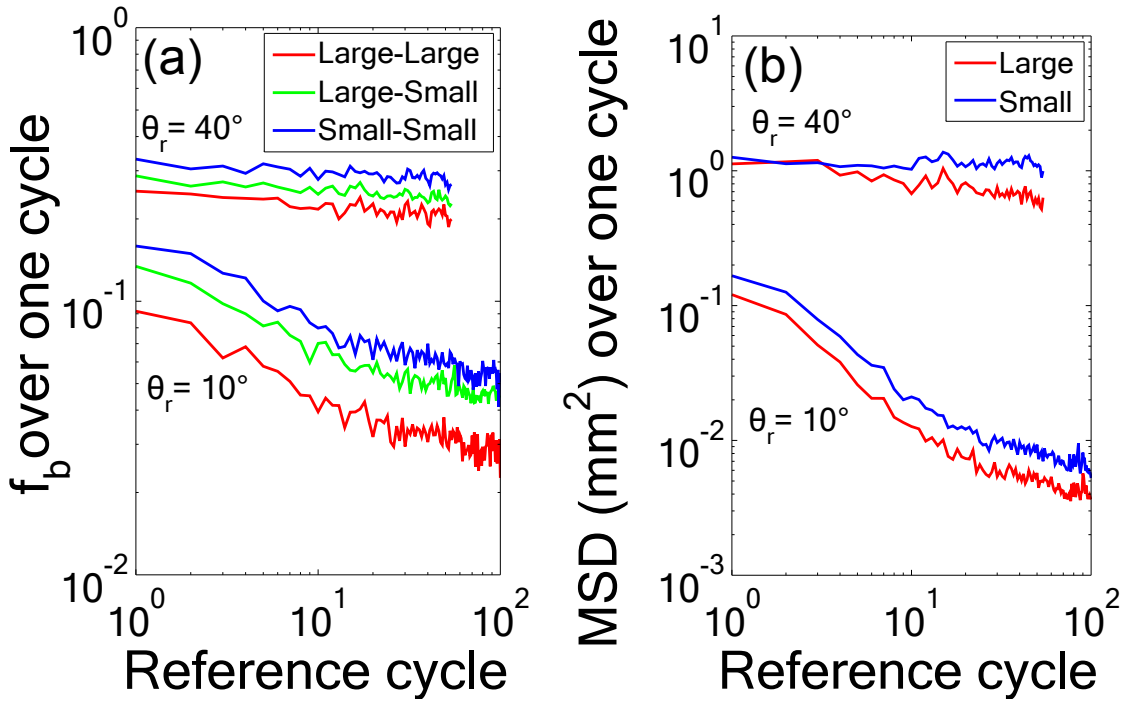

Figure 3.4: (a) Fraction of broken grain contacts and (b) MSDs over a single cycle versus that particular cycle number.

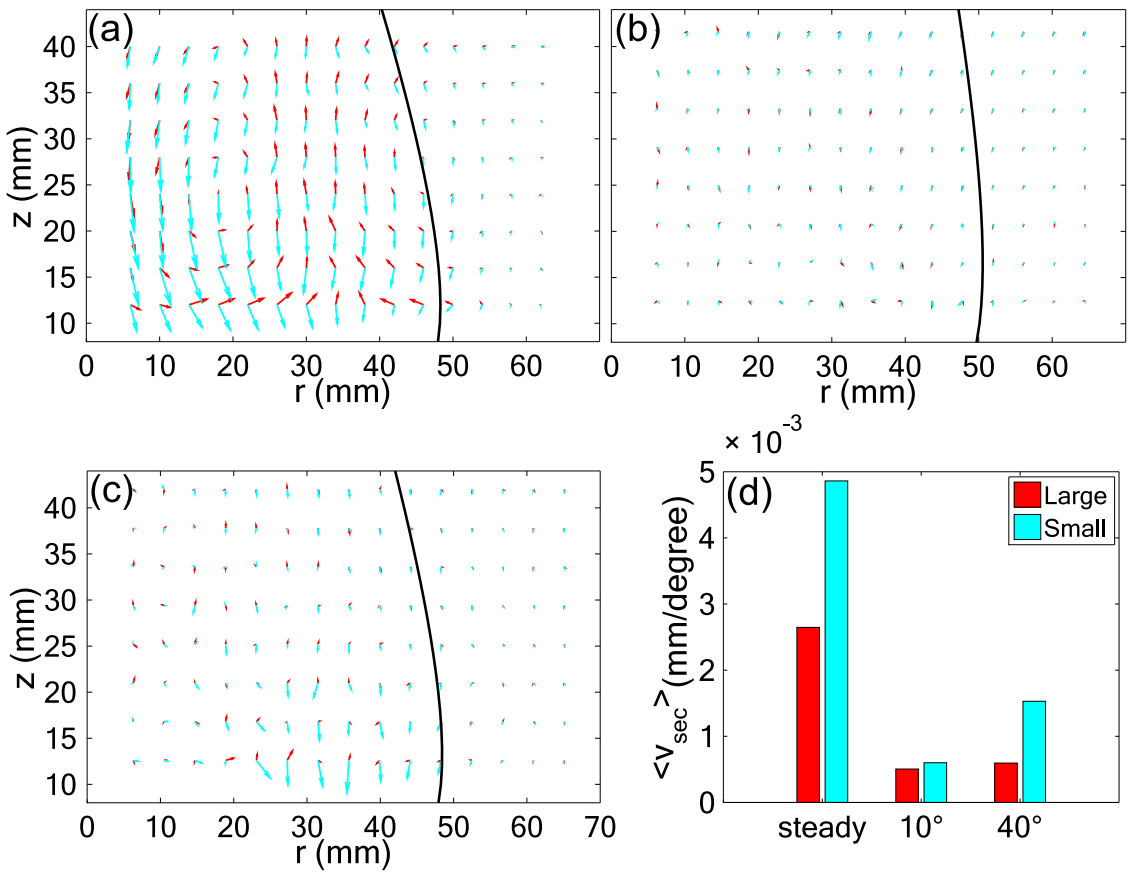

Figure 3.5: Time- and θ-averaged flows of large (dark red arrows) and small (light cyan arrows) grain flows plotted together for all shearing procedures considered: (a) steady, (b) $\theta_r = 10°$, (c) $\theta_r = 40°$. Vectors are scaled such that the grid spacing corresponds to $5.6 \cdot 10^{-3}$ mm/degree shear. (d) Average magnitude of secondary flow vectors within the shear zone outer boundary (black curve in (a)-(c)).

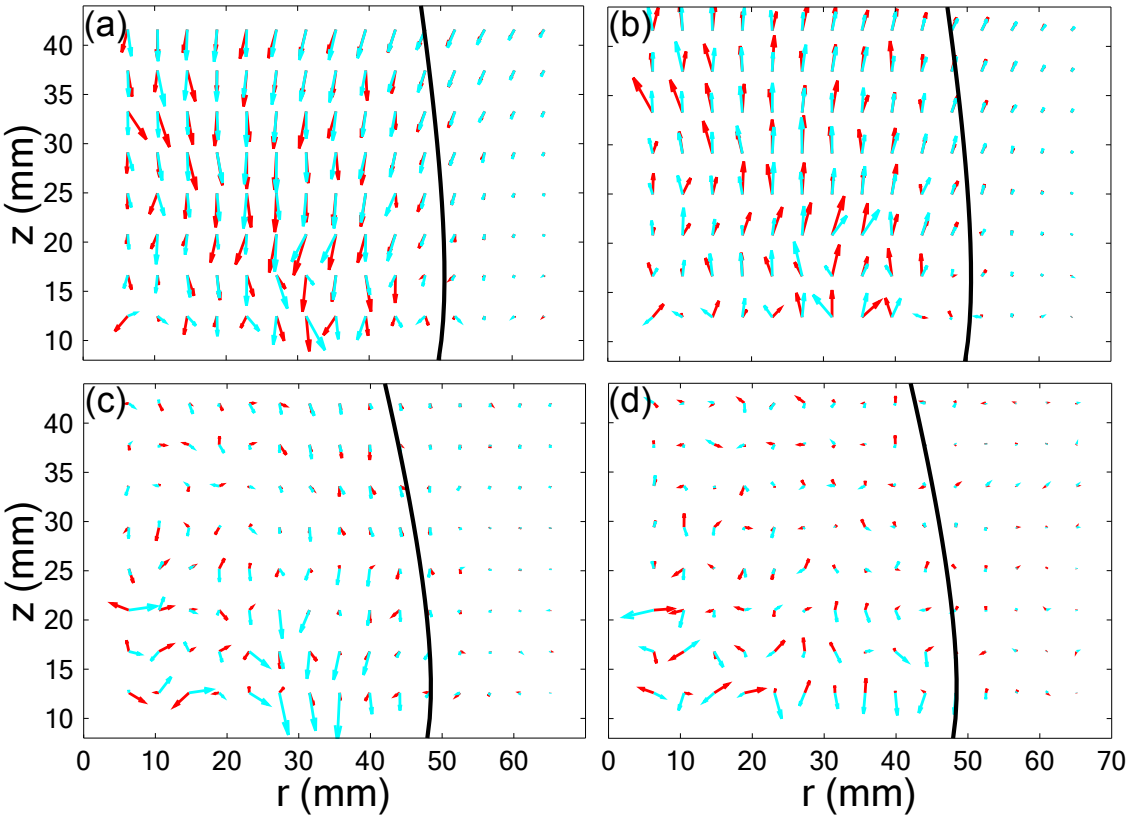

Figure 3.6: For $\theta_r = 10°$, reversible secondary flows can be seen when averaging over (a) positive and (b) negative strain. For $\theta_r = 40°$, such a strong distinction cannot be made between (c) positive and (d) negative strain. Flow vectors are shown on the same scale as Figure 3.5.

particle-scale reversibility. However, segregation requires rearrangements on much larger than particle scales. To capture such larger scale rearrangements, we are motivated by the prevalence of convective flows in other segregating systems to examine secondary flow profiles.

3.3.3 Secondary Flows

The motion of the grains is primarily in the θ-direction, as grains near the bottom are driven locally by the rotation of the shearing disk. However, the grains are also free in move in the other two cylindrical coordinates, r and z. The time- and azimuthal-averaged motions of grains in r and z are referred to as *secondary flows*. Simulations in the split-bottom geometry suggest that secondary flows are a key component of the segregation process [70].

For steady shear, the secondary flows for large and small particles are shown in Figure 3.5(a). The flow profiles of the two species are vastly different; while the large particles form two distinct convection rolls, the small particles primarily drift toward the bottom. There is a net downward flux of small particles above the shearing disk, which is in line with the bulk segregation pattern. Also shown in Figure 3.5(a)-(c) is the outer border of the shear zone, which is determined from the shape of the azimuthal, or primary, flow profiles [46, 47]. The secondary flows exist within this boundary, suggesting that the segregating region is necessarily determined by the size of the particles and the shearing disk. Furthermore, the symmetry of our system indicates that the magnitude and direction of the flow fields are independent on the direction of steady shear.

Under oscillatory shear, the secondary flow profiles are dependent on the shear amplitude. For an amplitude of 10°, the secondary flows of both species are suppressed, as illustrated in Figure 3.5(b). This is to be expected given the increasing reversibility of the system over time, and is also reflected when averaging over

only positive and negative strain. The motion illustrated in Figure 3.6(a)-(b) indicates that the system merely exhibits alternating phases of compaction and dilation. When the shear amplitude is increased to 40°, such reversibility in the fabric is not observed due to overall trajectory irreversibility. While granular convection remains mostly undeveloped for large particles, small particles, particularly those close to the shearing disk, drift downward, as shown in Figure 3.5(c) and Figure 3.6(c)-(d). For higher amplitudes, as irreversibility increases, we expect to see stronger downward drifts of small particles, as well as granular convection of large grains to approach that of steady shear.

3.4 Discussion & Conclusions

Using the RIMS technique, we image and track individual grains in a dense 3D bidisperse granular mixture under the influence of shear in a split-bottom geometry. We observe that in a regime of slow, rate-independent steady shear, the system segregates with large particles occupying the top portion of the pile directly above the shearing disk. When the system is sheared cyclically, there is a critical shear amplitude below which segregation is suppressed.

We find that bulk segregation may be linked to microscopic reversibility of small and large grain trajectories. Under 10° oscillatory shear, trajectories of small and large grains are increasingly reversible over time, as observed structurally from their grain contacts and spatially from their MSDs. However, at 40° oscillatory shear, the degree to which the large and small grain trajectories are reversible re-

mains steady over all cycles. These trends of microscopic reversibility are very similar to observations of the monodisperse system [17], indicating that they are not due to any additional forces, unique to granular mixtures, that drive segregation.

Finally, we investigate the secondary flow profiles brought about by the (ir)reversibility of the system. Under steady shear, we find clear convective flows of large grains, which help drive the segregation mechanism by allowing large grains to settle at the top of the pile, while a net flux of small grains falls toward the bottom of the container. These flows are also confined within the outer boundary of the shear zone, suggesting that the size and shape of these flows are dependent on the system geometry. For small amplitude oscillatory shear, however, secondary flows are reversible between positive and negative strain, indicating that the system fabric retains its original configuration. Above some critical shear amplitude, the fabric breaks sufficiently and the flow profiles are less distinguishable between positive and negative strain. While convection of large grains has not completely formed, there is a clear downward drift of small grains near the shearing disk.

In this system, we observe distinct rates of segregation for steady and adequately large amplitude oscillatory shear. However, we cannot immediately attribute these rates to relevant system parameters, such as shear amplitude, diffusion coefficients, or gradients of local strain. A recent study also indicates the presence of gravity is a determinant of granular convection [78], which would be relevant for segregation rates in astrophysical applications. Future work on this system should focus on probing the functional dependence of segregation rate on these variables, which is key to determining a general predictive model for shear-driven segregation

[79].

We are encouraged by the apparent existence of a critical shear amplitude that brings about segregation. In fact, a critical strain of similar magnitude also exists for fracture [77] and irreversibility [17], suggesting that this granular system may have a universal length scale that drives inherently bulk rearrangements, yet arises directly from particle-scale dynamics. This length scale could be instrumental in the development of not only segregation models, but also predictive constitutive models for granular flows that rely on a characteristic length for cooperative rearrangements [80].

Chapter 4

Simulations of Granular Shear Flows

This chapter is based on work contained in the publication: Consequences of Anomalous Diffusion in Disordered Systems under Cyclic Forcing. M. Mailman, M. Harrington, M. Girvan, and W. Losert, *Phys. Rev. Lett.* **112**, 228001 (2014), Mitch Mailman developed the molecular dynamics package and performed the initial analysis. I provided additional analysis, particularly with regard to waiting time distributions, and revamped the discussion of candidate subdiffusive models.

4.1 Introduction

In recent years there has been a good deal of interest in amorphous systems under oscillatory driving [16, 17, 22, 23, 81, 82, 83]. These works focus on the property of reversibility of particle dynamics, or the dependence of dynamical behaviors on the distance to ϕ_J, which is the density at which the packing becomes "jammed." However, what has been less well studied is the systematic dependence of bulk and particle dynamics of amorphous systems on driving amplitude, for systems that are not strictly reversible. In this study, we simulate an amorphous system under slow, cyclic shear for a range of reversal amplitudes γ_r. We find that for our simple model, a crossover exists in the behavior of bulk and particle dynamics from a regime that is

dependent on γ_r to one that is not. This crossover appears to influence a wide range of properties, including shear stress, packing fraction, and particle displacements.

Next, we address the microscopic origins of the γ_r-dependent diffusive properties. We find a γ_r dependence in the exponent β of the mean-squared displacement (MSD) $\langle r^2 \rangle \propto t^\beta$. To limit the possible underlying stochastic processes that can potentially explain the observed subdiffusivity, we analyze the scaling properties of probability distribution functions (PDFs) as a function of distance and time for all grains. We observe that the exponent β exclusively dictates the γ_r dependence of the PDFs, as well as the MSDs and the dependence of bulk properties on γ_r.

Finally, we characterize local motion by defining a measure of average displacement relative to a grain's neighborhood. Quantifying motion in this way allows us to determine how cyclic forcing from the boundary drives overall motion throughout the system. We also find that relative motion exhibits similar crossover behavior with increasing γ_r.

4.2 Methods

We study a minimal model system, very similar to one used by Gao, Blawzdziewicz, and O'Hern [84], with the use of molecular dynamics simulation. Bidisperse (1:1) frictionless disks, with larger disks having 1.4 times larger diameter than the smaller, interact via a linear spring potential with damping [85] that is dependent on the difference in velocity between contacting grains. The bidispersity of the system prevents crystallization and segregation is not observed even for very large values of

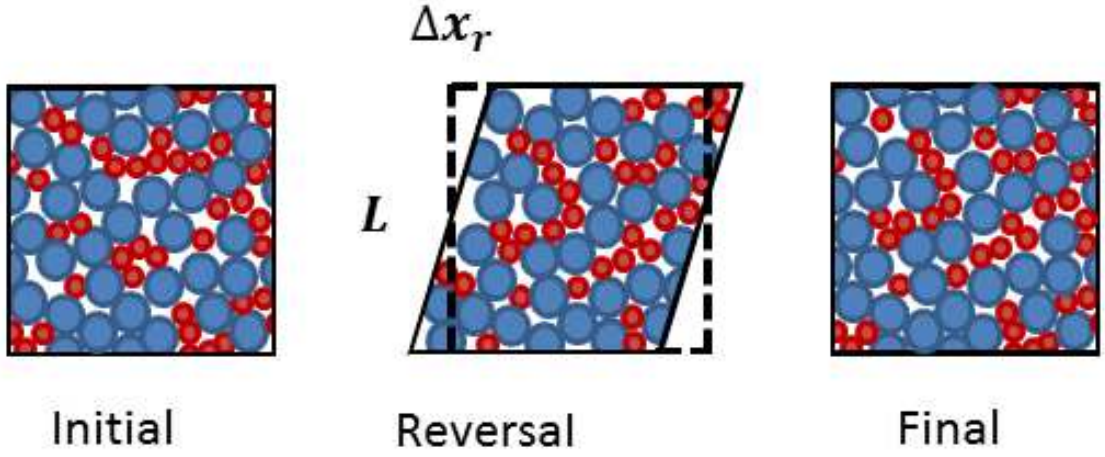

Figure 4.1: A schematic of how shear is applied to the 2D model granular system. The initial state has a repeat cell which is square with linear size L. The strain is applied by shifting the the lower and upper adjacent repeat cells horizontally up to Δx_r as per Lees-Edwards boundary conditions. Then, the shear strain Δx_r is reversed back to zero.

absolute strain. Lees-Edwards periodic boundary conditions [63] are used to apply a shear strain of γ. It is important to note that we choose not to include a coupling to an affine displacement field since we only intend to capture interactions between grains at contact, and not interactions with a constituent fluid. Since we have not included coupling to an affine field, strain is applied exclusively at the boundary by providing an offset between two periodic domains when calculating interactions. Packings are kept at approximately fixed pressure during shear by uniformly modulating the grain sizes in response to changes in pressure. At each simulation time step, the change in pressure prior to size modulating is calculated. The grain sizes are then adjusted to account for the apparent pressure change. If the pressure decreases, then grain diameters are increased, otherwise the grain diameters are decreased. This allows for consistent interactions between grains without adjusting the simulation window to account for dilation and compaction.

Under these conditions, we study 8000 grain systems over a range of $\gamma_r = \frac{\Delta x_r}{L}$ from 0.05 to 0.225, as well as $\gamma_r = 0.5$ to verify consistent behavior at very large amplitudes.

4.3 Results

4.3.1 Crossover in Grain & Bulk Behaviors

We begin by presenting some of the dynamical properties of our system. In particular, we look at the mean-squared displacements (MSD) of the grains. We will always report MSDs on a cycle-by-cycle basis, that is to say, the MSD is calculated

at the end of each cycle, where for reversible dynamics the system should return to zero net displacement. We find that for all γ_r studied, grains are at least slightly displaced relative to the beginning of the cycle, with increasing MSDs as a function of cycle number (where cycle number replaces time). First, we simply report the MSD relative to the initial (isotropic) state in Figure 4.2(a). These MSDs are noisy, making it difficult to extract a single β characterizing the evolution of the grain displacements. As a result, we also average over intervals of up to 200 cycles, each separated by 10 cycles in the oscillatory shear trajectory, to produce time- (or cycle-)averaged MSDs as shown in Figure 4.2(b). This procedure entails both a time and ensemble average, and single trajectory MSDs show similar behaviors. These averaged MSD curves exhibit a single exponent over the range of 200 cycles. Neglecting the first 10 cycles, as the very short time dynamics appear to be somewhat distinct from the longer time scale dynamics, we apply linear fits to the MSD curves and extract slopes.

These slopes as a function of γ_r provide the first evidence of a crossover between two regimes as γ_r is increased. For very small γ_r, the dynamics are highly subdiffusive, as has been previously observed in cyclic shear studies [23]. However, for γ_r=0.15, the exponent β is nearly 1, suggesting diffusive dynamics. As γ_r continues to increase, β stays unchanged at approximately 1.

This crossover in grain dynamics as γ_r is increased also manifests itself in the bulk properties of the shear flow, as shown in Figure 4.2(c-d). During each cycle, the packing fraction ϕ increases to a peak value, which depends on γ_r, and then decreases again. Averaged over many cycles, this process of compaction followed by

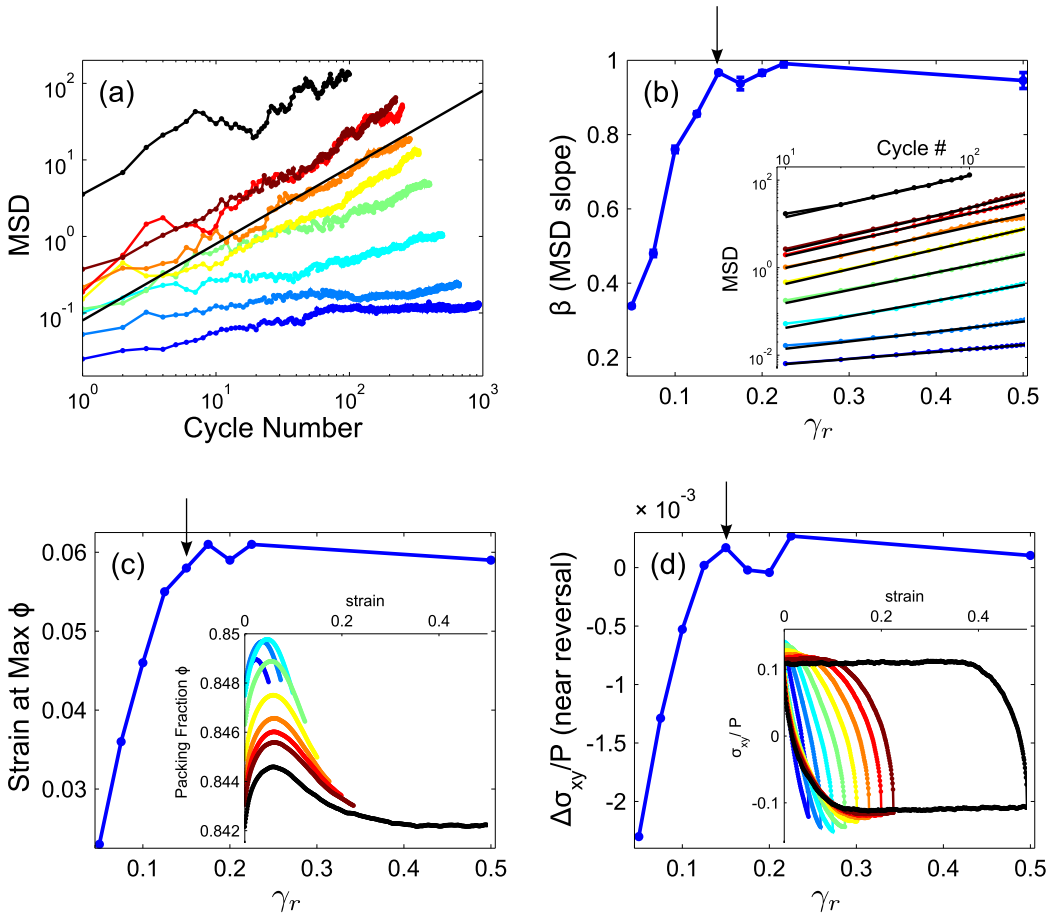

Figure 4.2: Crossover grain and bulk behaviors at $\gamma_r = 0.15$ (arrows). (a) MSD measured relative to the initial isotropic state. Different colors correspond to different reversal amplitudes, with blue (bottom curve) being the lowest and black (top curve) being the highest. A solid black line with a slope of 1 is added for reference. (b,inset) Time (or cycle-)averaged MSDs. The best linear fits are shown for each reversal amplitude. (b,main) The slopes from the linear fits (β) are shown as a function of reversal amplitude. Error bars stemming from the linear fits are shown. (c,inset) Packing fraction and (d,inset) shear stress σ_{xy} averaged over many cycles as a function of strain γ, for varying γ_r. (c,main) γ_r dependence for strain at peak ϕ and (d,main) slope of σ_{xy} at reversal.

dilation appears to begin and end at the same value of ϕ and for smaller γ_r exhibits a γ_r-dependent strain value at which the peak ϕ is reached. This strain at peak ϕ is plotted against γ_r in Figure 4.2(c), and a similar crossover from a γ_r-dependent regime near γ_r=0.15 is again observed.

Another observed bulk property that shows this crossover behavior is the shear stress σ_{xy}. The rate of change of σ_{xy} again shows a γ_r dependence. We illustrate this result by calculating the difference in σ_{xy} between the last two average strain steps before reversal, which again shows a crossover from a γ_r-dependent regime near γ_r=0.15, as illustrated in Figure 4.2(d). We also note that averaged over many cycles, σ_{xy} is quite hysteretic, as in the case of cyclic uniaxial loading [86]. Very quickly the stress state of the system, even at the beginning and end of each cycle, is anisotropic, oscillating on average between two extremal values of σ_{xy}.

Finally, we note that long time transients exist particularly for small γ_r. The essential conclusion from these results is that a crossover in dynamics and bulk properties as a function of γ_r occurs. Our finding is insensitive to the transient: ϕ and σ_{xy} increase for lower γ_r over many cycles initially, but the strain at peak ϕ and slope of σ_{xy} quickly become independent of cycle number. As for the dynamics, the MSD curves shift to lower squared displacements, but the slopes do not change significantly.

4.3.2 Comparing to Models of Subdiffusion

With such a strong correspondence between changes in bulk properties, and a crossover from a subdiffusive regime to simple diffusion, our next goal is to identify models that can capture the relevant subdiffusive dynamics for small γ_r. A concise survey of stochastic processes that result in subdiffusive dynamics is presented in [87]. These models are all able to exhibit a subdiffusive regime described by an MSD $\propto t^{\beta}$, $0 < \beta < 1$, but are motivated by different physics. In brief, there are two basic classes of self-similar processes that can exhibit anomalous diffusion: (I) processes with time-dependent diffusion coefficients, and (II) non-Markovian continuous-time random walks (CTRWs), which exhibit heavy-tailed waiting time distributions. The PDFs for these processes must obey a particular scaling form that reflects the self-affinity:

$$t^{H} P\left(r,t\right) \propto \psi\left(\xi = \frac{r}{t^{H}}\right) \tag{4.1}$$

The function $\psi\left(\xi = r/t^{H}\right)$ will have different forms for the different models discussed. Within the two broad classes discussed above are fractional Brownian motion (FBM), a subclass of (I), and fractional time processes (FTP), a subclass of (II), which exhibit a self-similarity exponent $H = \beta/2$. In addition, both processes can be generalized to linear fractional stable motion and ambivalent processes, respectively, by introducing heavy-tailed displacement distributions in analogy to Lévy flights. These processes are of generic fractional order and do not satisfy the self-similar relationship $H = \beta/2$ exhibited by FBM and FTP.

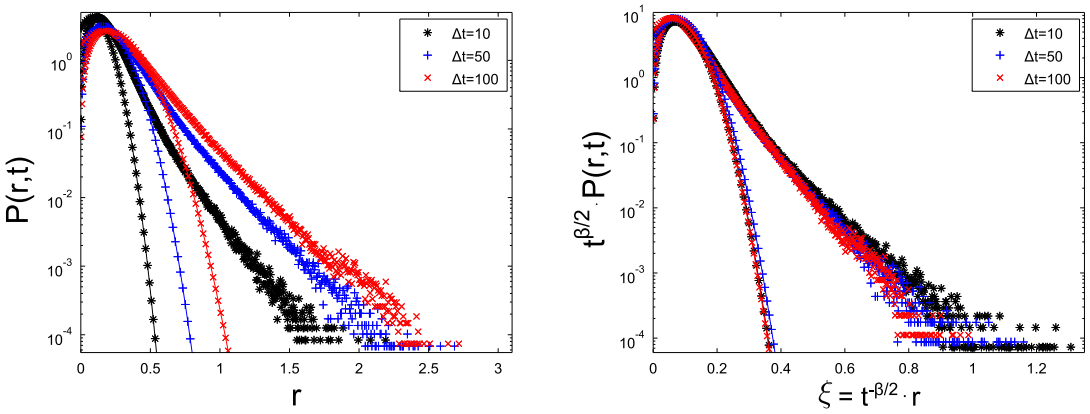

Figure 4.3: (Left) The unscaled displacement distributions for cycle intervals $\Delta t =$ 10, 50, and 100 (black asterisks, blue +'s, and red ×'s). (Right) The displacement distributions scale according to Equation 4.1, using the slope from the time averaged MSD for $\gamma_r = 0.075$. The markers with solid curves represent Gaussian fits about the mode.

Motivated by this fact, we scale each of the PDFs using the exponents gained from the time-averaged MSDs. As an example, Figure 4.3 shows PDFs for the time intervals $\Delta t = 10$, 50, and 100 for the case of $\gamma_r = 0.075$, scaled according to Equation 4.1 with $H = \beta/2 = 0.24$. Collapses for other γ_r are of similar quality. Based on this scaling, we conclude that neither linear fractional stable motion nor an ambivalent process is the appropriate model for the subdiffusive dynamics observed here, but that FTP and FBM are both viable candidates.

Furthermore, we can directly compare these displacement distributions to what would be expected for a FBM process. While the PDF of a FBM process is Gaussian at any time interval, the simulated PDFs, both unscaled and scaled, deviate significantly from a Gaussian. This calls the applicability of FBM into question.

4.3.3 Cage Dynamics & Waiting Times

Turning our attention to FTP as a candidate model, we consider the physical implications of waiting time distributions. Consider a random walker that moves under the guidance of FTP, with the ability to wait in one place rather than continually moving. The amount of time that the walker spends at a particular location is chosen from a heavy-tailed distribution. This description shares similarities with the 'cage-breaking' scheme used to describe long relaxation times in granular and glassy systems. In this scheme, particles such as the grains in our simulation "rattle" inside a cage of their neighbors on a shorter time scale, intermittently escaping out and into a new cage. The time spent in cages is then akin to a "waiting time."

Previous studies of cyclic shear under a different geometry and dynamics have attempted to characterize the cage sizes [23]. However, the notion of a cage can be difficult to define in a system where all of the particles are in motion. The cage is then itself a transient feature, rather than characterized by frozen-in defects. To determine a proper choice of cage size, we implement a method used by Allegrini, Douglas, and Glotzer [88]. We measure the average number of cycles $\langle\tau\rangle$ it takes a grain to reach an absolute displacement ϵ. After a grain has reached an initial displacement ϵ, it finds itself in a new starting cage, and a subsequent displacement ϵ constitutes the next cage-breaking event. Repeating this procedure for several values of ϵ, we select the cage size ϵ_c corresponding to the maximum of the logarithmic derivative $\Delta = \frac{d\log\langle\tau\rangle}{d\log\epsilon}$. For the example of $\gamma_r = 0.075$ shown in Figure 4.4, we find $\epsilon_c = 0.35$.

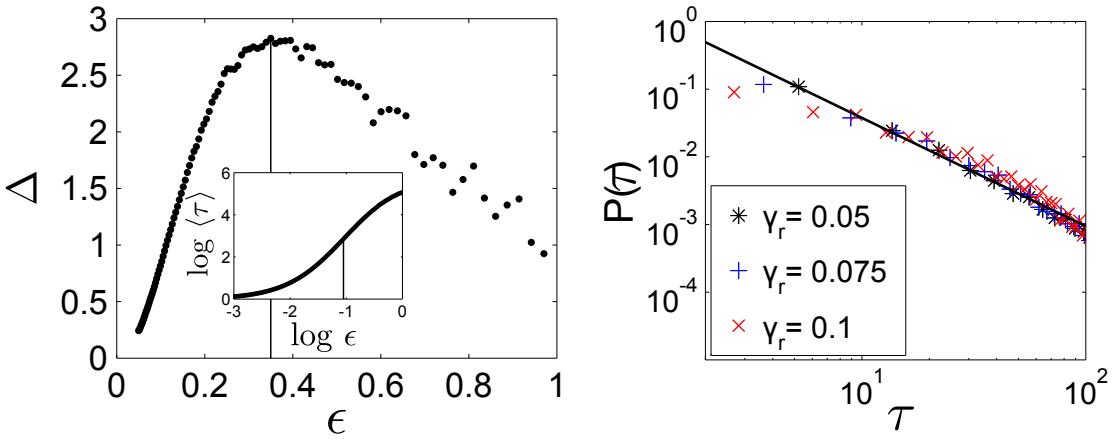

Figure 4.4: (Left,inset) The mean waiting time $\langle\tau\rangle$ as a function of candidate cage size ϵ for $\gamma_r = 0.075$. (Left,main) The logarithmic derivative Δ, with the location of ϵ_c marked with a solid line in both plots. (Right) The waiting time distributions for $\gamma_r = 0.05$, 0.075, and 0.1. They fall on a coinciding power law of slope -1.6.

Using this dynamically determined ϵ_c, we then investigate the properties of the resulting waiting time distributions. For all three shear amplitudes shown in Figure 4.4, we find that the distributions are, in fact, heavy-tailed, as would be expected for an FTP. However, the tails exhibit no dependence on the MSD slope β. This contradicts standard CTRW models, which are characterized by heavy-tailed waiting time distributions of the form $P(\tau) \sim \tau^{-(1+\beta)}$ [89].

4.3.4 Modifying the MSD

To further explore the validity of a cage breaking scheme, we calculate a modified MSD (mMSD) for every grain with respect to its neighborhood of nearby grains, as illustrated in Figure 4.5. In the initial isotropic state of the packing, the 6 nearest grains are found for grain i. A centroid for these nearby grains is calculated at every

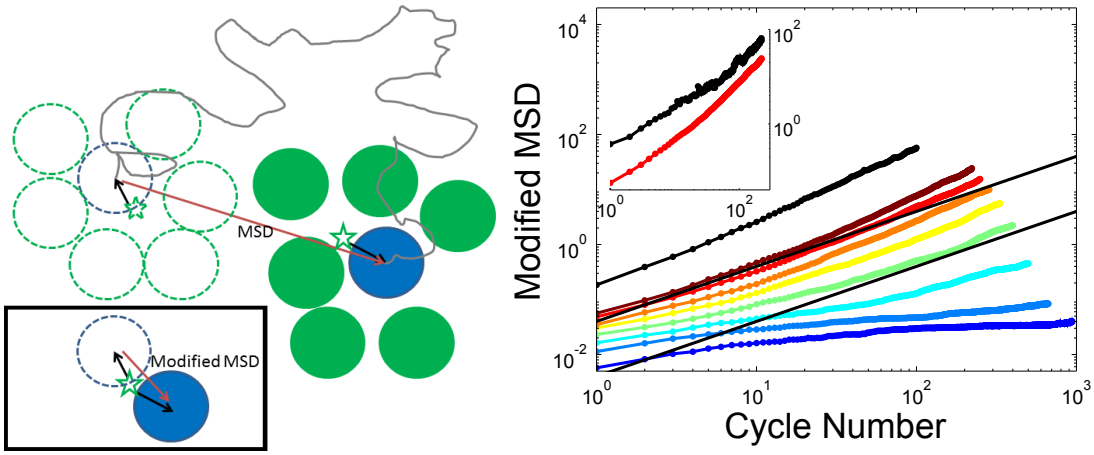

Figure 4.5: (Left) An illustration of the modification (inset) to the standard MSD approach (main). Open circles correspond to the initial configuration and filled circles represent the new configuration some time later. The reference grain (blue) is marked with arrows and the green star is the centroid of neighboring grains (green). (Right,main) The mMSD, relative to the packing configuration at $t = 0$, is shown. Solid lines have a slope of 1. (Right,inset) MSD (top curve) and mMSD (bottom curve) for $\gamma_r = 0.225$.

strain step, and the displacement of grain i relative to the centroid is calculated. In this way, we characterize the motion of a grain relative to its nearby grains, which is found to be highly isotropic and provides better insight into the nature of the local fluctuations in grain displacements.

Figure 4.5 shows that the mMSD curves are very smooth, with total squared displacements almost an order of magnitude smaller than those found with the MSD. This suggests that the motion of the grains are coordinated with the motions of their neighborhoods of grains, which is itself changing size and shape over time. Interestingly, unlike the MSD, the mMSD exhibits a continuous change from subdiffusive to superdiffusive motion, with superdiffusion for $\gamma_r \geq 0.15$. Understanding the origin of superdiffusion in this context is a goal for future investigations.

4.4 Discussion & Conclusions

We have presented a systematic study of reversal amplitude γ_r in a model amorphous system under cyclic shear. Results for bulk and grain dynamical properties suggest a crossover from subdiffusive to diffusive behavior near $\gamma_r = 0.15$. Interestingly, the MSD exhibits a crossover in particle dynamics with increasing γ_r, similar to the crossover from "caged dynamics" to diffusion as a function of time reported in thermally driven systems such as colloids [90]. However, a mMSD measurement suggests that a cage-breaking scheme may not provide the appropriate description of grain dynamics under cyclic shear. Instead of rattling in their cage, grain displacements are almost an order of magnitude smaller when measured

relative to their cage.

The observed displacement distributions and their scaling behaviors are not consistent with a simple cage-breaking model that is typically used for thermal systems, as shown in Figure 4.3. If we then consider the amount of time a grain spends within its neighborhood to be analogous to a cage lifetime, we find that the distribution of cage lifetimes appears to be scale invariant, with an apparent power-law distribution shown in Figure 4.4. This observation is consistent with the FTP model, where waiting times are assumed to be heavy tailed, although the exponent of the observed cage lifetimes is not consistent with FTP. Still, the observation that the cage lifetimes lack a single characteristic time scale is at odds with the standard caging scenario as presented in [90], where the cages have a single characteristic lifetime for a particular density.

Beyond the implications for granular dynamics suggested by heavy-tailed waiting time distributions, such as long-time correlations, the crossover in MSD slope from less than 1 to 1 coinciding with crossovers in bulk density and stress properties has further implications. Since the origin of the collapse of the displacement PDFs is their self-affinity, and the self-affinity exponent controls the slope of the MSDs ($H = \beta/2$), we suggest that this self-affinity may be the origin of the crossover in all bulk properties as a function of γ_r. The reason for such a strong dependence on the self-affinity exponent H is not yet clear to us. We suggest that a more complex picture of particle dynamics in cyclic athermal flows is needed, which will require more focus on the importance of global boundary forcing versus particle-scale thermal forcing, as well as driving amplitude.

In a thermal system, temperature drives the system at the particle-scale, while cyclic shear drives the system at the boundary. In other words, the driving force is applied at large scales. The results presented in this chapter indicate that in dense systems of many particles, such large scale forcing can lead to fundamentally different particle motion and collective rearrangements compared to thermal forcing. More broadly, our method for computing mMSD relative to a particle's neighborhood may provide a tool for extracting local dynamics within athermal systems. Similar questions concerning the origins of subdiffusion in dense systems are ubiquitous in biological physics as well. Subdiffusion has been observed in, for instance, the cytoplasm of living cells [25, 91] and mRNA dynamics in *E. Coli* [24, 92].

Chapter 5

Initial Measurements of Rotational Motion

This chapter is based on work contained in the publication: Experimental measurements of orientation and rotation of dense 3D packings of spheres. M. Harrington, M. Lin, K.N. Nordstrom, and W. Losert, *Granul. Matter* **16**, 185-191 (2014), ©2014 by Springer. I gave Michael Lin guidance in performing the experiments, and together we developed and performed the analysis.

5.1 Introduction

Current experimental research on dense granular flows has placed a heavy interest in the quantification of individual grain motion. Details of the microscopic origins of granular motion are typically lost in bulk rheological measurements, but researchers now have rigorous imaging techniques for acquiring particle-scale dynamics at their disposal. In particular, capturing the motion of grains inside a three-dimensional (3D) system is a challenge that has been addressed with techniques such as X-ray tomography [40], magnetic resonance imaging (MRI) [39], confocal microscopy [41], and refractive index matched scanning (RIMS) [42]. These techniques have provided additional insight to local structure, both static [93, 94, 95] and dynamically evolving under driving forces [77, 96, 97, 98, 99, 100], velocity profiles [39, 43, 101, 102, 103, 104], reversibility [17], size segregation [105, 106, 107],

and response to impact [44]. All of these methods capture the translational motion of grains, which is often sufficient in the appropriate context. However, granular materials consist of particles large enough to be considered athermal [4], so every grain should be thought of as a solid body that exhibits an orientation that may change over time under the mechanics of rigid body motion.

Consider a collection of hard grains in a system of dimensionality D, which dictates the number of degrees of freedom accessible for translation, D, and rotation, $\frac{D(D-1)}{2}$. A pair of grains in contact mutually exert a normal repulsive contact force on each other, as well as a tangential frictional force at the grain surface. Each one of those grains is likely touching other grains as well, so it feels additional normal and tangential forces from those contacts. The sum of the tangential forces yields a net torque on the individual grain, which can lead to rotational acceleration when torques are unbalanced, or static rotational equilibrium when torques are balanced.

Measurements of individual grain rotation have been made in some previous work, but much of the recent formal discussion is limited to rotations within a granular gaseous state. For example, the internal energy of a real 2D driven dense gas has equal contributions from each degree of freedom in rotational and translational motion [38]. Equipartition is not generally observed in 3D dilute gases [108], but linear velocity vectors and particle rotation axes are correlated [109]. Whether equipartition is broken by density or dimensionality is not immediately clear. There are also observations from simulations that indicate the prevalence of rotations in the shear-banding of a dense system. The presence of inter-particle friction can affect the geometry of shear-bands under a biaxial load [110, 111] and split-bottom shear [112],

indicating that energy is either dissipated through sliding contacts or stored as rotational energy within rolling subregions [27, 110]. The observation of rotational motion within the shear band of a real biaxial load predates simulations [113], while particle rotations in the shear zone of a split-bottom geometry has been recently verified in the alignment of rod-like particles [99, 100, 114]. However, the relative contributions of particle rotations and frictional dissipation in the formation of split-bottom shear zones have not been formally studied.

Measuring 3D orientation and rotational motion in real systems brings about additional challenges, particularly for dense systems of spherical grains. Unlike rods, solid spheres do not have an intrinsic orientation that arises from geometric asymmetry, so the orientation is indiscernible by current 3D imaging techniques. In this chapter, we propose and demonstrate a technique for extracting spherical grain orientations and a portion of their rotational motion in a dense 3D system. Then, we report on the performance quality of our orientation algorithm in initial experiments. Finally, we connect the bulk particle rotation profiles with well-known azimuthal velocity profiles in the split-bottom geometry. This provides an indication of the origin of individual rotational motion in a system driven by circular shear.

5.2 Setup & Procedure

5.2.1 Granular System

The dense granular pile ($\phi = 0.60 \pm 0.01$) is comprised of 6 mm polymethyl methacrylate spheres, each of which has a 1.5 mm diameter hole drilled all the way

Figure 5.1: Photograph of the drilled beads used for capturing rotational motion.

through, as shown in Figure 5.1. The cylindrical hole through the sphere introduces a slight inertial anisotropy of $\frac{I_{2,3}}{I_1} = 0.929$ (see section 5.5).

The grains are placed in a circular split-bottom shear geometry, illustrated in Figures 2.2 and 3.1. This geometry is known for producing wide shear zones [46, 47], and has recently been used for studying rotational motion and ordering of anisotropic particles [99]. The square tank has side lengths of 15 cm and the shearing disk diameter is 9 cm. The disk is separate from the tank floor and rotates at a rate of 1 mrad/s, either steadily or in an oscillatory fashion. The results shown in this chapter are derived from 2 full rotations of steady shear. The average pile height is selected to be about 4.5 cm, so the height to disk radius ratio $\frac{H}{R_s} \approx 1$. This is the same setup used previously in several studies examining shear-driven granular flow in 3D [17, 43, 77, 107]. Before any data is collected, we pour the grains into the tank and shear steadily for 2 full disk rotations to eliminate any fabric memory from the initial loading of the packing.

5.2.2 Acquisition of 3D Images

The grains are immersed in a fluorescent index-matched fluid, Triton X-100 with Nile Blue 690 Perchlorate. A small amount of hydrochloric acid is also added to stabilize the mixture. The density of the grains ($\rho_g = 1.18$ g/cm^3) is greater than that of the fluid ($\rho_f = 1.07$ g/cm^3), so the grains settle at the bottom of the tank under gravity. Although the system is fluid-immersed, the flows observed under our choice of shearing rate (1 mrad/s) are rate-independent, as well as similar to those of a dry pile [43].

Cross sections within the pile are illuminated by two laser sheets (635 nm) which are aligned on opposite sides of the tank. A high-sensitivity camera then captures an image of the horizontal cross section from the top-down. The laser sheets scan vertically through the entire pile, in 200 μm steps, to capture a full 3D image. This imaging procedure is repeated between 2° increments in shear.

Typical cross sections using solid and drilled grains are shown in Figure 5.2. Note that both images yield circular cross sections of each individual grain, while the cavities in the drilled grains are clearly visible.

5.2.3 Particle Extraction

The locations of individual grain centroids are obtained by applying a 3D Gaussian convolution kernel [76]. Since the kernel primarily detects the edge of spheres to determine centroid location, the positions of drilled spheres are not significantly affected compared to solid spheres.

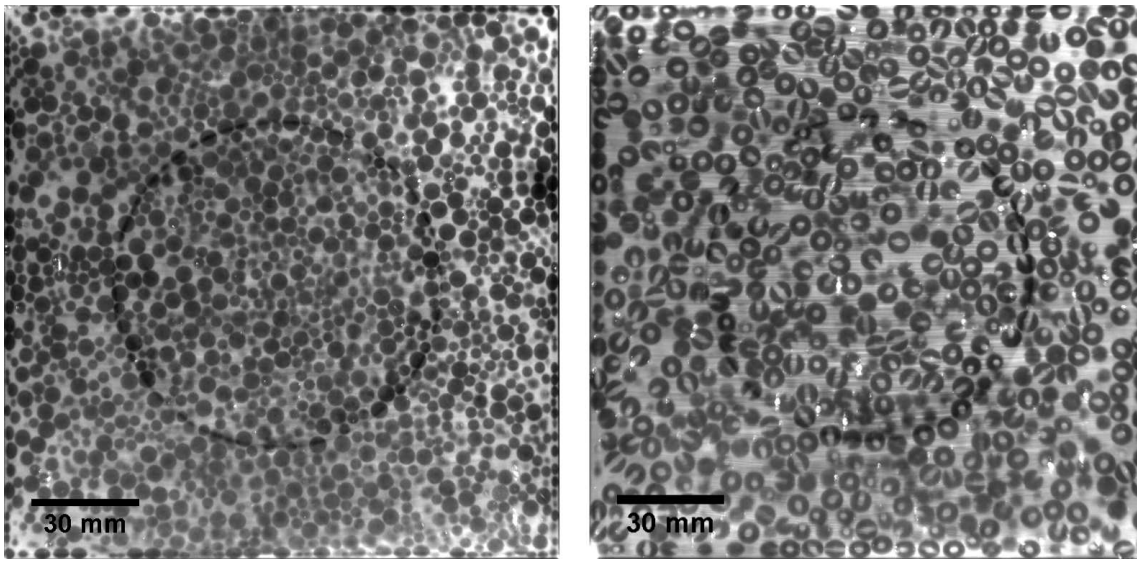

Figure 5.2: (Left) A cross section within the bidisperse system used in chapter 3, which contains solid spheres of size $D_S = 3.2$ mm and $D_L = 4.8$ mm. (Right) A cross section of the pile with drilled grains, $D = 6$ mm and hole diameter 1.5 mm.

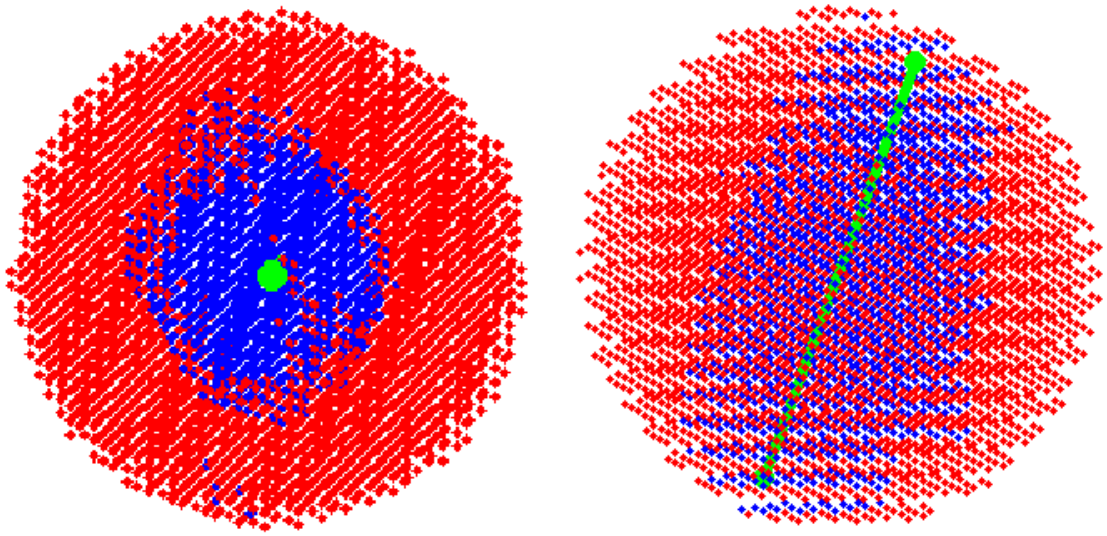

Figure 5.3: Two views of the orientation extraction of a single grain.

In the case of drilled beads, the presence of a cavity allows us to then extract particle orientations. Once the centroid of a grain is determined, a spherical neighborhood surrounding the centroid, with a radius slightly smaller than the grain radius, is isolated. Principal component analysis (PCA) is then performed on bright voxels that correspond to the hole, leaving out dark voxels that represent the solid portion. The grain orientation vector is given by the eigenvector associated with the maximum eigenvalue of the covariance matrix, which is defined by the spread of bright band voxels in 3D space. A binary 3D image of a single grain with an extracted orientation using this method is shown in Figure 5.3.

5.2.4 Tracking Translational & Rotational Motion

Individual grains are identified and tracked in 3D using Particle Tracking Velocimetry [48]. This and other tracking algorithms uniquely label each particle and determine the translational motion. Next, the change in orientation axis between consecutive frames is directly calculated for every tracked grain. An additional check on the angular displacement is performed to avoid overestimating the rotational motion. This kind of error can result if PCA yields orientation vectors in consecutive frames that point in nearly opposite directions.

It is important to now emphasize that, while this PCA method is sufficient to capture two rotational degrees of freedom, there is an additional degree of freedom along the axis of the drilled hole that cannot be measured.

5.3 Results

5.3.1 Extraction Performance

As stated previously, the presence of the cylindrical hole does not significantly affect grain position. Using ordinary solid spheres, particle center resolution is typically about 100 μm, which is consistent with the drilled grains. Furthermore, the orientations of stationary grains far from the disk are seen to fluctuate within a total angular deflection of 1 mrad (0.06°).

In a given frame, both positions and orientations can be found for at least 90% of the grains, a slightly lower success rate from prior studies using solid spheres. In some cases, the position of a grain can be found, while the grain cavity is not adequately resolved to definitively assign an orientation. This effect is caused by the presence of additional solid-fluid interfaces, which further amplifies image distortion due to any disparity in the indices of refraction. The current success rate provides a very good basis to examine initial bulk measurements of rotations throughout the pile. In the future, however, we would like to capture an even higher percentage of grain orientations and rotations under improved index-matching. Then, reliable measurements of rotational motion within neighborhoods can be taken and reported.

Sample images depicting our extraction and tracking capabilities are shown in Figure 5.4. Notice in the track image, on the right side of Figure 5.4, how some grains maintain a very consistent orientation, while others rotate very quickly. Some grains even maintain consistent orientations for several frames, followed by intermittent rotations.

At this point, one aspect of our drilled spheres that should be addressed is the possibility of grains touching each other at the small cavity created by the drill hole. Figure 5.5(a)-(b) demonstrate two general ways that two grains can come into contact: (i) as with any solid sphere contact, the spherical surfaces of the grains are in contact with each other, and (ii) the points of contact actually lie on the lip of the drill hole, such that the surface of one grain slightly penetrates the drill hole cavity of the other. Grains that are in contact under the latter condition are what we refer to as "sticking." To address this issue, we measure the probability density of the angle ϕ between a grain's orientation and the relative position vector to its neighbor contacts. For sticking contacts, these vectors are very close to being either parallel or antiparallel. Specifically, a sticking contact is defined as one in which $|\cos\phi| \geq \frac{R}{\sqrt{R^2+h^2}}$, where R is the grain radius and h is the hole radius. This condition also includes the particular case where the orientations of both grains and the points of contact in between are all aligned. For the grains used in this study, this limit is found to be $|\cos\phi| \geq 0.97$. Figure 5.5(c) illustrates that a bias does indeed exist for sticking contacts at any given time, while much of the distribution in between remains close to uniform. However, the distribution does not change over large values of strain. In fact, Figure 5.5(d) illustrates that the magnitude of the bias does not vary appreciably. Rather than driving the grains into a locked arrangement, the system exhibits a steady amount of sticking contacts which are not intrinsically preferred or stable. We also observe that sticking contacts that persist throughout the entirety of the experiment lie in an immobile region of the tank, far from the disk center.

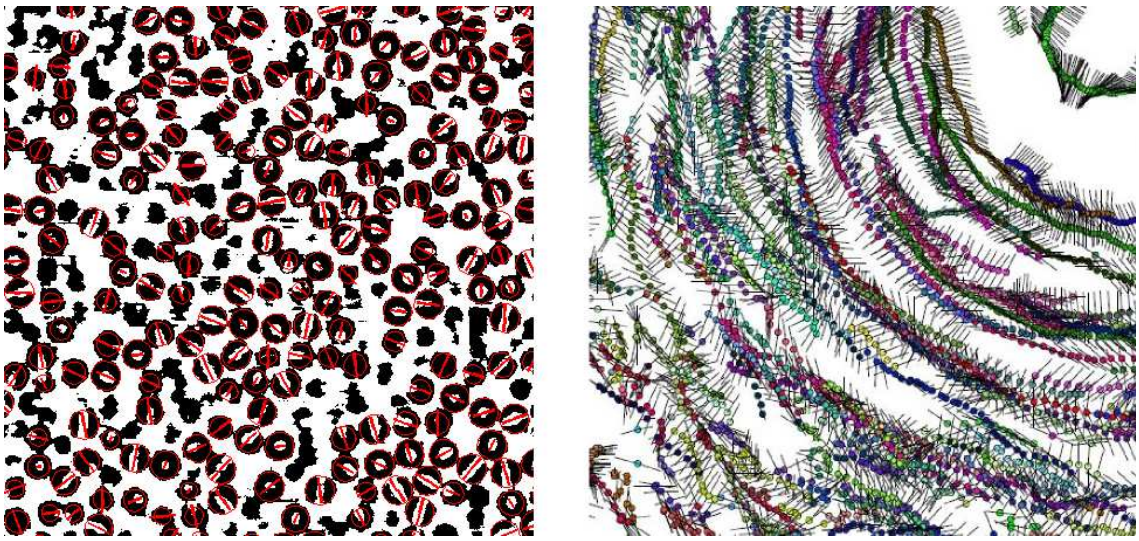

Figure 5.4: (Left) Grain positions and orientations overlaid over a binary cross section of the pile, after processing. This image corresponds to a height of 1.5 cm and a 10 cm x 10 cm area centered about the shearing disk. Circular outlines are drawn around extracted grain positions, while the lines are projections of the orientation vector. Dark circles with lines laid across indicate nearly horizontally oriented grains, with the cavity lying just out of plane. (Right) Several sample trajectories passing through a height of 1.5 cm within a 3.0 cm x 2.9 cm area. The small circles are centroids, while the lines protruding from them are the grain cavity orientations. The colors indicate distinct tracks. The top right corner corresponds to the disk center.

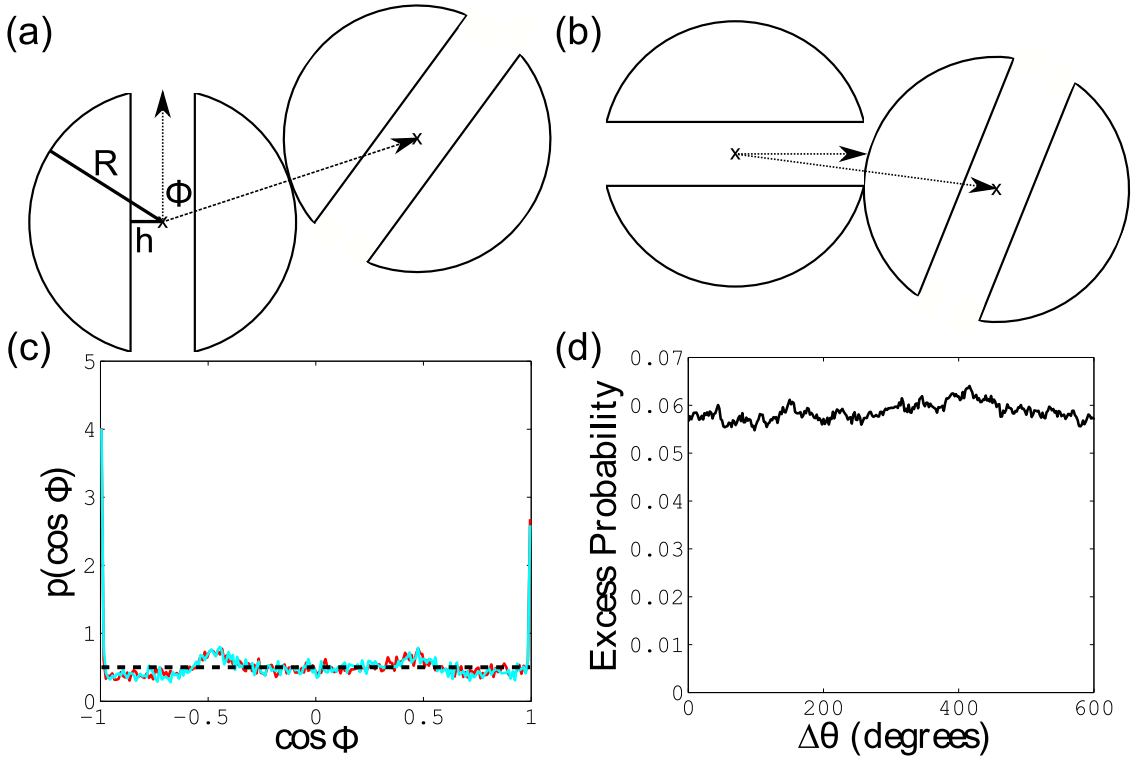

Figure 5.5: (a) A cross sectional view of two drilled spheres whose contact point lies entirely on the grain surface. R is the grain radius, h is the drill hole radius, and ϕ is the angle between the orientation axis of one grain and the relative position vector between the two grains. (b) Two "sticking" grains whose points of contact are on the edge of the drill hole. (c) The probability density of $\cos\phi$ at an initial distribution (dark red) and after 600° of strain (light cyan), which mostly overlap each other. For reference, a perfectly uniform distribution is also shown (dotted black). (d) Over the course of 600° of strain, the probability of a grain contact sticking, in excess of the ideal uniform case.

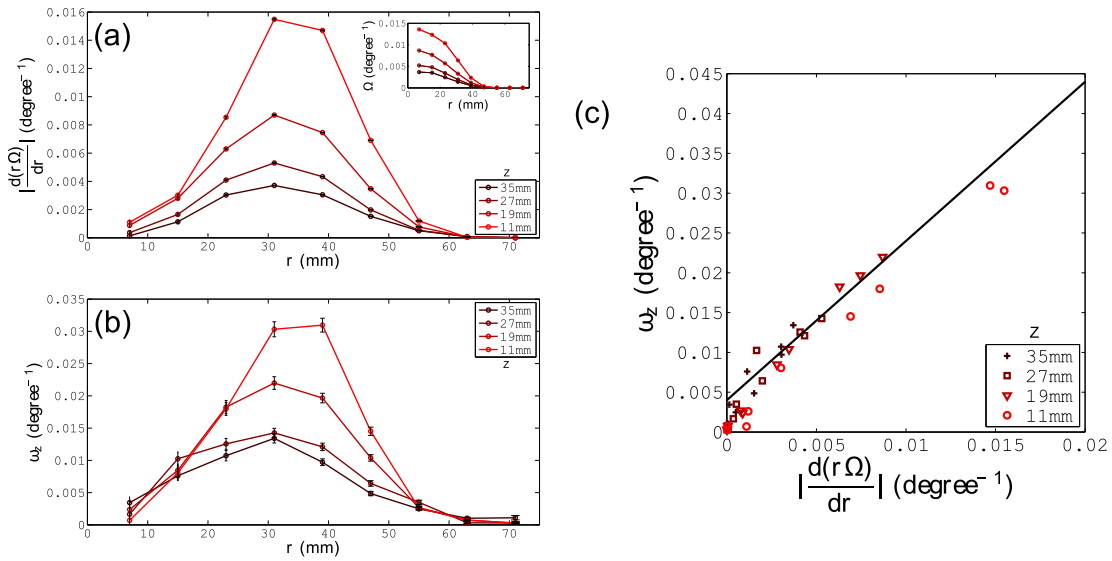

Figure 5.6: (a,Inset) Azimuthal velocity (Ω) profiles within the pile as a function of r for various heights in z. (a,Main) The gradient of tangential velocity, $r\Omega$, with respect to r. (b) The average z-component of rotational motion (ω_z) as a function of r at various heights in z. (c) ω_z versus tangential velocity gradient. The solid black line has slope 2, as prescribed in Equation 5.1.

5.3.2 Rotational Coupling with Velocity Profiles

Given our capability to track grains in both space and orientation, we would now like to quantify the resulting velocity profiles, as well as the average rotation within several portions of the pile. As with previous experiments in circular split-bottom geometries, the grains exhibit azimuthal velocity profiles, as a function of r at fixed z, in the form of error functions [46, 47]. As a result, the corresponding velocity gradient is sharply peaked in the middle of what is determined to be the shear zone. The shear zone is the intermediate region that separates two contrasting regions: one near the center of disk where grains undergo solid-body rotation, and a

stationary region far from the disk center. The center of the shear zone moves slightly toward the disk center and the shear zone widens with increasing z. Figure 5.6(a) demonstrates the behavior of the azimuthal velocity, as well as the corresponding gradients in tangential velocity.

Strikingly similar behavior is then seen in the average θ-rotation of individual grains (that is, the z-component of particle angular velocity, ω_z). As shown in Figure 5.6(b), ω_z peaks at approximately the same locations in r and z as the tangential velocity gradient, and exhibits a width that is similar to that of the shear zone. This suggests that the gradients in tangential velocity may be what is directly driving ω_z.

In fact, a relationship between azimuthal rotation and tangential velocity gradient can be derived using only elementary mechanics, under special conditions. Consider the physical system illustrated in Figure 5.7. A sphere of radius R is wedged between two plates which are aligned and parallel. The plates are located at perpendicular distances of r_1 and r_2 from a reference origin. If the plates translate at different velocities, v_1 and v_2, and the sphere does not slip between either of the plates, it will rotate instantaneously along an axis perpendicular to r_i and v_i. The amount of rotation is

$$\omega = \frac{v_2 - v_1}{R} = \frac{\Delta v}{R}$$

The tangential velocities of the plates can also be written in terms of angular velocities relative to the origin, $v_i = r_i \Omega_i$. Also, the sphere radius can be substituted with the plate spacing $\Delta r = 2R$.

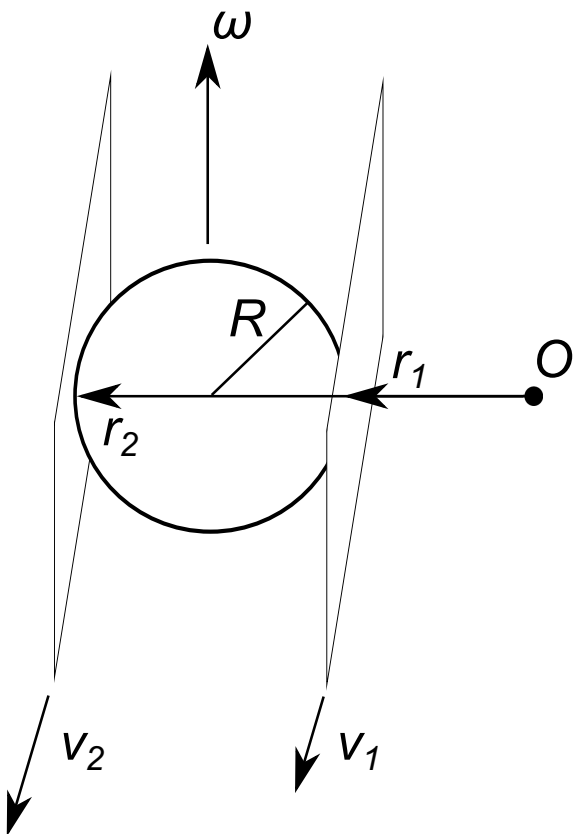

Figure 5.7: A sphere which rotates without slipping between two moving parallel plates.

$$\omega = 2\frac{\Delta(r\Omega)}{\Delta r}$$

Therefore, in terms of derivatives,

$$\omega = 2\frac{d(r\Omega)}{dr} \tag{5.1}$$

Similar relationships for shear-driven systems have been indicated by simulations [115, 116] and experimentally observed in 2D [117]. In our system, ω_z indeed exhibits a linear relationship with the tangential velocity gradient, as shown in Figure 5.6(c). Good agreement between the empirical data and a line with slope 2

indicates that gear-like motion within the shear zone may be the mechanism behind the azimuthal rotation of individual grains.

5.4 Discussion & Conclusions

As advances in the study of granular materials continue, individual rotational motion is one aspect that is likely to receive increased attention in the near future. Measuring rotational motion experimentally brings about many difficulties, particularly for dense 3D systems of symmetric particles. To address these challenges, we have devised and performed initial experiments on the driving of drilled grains under circular split-bottom shear. The RIMS imaging technique allows us to extract the orientation of the grain cavity using PCA and measure a portion of a grain's rotational motion in 3D. While some limitations currently exist, this method has demonstrated that it is capable of making precise measurements of individual grain orientation and, in turn, rotational motion.

In particular, we can directly measure the average amount of azimuthal rotation within the shear zone, as well as investigate the potential origin of such motion. Namely, Figure 5.6(c) indicates that rotations within the shear zone are directly coupled to the radial gradient of tangential velocity, with strong agreement between experimental data and what is theoretically predicted for a perfectly rolling system. It stands to reason, then, that varying the amount of interparticle friction would have a direct influence on shear zone size, which has previously been observed in simulations [112].

With the procedure described in this chapter, one persistent limitation is that rotational motion about the drilled axis cannot be measured. In other words, the 3D images of a grain that rotates between consecutive frames entirely along the axis of the drill hole are indistinguishable. Consequently, full rotational motion of the grains cannot be captured. This limits the amount of physics that may be extracted, including locally coupled rotations, equipartition, and velocity correlations. In future studies, we will explore further modifications of the apparatus to allow us to probe full 3D rotational motion of the spheres.

5.5 Appendix: Moments of Inertia

Recall the moment of inertia for a solid sphere of mass M and radius R,

$$I_s = \tfrac{2}{5}MR^2$$

For the purpose of these calculations, it will be more convenient to express this in terms of density ρ,

$$I_s = \frac{8}{15}\rho\pi R^5 \tag{5.2}$$

First, we start with the axis along the hole, about which rotation is visually indeterminant under the current setup. For convenience, the moment of inertia of the material which is removed will be subtracted from the solid sphere inertia.

$$I_1 = I_s - I_{hole,1}$$

The moment of inertia of a differential mass element of the holed-out material is given by that of a thin solid disk,

$$\mathrm{d}I_{hole,1} = \tfrac{1}{2}r^2\mathrm{d}m$$

$$\mathrm{d}I_{hole,1} = \tfrac{1}{2}\rho\pi r(z)^4\mathrm{d}z,$$

where

$$r(z) = \begin{cases} h, & |z| \leq \sqrt{R^2 - h^2} \\ \sqrt{R^2 - z^2}, & |z| > \sqrt{R^2 - h^2} \end{cases} \tag{5.3}$$

h is the hole radius in the interior of the sphere and z is the coordinate along the drill axis. Then, after performing the integrals,

$$I_1 = I_s\sqrt{1 - x^2}(1 + \frac{1}{2}x^2 - \frac{3}{2}x^4) \tag{5.4}$$

In the intermediate steps, I_s is substituted in using Equation 5.2 and x is defined to be the hole size ratio, $x = \frac{h}{R} < 1$.

Next, we move to the moment of inertia for rotations about the axes perpendicular to the hole.

$$I_{2,3} = I_s - I_{hole,2,3}$$

We again use a thin disk as the mass element for the hole. The differential moment of inertia is then defined by applying the perpendicular and parallel axis theorems,

$$\mathrm{d}I_{hole,2,3} = \tfrac{1}{2}\mathrm{d}I_{hole,1} + z^2\mathrm{d}m$$

$$\mathrm{d}I_{hole,2,3} = \tfrac{1}{2}\mathrm{d}I_{hole,1} + \rho\pi r(z)^2z^2\mathrm{d}z$$

Now, we evaluate the integrals using the same limits for z and definition of $r(z)$ from Equation 5.3. Again, I_s is substituted for the solid sphere inertia and x

is substituted for the hole size ratio.

$$I_{2,3} = I_s\sqrt{1-x^2}(1 - \frac{3}{4}x^2 - \frac{1}{4}x^4) \tag{5.5}$$

For our grains in particular, $\rho = 1.18$ g/cm^3. The grains have a diameter of 0.6 cm. For a solid sphere, Equation 5.2 gives

$$I_s = 4.80 \cdot 10^{-3} \text{ g} \cdot \text{cm}^2$$

The hole diameter is 0.15 cm, which gives a size ratio of $x = 0.25$. From Equations 5.4 and 5.5,

$$I_1 = 4.77 \cdot 10^{-3} \text{ g} \cdot \text{cm}^2$$

$$I_{2,3} = 4.43 \cdot 10^{-3} \text{ g} \cdot \text{cm}^2$$

Chapter 6

Extension to 3D Rotational Motion

As described in the previous chapter, rotational information cannot be captured if a bead rotates about the axis of its cavity. In fact, only two degrees of rotational freedom can be measured with these beads. This chapter describes further work, part of which was performed with Michael Lin, to expand this technique to measuring 3D rotational motion.

6.1 Motivation

Given two states of an object, measuring the average velocity of the object is very straightforward. If the position of the object's center of mass is known in both states, one can simply take the difference between the two positions and divide by the time interval,

$$\boldsymbol{v}_{avg} = \frac{\boldsymbol{x}_f - \boldsymbol{x}_i}{\Delta t} \tag{6.1}$$

When applied to experimental data, this simple finite difference procedure yields an approximation of the instantaneous velocity of the object, with uncertainty given by the spatial and temporal resolution of the acquisition system.

Unfortunately, finite difference methods are generally not useful for 3D rotational motion. Suppose the object in question is a thin rod that is fixed at its center

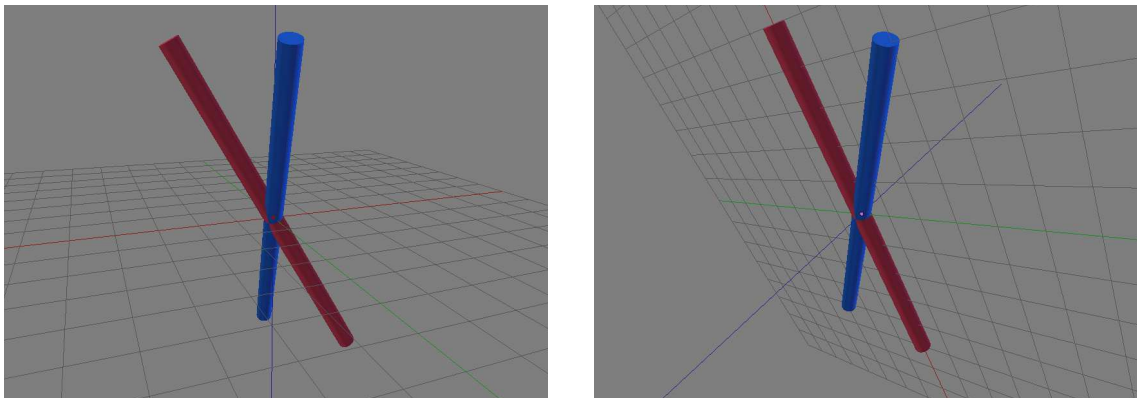

Figure 6.1: (Left) Two rods that are displaced an angle of 30° from the z-axis. One of the rods is drawn by making a 75° rotation about the z-axis. (Right) A nearly identical picture drawn using a modified coordinate system, where the plane defined by the rods is shown. In this case, the two rods are separated by a rotation about the normal direction of about 35.4°.

but free to rotate, as shown in Figure 6.1. The state of the rod can then, in part, be represented by an orientation vector pointing outward from the origin and along the rod. Consider two states in which, for the sake of simplicity and without loss of generality, the rod keeps a constant angle with respect to the vertical coordinate, z. Euler's rotation theorem states that any rotation of a 3D object, about some fixed point, can be characterized by a single rotation about an axis passing through the fixed point [118]. The finite difference method for determining translational velocity relies on the minimum path an object can take from the initial to the final position. Similarly, we would like to know the minimum rotation required to go from the initial orientation to the final one.

However, this cannot be done with our simple example. For instance, the rod

could rotate azimuthally about z, or the rotation vector could be perpendicular to both initial and final orientations. In fact, there are infinitely many rotation axes and displacements that could satisfy this transformation. Without any additional information or constraints on the object, this is a measurement that cannot be made with only one orientation vector. In the case of the 3D granular shear cell system, the grains are certainly free to rotate about all three rotational degrees of freedom, so modifications to our image acquisition and analysis must be made.

6.2 Background on 3D Rotational Kinematics

Before describing how 3D rotations are measured experimentally, it is important to also appreciate some background on what is well known with regard to 3D rotational kinematics [119]. The easiest place to start is with objects that are confined to only rotate in 2D. In this case, there is only one rotational degree of freedom and a counter-clockwise rotation of θ can be represented by the applying the following rotation matrix to a 2D vector,

$$R = \begin{pmatrix} \cos\theta & -\sin\theta \\ \sin\theta & \cos\theta \end{pmatrix} \tag{6.2}$$

This rotation can be equivalently written in the following 3D form, where the z coordinate is not affected,

$$R = \begin{pmatrix} \cos\theta & -\sin\theta & 0 \\ \sin\theta & \cos\theta & 0 \\ 0 & 0 & 1 \end{pmatrix} \tag{6.3}$$

However, a generic 3D rotational transformation is more complicated, and can be written in this form,

$$R = \begin{pmatrix} r_{11} & r_{12} & r_{13} \\ r_{21} & r_{22} & r_{23} \\ r_{31} & r_{32} & r_{33} \end{pmatrix} \tag{6.4}$$

While Equation 6.4 refers to nine seemingly independent parameters, there are some generic properties that a rotation matrix R must meet. For instance, R must be orthogonal, which means

$$\sum_{i=1}^{3} r_{ij} r_{ik} = \delta_{jk} \tag{6.5}$$

where δ_{jk} is the Kronecker delta. It then follows that the inverse R^{-1} is equal to the transpose R^T and the determinant $\det R$ is equal to 1, assuming the rotation is not followed by an inversion of points (i.e., that it is a "proper rotation"). These conditions reduce the number of independent parameters in R from nine to six.

There are many formalisms for 3D rotational motion that provide some physical interpretation for these nine terms. These formalisms can come in many forms, but they all presume that a desired rotation is known and applied to system or object of interest. This is important in a wide variety of settings, from the rotation

of a 3D rendering, to the time evolution of quantum states [120].

Perhaps the most recognized formalism for the rotation of objects in real 3D space is that which is defined by the Euler angles. The Euler angles (or Tait-Bryan angles in some contexts) can be defined with respect to many conventions. The most common convention is zxz, where an overall rotation is achieved by performing three separate rotations: one about the z-axis, one about the new x-axis, and one more about the new z-axis. The final rotation matrix in this formalism is given by

$$R = \begin{pmatrix} c\psi c\phi - c\theta s\phi s\psi & -s\psi c\phi - c\theta s\phi c\psi & s\theta s\phi \\ c\psi s\phi + c\theta c\phi s\psi & -s\psi s\phi + c\theta c\phi c\psi & -s\theta c\phi \\ s\theta s\psi & s\theta c\psi & c\theta \end{pmatrix} \tag{6.6}$$

where $s\cdot = \sin(\cdot)$ and $c\cdot = \cos(\cdot)$. Similar matrices can found using other Euler or Tait-Bryan conventions, where three angles and three axes are specified. This mode of thinking also points to each rotation matrix having six independent parameters.

There is one formalism that represents rotation of an object as a vector equation. Given initial and rotated vectors $\boldsymbol{x}$ and $\boldsymbol{x}_{rot}$, respectively, a unit rotation axis $\boldsymbol{k}$, and angular displacement ϕ,

$$\boldsymbol{x}_{rot} = \boldsymbol{x}\cos\phi + (\boldsymbol{k}\times\boldsymbol{x})\sin\phi + \boldsymbol{k}\,(\boldsymbol{k}\cdot\boldsymbol{x})\,(1-\cos\phi) \tag{6.7}$$

This is known as Rodrigues's rotation formula, which, unlike the Euler and Tait-Bryan formalisms, directly applies the object's minimum rotation. Another formalism that specifies the minimum rotation uses the Euler parameters,

$$
\begin{aligned}
e_0 &= \cos\left(\phi/2\right) \\
e_1 &= k_x \sin\left(\phi/2\right) \\
e_2 &= k_y \sin\left(\phi/2\right) \\
e_3 &= k_z \sin\left(\phi/2\right)
\end{aligned}
\tag{6.8}
$$

Collectively, these parameters form a quaternion, a unit norm ($e_0^2+e_1^2+e_2^2+e_3^2 = 1$) structure that contains a scalar component (e_0) that specifies the rotation angle and a vector component ($\boldsymbol{e} = e_1\hat{x} + e_2\hat{y} + e_3\hat{z}$) which, given the rotation angle, specifies the rotation axis. Combined with Equation 6.7, these parameters then define a rotation matrix given by the Euler-Rodrigues rotation formula,

$$
R = \begin{pmatrix}
e_0^2 + e_1^2 - e_2^2 - e_3^2 & 2\left(e_1e_2 + e_0e_3\right) & 2\left(e_1e_3 - e_0e_2\right) \\
2\left(e_1e_2 - e_0e_3\right) & e_0^2 + e_2^2 - e_1^2 - e_3^2 & 2\left(e_2e_3 + e_0e_1\right) \\
2\left(e_1e_3 + e_0e_2\right) & 2\left(e_2e_3 - e_0e_1\right) & e_0^2 + e_3^2 - e_1^2 - e_2^2
\end{pmatrix}
\tag{6.9}
$$

Some of these formalisms will be brought up once again when the experimental method for determining rotational motion is discussed.

6.3 3D Imaging

From the discussion in the previous sections, it is clear that insufficient orientation data is a limitation in the experimental measurements of rotational motion described in chapter 5. In the context of tracking rotations within macroscopic particle-laden flows, researchers have addressed this by either using geometrically

asymmetric objects [121] or, in the case of spheres, by marking the surface of each with a distinguishable pattern [122]. In both cases, additional information about the orientation of each object can be readily extracted.

It is then clear that our drilled spheres would also have to be somehow modified to elucidate additional orientation information. In the previous section, it was shown that a rotation matrix has nine entries, but only six of those are independent parameters. Therefore, minimal modification should be made to each sphere so that a second orientation vector can be found for each sphere, yielding a total of six measured quantities to completely specify the orientation of each grain.

This was achieved by adding a small notch in the surface of each bead, as shown in Figure 6.2. The diameter of the new hole is 1 mm, smaller than the original hole, and goes about 1 to 1.5 mm deep. The drilling of each sphere was done manually, so there is non-negligible variation in the depth of the notch, as well as its orientation relative to the original cavity.

The beads are then placed in the same apparatus as before. However, given the small drill hole axes and relatively high viscosity of Triton X-100, the fluid can have difficulty permeating every cavity. While preparing an experiment, fluid-immersed beads are placed in a vacuum, which effectively removes large air pockets, while smaller bubbles can be treated with hand-stirring. Finally, the beads and fluid are simultaneously transferred into the shear cell.

From here on, the experimental procedure is identical to previous studies, with regard to how the system is driven quasistatically by the shearing disk, while the RIMS system periodically captures 3D images.

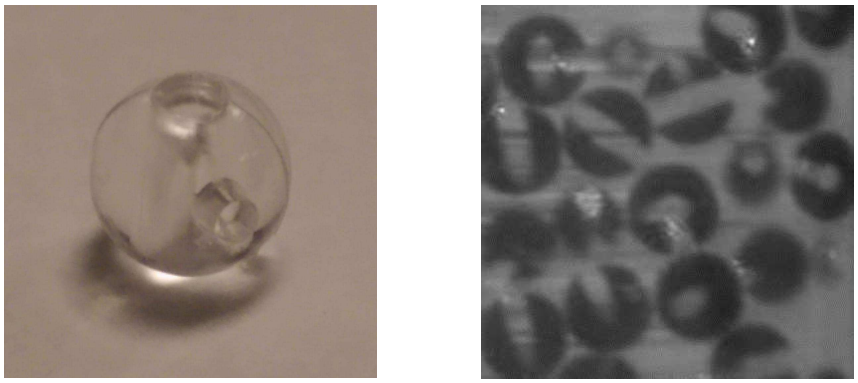

Figure 6.2: (Left) Photograph of the bead with an additional notch drilled in the side, in addition to the original hole. (Right) A portion of a cross section captured using the RIMS system, demonstrating that the additional notch is visible.

6.4 Analysis Procedure

Once all the 3D images are captured over the course of an experiment, the images must be analyzed to locate and track individual grains. As with the initial study on rotational motion, much of analysis procedure is the similar to that used for solid spheres. The spheres are located using a 3D convolution kernel, then a tracking algorithm, either PTV or Lagrangian particle tracking, uniquely labels the spheres. Of course, additional steps must be added throughout this process so that rotational motion can also be measured.

6.4.1 Extraction of Orientations

The orientation of each sphere is found simultaneously with position extraction, similar to how orientations were found in the initial rotations study. Initially, the centroid of a candidate sphere is found. When a proper threshold is applied

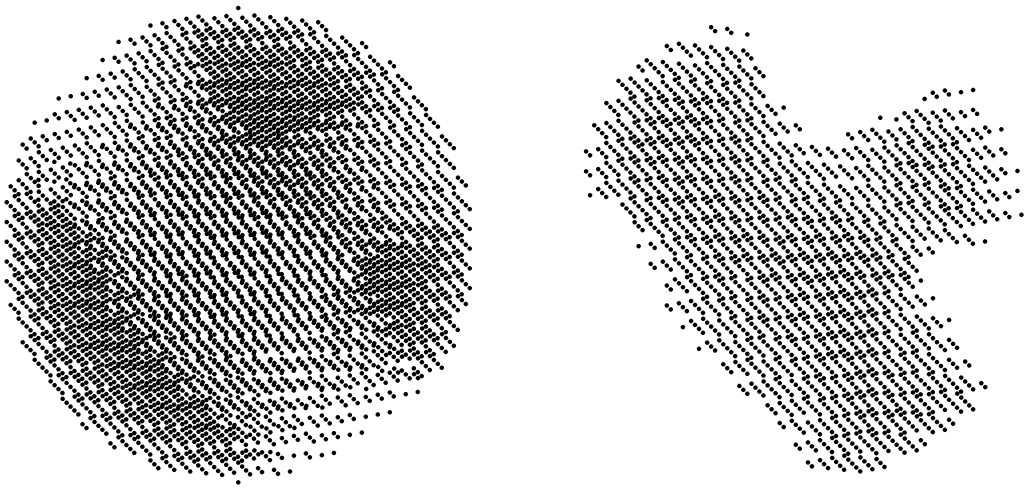

Figure 6.3: (Left) A binary image of a single bead with two axes that can be extracted. (Right) Another binary image of the same sphere, inverted to clearly show the orientations to be extracted.

to the image, the original long axis and short notch should be apparent from a binary image, as shown in Figure 6.3. The following image processing steps are then performed on the binary image.

First off, it should be noted from the binary image that, due to hand-drilling, image resolution, and noise, it may be difficult to immediately separate two distinct clusters of voxels. For this reason, a shell mask is first applied, so that only voxels near the surface of the sphere remain. This should leave three patches remaining, as shown in Figure 6.4(a). Once the centroid of each patch is calculated, the two that are most co-linear with the sphere center are identified. These two centroids correspond to opposite ends of the long axis.

Next, a cylindrical mask pointing from one co-linear patch to the other, and

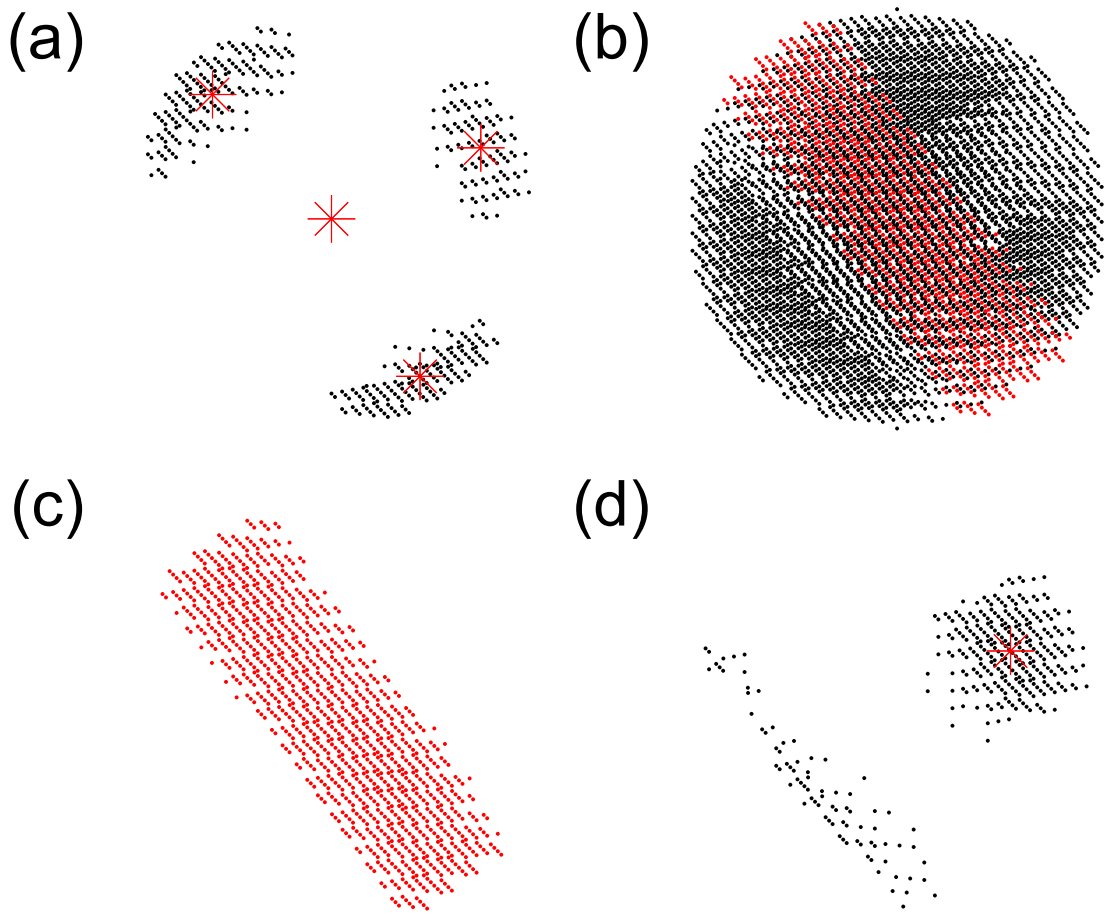

Figure 6.4: Various intermediate images of the orientation extraction process: (a) A shell mask is applied to the sphere, leaving three small patches of voxels. The centroid of each patch, along with the sphere centroid, are shown with asterisks. (b) A cylindrical mask is generated based on the two patch centroids that are most co-linear with the sphere centroid. (c) The resulting voxels from applying a cylindrical mask to the original binary image. (d) When almost all voxels along cylinder are deleted from Figure 6.3, the small notch can be identified and located. The centroid of the small notch is shown with an asterisk.

with similar dimensions to the long bead axis, is generated, as shown in Figure 6.4(b). This cylinder represents a first-pass approximation for the orientation of the long axis. This mask is then applied to the original binary image, so all voxels lying outside the cylinder are temporarily removed. The remaining voxels, shown in Figure 6.4(c), then lie entirely within the long axis. Just as with the original rotations study, PCA is performed on these voxels, yielding a refined measurement of the long axis orientation.

Returning again to the original sphere image, we use the refined measurement of orientation to eliminate almost all voxels along the long axis. As shown in Figure 6.4(d), this effectively leaves just the small notch voxels. The mask used in this case can be slightly larger than the one used to find the first orientation, but not so large that voxels within the small notch are also lost. The small notch voxels are treated differently from the long axis, since the hand-drilling necessarily implies that there is some variation in the orientation of this notch relative to the long axis. In addition, we would like to treat the extracted orientations as pointing outward from the sphere center, so that rotations can be measured about the sphere centroid. With all of these considerations in mind, the centroid of the remaining small notch region is computed relative to the sphere center. Once normalized, this is defined as the sphere's "second" orientation. The final results of the orientation extraction for this sphere are shown in Figure 6.5, along with the original binary images.

Once positions and orientations have been identified for all frames, tracks can be stitched together using a particle tracking algorithm as before. This will also produce tracks of the two orientations, such as those shown in Figure 6.6.

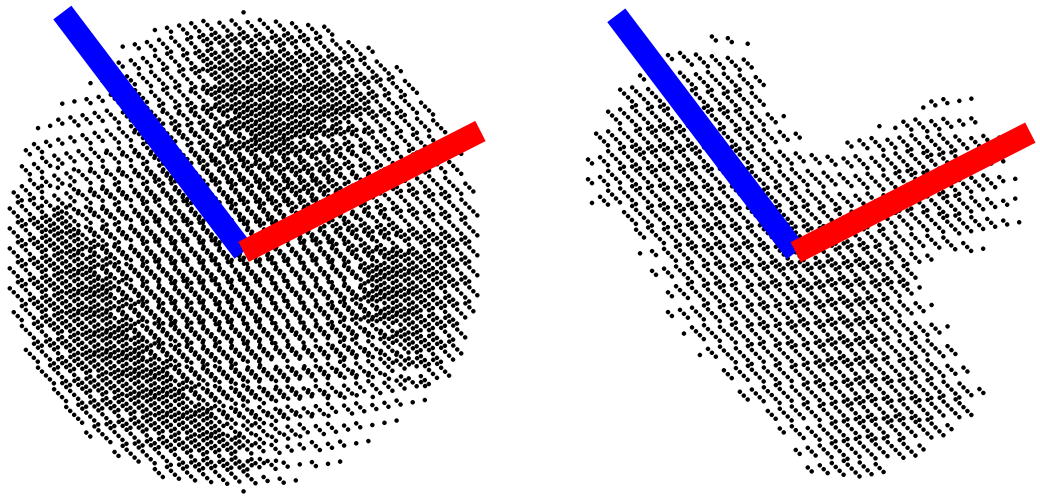

Figure 6.5: Same as Figure 6.3, overlaid with the two extracted orientations.

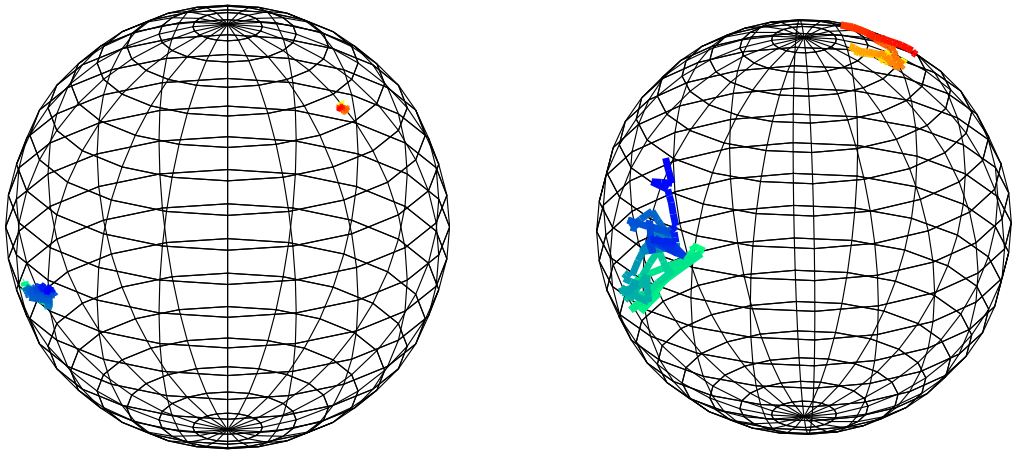

Figure 6.6: Sample tracks of two grains, one that is far from the disk and experiences very little motion (left) and one that is located within the shear zone but near the top of the pile (right). Time evolution of the long axis is represented by the curve that changes from light yellow to dark red, while the short notch is denoted by light green to dark blue.

6.4.2 Determination of Rotational Axis & Displacement

After all of the grains have been tracked and labeled, one can determine the rotational motion of each grain between subsequent frames. This can be accomplished by applying the Kabsch algorithm [123, 124], which solves for the minimum rotation matrix R between the two frames. This method can be applied to the rotation of physical objects [122], but also finds broader application in the transformation of generic point patterns [125], and especially in the field of bioinformatics, providing a standard for comparing protein structures [126]. The method behind the algorithm is briefly described here.

Consider the orientation vectors in the initial and final frame, which are labeled $\boldsymbol{\sigma}_{1,i}$, $\boldsymbol{\sigma}_{2,i}$, $\boldsymbol{\sigma}_{1,f}$, and $\boldsymbol{\sigma}_{2,f}$. Then, the covariance between initial and final orientations can be computed,

$$C = \begin{pmatrix} \boldsymbol{\sigma}_{1,i} & \boldsymbol{\sigma}_{2,i} \end{pmatrix} \begin{pmatrix} \boldsymbol{\sigma}_{1,f} \\ \\ \boldsymbol{\sigma}_{2,f} \end{pmatrix} \tag{6.10}$$

Then, single value decomposition is performed on the covariance matrix C,

$$C = VSW^T \tag{6.11}$$

where V and W are orthogonal matrices whose columns contain, respectively, the left- and right-singular vectors of C, while S is a diagonal matrix containing the singular values of C. The matrices V and W also happen to define the rotation vector that most closely maps the initial coordinates to the final coordinate via a single rotation, with the minimum residual error. Specifically, R is given by

$$R = WV^T \tag{6.12}$$

Ultimately, this yields a rotation matrix in the form of Equation 6.4 that minimizes the root mean square distance between the final orientations and the ones that result from the rotation matrix acting on the original orientations. Alternatively, this can be thought of as maximizing the covariance between these two sets of coordinates. The rotation matrix R can then be related to the Euler parameters, defined in Equation 6.8, with the following relations,

$$\begin{aligned} e_0 &= \frac{\sqrt{\mathrm{Tr}R + 1}}{2} \\ e_1 &= \frac{r_{23} - r_{32}}{4e_0} \\ e_2 &= \frac{r_{31} - r_{13}}{4e_0} \\ e_3 &= \frac{r_{12} - r_{21}}{4e_0} \end{aligned} \tag{6.13}$$

Note that this formulation breaks down if e_0 is exactly zero. From Equation 6.8, this would require a rotation of exactly $\pm\pi$ radians, so this should not occur when used in practice with experimental data that measures small increments of rotational motion. In applications where rotations of $\pm\pi$ radians should be allowed, this exception can be caught with alternate formulations of the Euler parameters in terms of the components of the rotation matrix.

It should be noted that the Kabsch algorithm can also take translation into consideration, making this method applicable to scenarios requiring the extraction of a rigid transformation between two sets of coordinates. However, given that both

orientations are defined to be unit vectors pointing from the sphere centroid, the translational component of the Kabsch algorithm is subverted.

6.5 Discussion

The approach described in this chapter for determining orientation and rotation appears to be very sound. Of course, the lack of uniformity in the dimensions of the additional notch is not ideal, but this method provides a way to work around that shortcoming. While the repeated instances of PCA in the orientation extraction algorithm can be computationally taxing, much of the process can be parallelized locally or on a cluster. Once these orientations are found, determining the rotational motion with Kabsch algorithm between between two frames is straightforward and computationally fast.

One aspect that requires further improvement is the overall quality of 3D images, which tends to deteriorate as the system images deeper into the system, under several layers of PMMA spheres. This is an indication of insufficient index-matching between the spheres and the fluid, since the images are clearer when imaging through fewer layers. This would indicate that modifying the experimental set-up has had an adverse effect on the 3D image quality, for one of a couple possible reasons. For one, the small drilled notch on each sphere adds many more solid-fluid interfaces, which amplify any slight deviation in refractive indices. In this case, more care is needed to ensure very close refractive index matching between the spheres and fluid. Another possibility is that the act of drilling the additional notch, perhaps

with slight heating and/or melting of the plastic, has changed the effective index of refraction in the neighborhood of the small notch. If the index of refraction of each individual grain is not very consistent, it becomes an impossible task to formulate an effective refractive index matching fluid.

To improve the data acquisition in future experiments, one possibility is to have each grain 3D printed, assuming optical properties can remain consistent within each grain. An added benefit would be a very reproducible pattern of notches within each grain. 3D printing granular materials has already seen application in the context of generating stable granular packings [127], and DSM Somos WaterClear Ultra 10122 could be a candidate printing material, since it has been used in other experimental studies to match refractive index with PMMA [128].

6.6 Appendix: Moments of Inertia

With an additional modification made to each sphere, the question of how the moments of inertia are affected must again be raised. For the purpose of these calculations, suppose an idealized cavity configuration as shown in Figure 6.7. There is a centered axis of radius h that passes all the way through sphere and a short notch of length l and radius a that is perpendicular to the original axis, and is also aligned with the sphere center.

Three principal moments of inertia are defined: one about the long axis, I_1, one about the short notch, I_2, and one about an axis that is perpendicular to both, I_3. For ease of presentation, we shall begin with the computation for I_2. Prior to

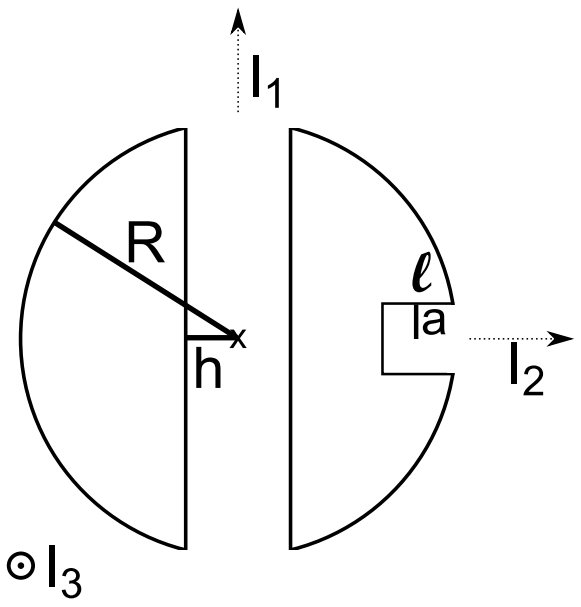

Figure 6.7: An illustration of an idealized grain with two cavities: one that goes all the way through the center and one that is a short notch near the surface.

adding the short notch,

$$I'_{2,3} = I_s\sqrt{1-x^2}(1 - \frac{3}{4}x^2 - \frac{1}{4}x^4) \tag{6.14}$$

where I_s is the moment of inertia of the solid sphere and $x = \frac{h}{R}$ is the ratio of the axis radius to the grain radius. Using the technique described in the previous chapter, the new moment of inertia would be given by subtracting that of the notch,

$$I_2 = I'_2 - I_{notch,2}$$

The moment of inertia of a differential element of the removed material is given by

$$\mathrm{d}I_{notch,2} = \tfrac{1}{2}r^2\mathrm{d}m$$

$$\mathrm{d}I_{notch,2} = \tfrac{1}{2}\rho\pi r(z)^4\mathrm{d}z,$$

where

$$r(z) = \begin{cases} 0, & h < z < R - l \\ a, & R - l \leq z \leq \sqrt{R^2 - a^2} \\ \sqrt{R^2 - z^2}, & \sqrt{R^2 - a^2} < z < R \end{cases} \tag{6.15}$$

z is again taken to be the coordinate integrated, this time along the notch axis, and R is the grain radius. After performing the integrals,

$$I_2 = I_s \left[\sqrt{1-x^2}(1 - \frac{3}{4}x^2 - \frac{1}{4}x^4) + \frac{1}{2}\sqrt{1-y^2}(1 + \frac{1}{2}y^2 - \frac{3}{2}y^4) + \frac{15}{16}y^4(1-\ell) - \frac{1}{2} \right] \tag{6.16}$$

where $y = \frac{a}{R} < 1$ and $\ell = \frac{l}{R} < 1 - x$ are new size ratios.

Next, we move to the moment of inertia for rotations about the long axis. Recall the expression for I_1 prior to the additional modification,

$$I_1' = I_s\sqrt{1-x^2}(1 + \frac{1}{2}x^2 - \frac{3}{2}x^4) \tag{6.17}$$

Similar to the above calculation, the moment of inertia after removing the notch is given by

$$I_1 = I_1' - I_{notch,1}$$

The differential moment of inertia of a notch element is found from the perpendicular and parallel axis theorems, and also applies to the final axis perpendicular to both long and short axes.

$$\mathrm{d}I_{notch,1,3} = \tfrac{1}{2}\mathrm{d}I_{notch,2} + z^2\mathrm{d}m$$

$$\mathrm{d}I_{notch,1,3} = \tfrac{1}{2}\mathrm{d}I_{notch,2} + \rho\pi r(z)^2 z^2 \mathrm{d}z$$

Now, we evaluate the integrals using the same limits for z and definition of $r(z)$ from Equation 6.15.

$$\begin{aligned} I_1 = \quad & I_s[\sqrt{1-x^2}(1+\tfrac{1}{2}x^2-\tfrac{3}{2}x^4)+\tfrac{1}{2}\sqrt{1-y^2}(1-\tfrac{3}{4}y^2-\tfrac{1}{4}y^4)+ \\ & \tfrac{15}{32}y^4(1-\ell)+\tfrac{5}{8}y^2(1-\ell)^3-\tfrac{1}{2}] \end{aligned} \tag{6.18}$$

Components of the previous two calculations can be combined to determine the final moment of inertia I_3,

$$\begin{aligned} I_3 = \quad & I_s[\sqrt{1-x^2}(1-\tfrac{3}{4}x^2-\tfrac{1}{4}x^4)+\tfrac{1}{2}\sqrt{1-y^2}(1-\tfrac{3}{4}y^2-\tfrac{1}{4}y^4)+ \\ & \tfrac{15}{32}y^4(1-\ell)+\tfrac{5}{8}y^2(1-\ell)^3-\tfrac{1}{2}] \end{aligned} \tag{6.19}$$

For PMMA grains with grain diameter 0.6 cm, $I_s = 4.80 \cdot 10^{-3}$ g $\cdot$ cm^2. Suppose a grain is constructed with ideal cavities given by $x = \frac{1}{4}$, $y = \ell = \frac{1}{6}$. From Equations 6.16, 6.18, and 6.19,

$$I_1 = 4.73 \cdot 10^{-3} \text{ g} \cdot \text{cm}^2$$

$$I_2 = 4.42 \cdot 10^{-3} \text{ g} \cdot \text{cm}^2$$

$$I_3 = 4.39 \cdot 10^{-3} \text{ g} \cdot \text{cm}^2$$

Chapter 7

Prospective & Outlook

This thesis has presented experimental and simulation studies that probe various signatures of microscopic rearrangements within granular shear flows. In chapter 3, it was shown that a cyclically driven bidisperse mixture can either remain mixed or slowly segregate, depending on the presence of distinct convective secondary flow profiles giving rise to particle-scale irreversibility. Chapter 4 then presents a systematic probing of cyclic shear amplitudes to demonstrate various crossover behaviors across a critical shear amplitude, including the transition from confined subdiffusive motion that is locally driven by particle cages, to cage-breaking events that are increasingly ballistic with respect to local neighborhood motion. Finally, chapters 5 and 6 describe work on experimentally measuring 3D rotational motion, which will provide insight to how grains utilize either sliding or rolling to break their contacts, and what effect the prevalence of collective rotational motion has on overall reversibility. It is immediately apparent that rotations, on average, couple with each other throughout the shear zone, providing additional modes of irreversible plastic deformations.

In this chapter, we discuss a few possibilities for future work that can expand on these findings. Much of the work presented in this thesis has focused on the affect of altering the boundary driving as a means of probing features of microscopic

rearrangements. For instance, chapters 3 and 4 identified unique behaviors in grain motion that emerge as a result of tuning cyclic shear amplitude. Logical steps to follow would thus entail efforts to alter local inter-particle interactions as a way to better understand the connections between global driving and local motion.

One of the advantages of the RIMS imaging technique is that, as long as the same material and fluid are used, one can be very creative with alternate experimental set-ups without too much effort. In particular, PMMA is an easy material to use for the fabrication of new experimental components. The study on rotations is itself a great example of how the RIMS system, after slight modifications, can now yield new insights into particle-scale motion. Of course, coding a simulation study also allows for alterations of the system to be readily made, as was already the case with varying cyclic shear amplitude. Possible alterations that can be made to both experimental and simulation set-ups to probe new modes of inter-particle interaction are discussed below.

7.1 Flows of Rods & Arbitrary Shapes

This section is based on unpublished work with Miguel González-Pinto. I gave Miguel guidance in running the experiments and developed initial code to extract rod-shaped grains, which was then revised and expanded by Miguel.

As demonstrated in the previous two chapters, image processing tools can be added to and/or adapted from our established library of code to image grains that deviate from solid spheres. In future experiments, there may be interest in exploring

the formation of shear zones with grains that have even an even more complex shape.

In particular, there is general interest in the study of granular materials composed of rod-shaped grains [129]. One reason for this interest is that many grains in reality are, in fact, not spherically symmetric. Examples of asymmetric grains, specifically ones that are rod-shaped, include uncooked rice and spaghetti, as well as tree branches and trunks that make up beaver dams. Researchers are also interested in the potential of granular rods to serve as an analogous system to liquid crystal behavior, albeit at a larger scale. Indeed, granular rods tend to order themselves when shaken [130, 131] or sheared [99, 100, 114]. Rod-like grains also provide a way of altering the local grain interactions, since rods in contact are capable of exerting torques on each other, even with little or no friction [132].

Using our RIMS shear cell set-up, we have performed initial experiments to explore the dynamics of rod-like grains. The rods are machined from PMMA, with a 4.8 mm diameter and length of 24 mm, for an aspect ratio of 5. The extraction procedure of rod orientation is very similar in principal to that used in [133]. First, the standard 3D spherical convolution is applied, which tends to locate endpoints of rods. Then, these points are paired with others that are a suitable distance away. For each potential matching endpoint, a cylindrical mask is created and applied to the 3D image. The partner endpoint with the best fit to a cylinder is chosen. Then, a refinement measurement is made for rod orientation and centroid. Some of this code, namely that which generates cylindrical masks, is also used for the extraction of cavity orientations within spherical grains. The extraction of a sample synthetic rod, as well as a typical cross section of a 3D scan, is shown in Figure 7.1.

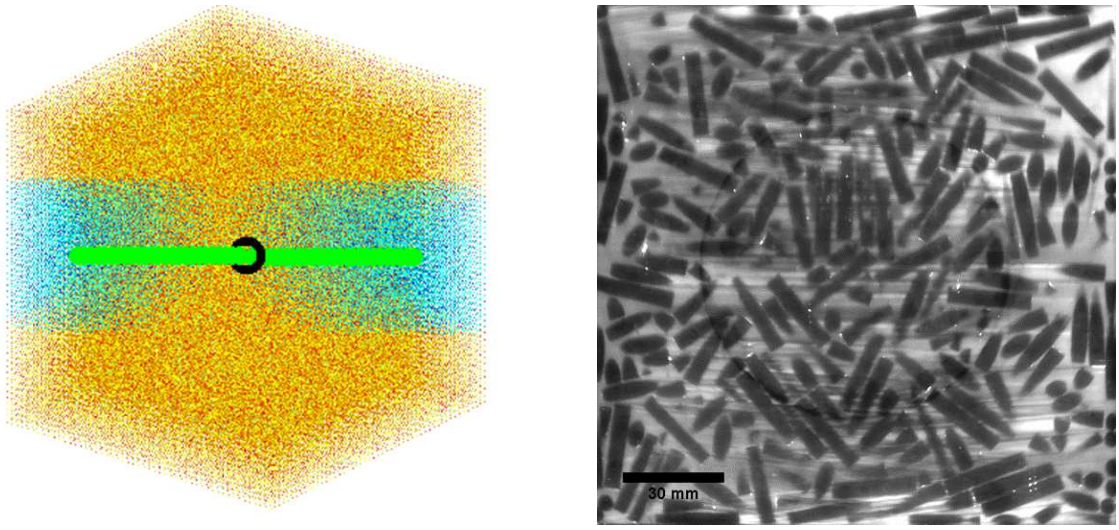

Figure 7.1: (Left) A synthetic rod, generated using intensity and noise levels that are typical in experiments, overlaid with the centroid and orientation found using the cylinder extraction method. (Right) A sample cross section from an experiment using PMMA rods in the RIMS shear cell set-up.

With these analysis tools in place, we began performing initial experiments with steadily applied shear to examine the degree of ordering in our system, and how it compares with results from other groups who do not force in the quasistatic regime. Indeed, our system exhibits progression toward nematic ordering, which can be expressed using several metrics, shown in Figure 7.2. For one, the average rod angle with respect to the average azimuthal stream line α is shown to tend toward to some non-zero value, fluctuating around $-10°$. The reason for this angle to not tend toward zero can be attributed to the shear gradient pointing along the polar radial direction, with stronger shear toward the disk center. When the shear is reversed after the rods reach an ordered state, the rods reorient themselves to go along the same angle with the reversed streamlines. Meanwhile, the polar angle ϕ does not

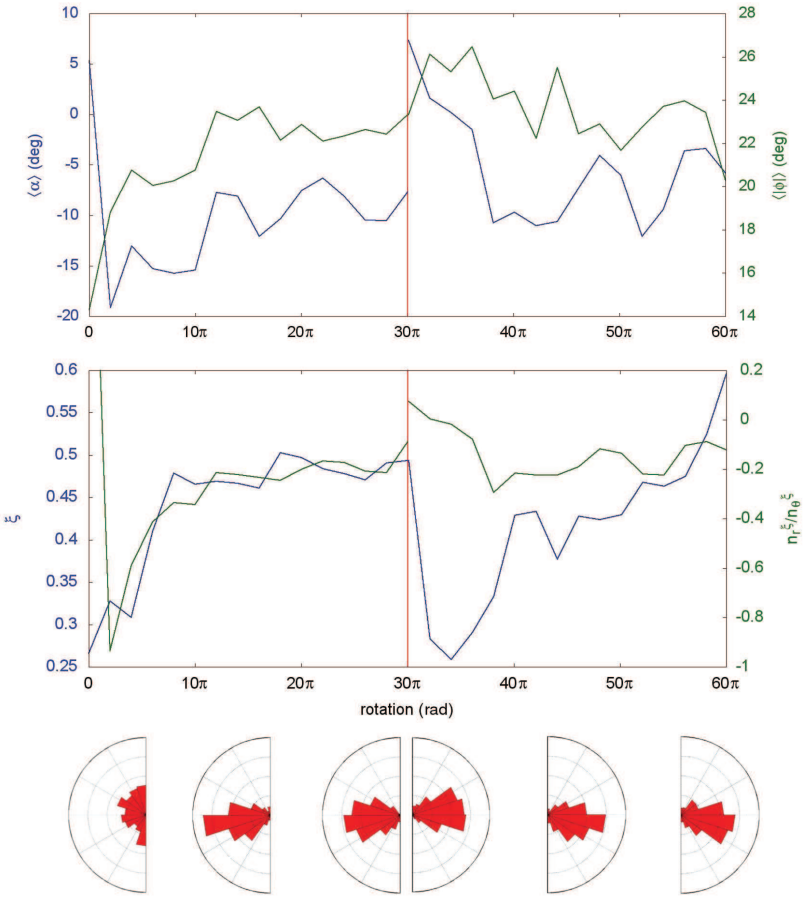

Figure 7.2: Over the course of applied shear and eventual shear reversal, the long-term evolution of (top) the average azimuthal angle α (with respect to the average circular streamline) and polar angle ϕ, and (middle) the global order parameter ξ and the ratio of radial to azimuthal components of the principal eigenvector. The vertical line across both plots denotes when shear is reversed. (Bottom) Snapshots of the full α distributions of the rods at various amounts of strain.

exhibit any ordering, as $\langle\phi\rangle$ is constantly about zero. However, as the rods dilate in order to undergo ordering rearrangements, the distribution of polar angles spreads out in a way that the average absolute value $|\phi|$ goes to about 20°.

There are also ways to quantify the global order without explicitly referring to the system geometry, to compare with systems in other contexts. One way is to define the following matrix in terms of the orientation of each rod,

$$Q_{\alpha\beta} = \frac{3}{2N}\sum_{i=1}^{N}\left(u_{i\alpha}u_{i\beta} - \frac{1}{3}\delta_{\alpha\beta}\right) \tag{7.1}$$

where N is the number of rods considered, $u_{i\alpha}$ is the $\alpha = \{r, \theta, z\}$ component of the orientation of the ith rod, and $\delta_{\alpha\beta}$ is the Kronecker delta. The largest eigenvalue ξ represents the amount of global order in the system, with its eigenvector $\boldsymbol{n}^{\xi} = \{n_r^{\xi}, n_\theta^{\xi}, n_z^{\xi}\}$ defining the preferred direction. Thus, n_r^{ξ}/n_θ^{ξ} can be used as an additional order parameter. Over the course of the experiment, we see that these quantities indeed trend toward an increasingly ordered state, with ξ approaching about 0.5 and n_r^{ξ}/n_θ^{ξ} going to some constant non-zero number, owing to the fact that α does not approach zero. Upon shear reversal, these quantities highlight the temporary disorder that must occur in order to settle back into a similarly ordered state.

There are still many local metrics that can be explored, which would be unique to our ability to image individual rods. For instance, aside from global ordering, one could explore the prevalence of cooperatively rotating rods as well as angular diffusivity, as a way of quantifying how "caged" the orientations are. Furthermore,

cyclic shear experiments would enlighten the question of irreversibility being a necessary condition for ordering, or if rods that compact under small shear amplitudes can also exhibit nematic ordering.

7.2 Confining Pressure

This section is based on published work with Allyson Rice. I gave Allyson guidance in running the experiments and in extracting flow profile characteristics.

Besides particle shape, another parameter that can be easily tuned in the RIMS shear cell is the confining pressure. It is worth noting that, in fact, all studies presented in this thesis are performed under constant pressure conditions, allowing for small fluctuations in volume fraction. Granular materials that are shear-driven while under some externally applied load have been explored in other systems [69, 134]. In experimental systems, the full effects of confining pressure on particle-scale motion within the granular material have not been explored.

We have performed initial experiments using PMMA plates that are cut to fit the shear cell and lay directly on top of the granular material, exerting a downward pressure that pushes grains closer together. This way of introducing pressure is analogous to increasing the pile height, the kinematics of which have been explored previously in the split-bottom geometry [103]. However, this method of pressure loading is unique in that granular force chains terminate at an effectively constant height where the load is applied, and is felt uniformly by the top layer.

In these experiments, three plates of varying thickness were considered, each

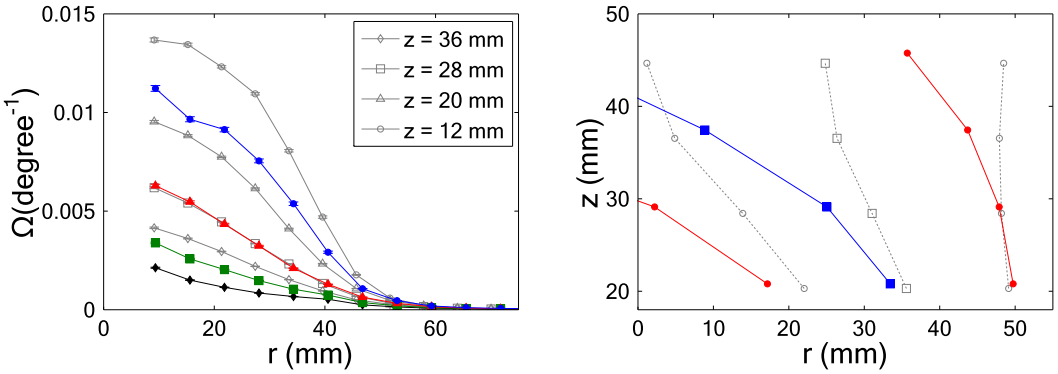

Figure 7.3: (Left) Primary (azimuthal) flow profiles of the granular material at various heights within the pile with a free surface (gray,open symbols) and with a 303 g load (colored,closed symbols). Since the applied shear is quasistatic, the angular velocity is not reported per time, but rather per angular displacement of the disk. (Right) The center (squares) and edges (circles) of the shear zone for the free surface with no load (gray,open symbols) and with the 303 g load (colored,closed symbols).

designed to weigh about 0.5, 1.0, and 1.5 times the total weight of the granular material. For a pile height of 45 mm, the block masses were measured to be 303, 626, and 933 g. With a single block in place at a time, quasistatic shear was applied in a constant direction.

As expected from previous results in the split-bottom geometry, the shear zone closes in on itself at lower heights when pressure is applied, as shown in Figure 7.3. This can also be seen in the suppression of primary flow profiles to the point where an error function can no longer faithfully represent the average azimuthal flow in the vicinity of the applied load. At the same time, confining pressure also appears

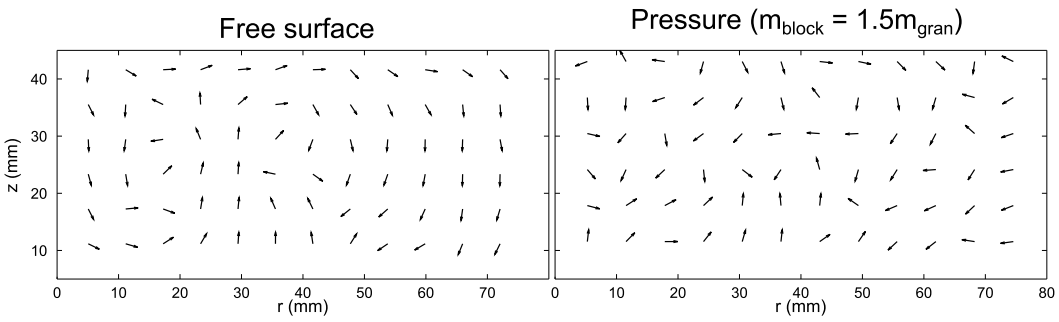

Figure 7.4: An illustration of the secondary flow profile under no load (Left) and a 966 g load (Right). In this figure, arrows are drawn with a constant length to highlight the profile shape.

to have a dampening affect on the convective secondary flow profile. As illustrated in Figure 7.4, the free surface case demonstrates clear convective rolls, reminiscent of those shown in chapter 3. When pressure is applied, these flows no longer exhibit any significant vorticity, suggesting that the presence of pressure can affect not only length scales for irreversibility, but also segregation rates and the driving length scales at which segregation can occur. Future studies can also look to this kind of pressure loading as a way of altering the force fabric of the material, thereby perhaps affecting characteristics of particle-scale rotational motion.

7.3 Particle Friction

Experimentally, interparticle particle friction can easily be altered by using grains of a different material. However, in order to effectively use the RIMS system for acquiring 3D images, one would need to make further adjustments to the system. In all likelihood, a new material would have to match refractive index with a new

fluid. In determining a new material and fluid combination, one would also have to be mindful of the chemical compatibility, much less the physical effect the fluid has on the motion of the grains.

Alternatively, the same material can be used with particle etching as a way of altering the surface roughness of each grain [135]. If particle etching can be done in such a way as to change the surface roughness without altering the optical properties of the material, this would afford the opportunity to use RIMS to easily study a wide effective coefficients of friction.

The simulations described in this thesis were performed using frictionless grains, so there was no tangential force to the grains to exert on each other. However, interparticle friction is a feature that could be added into the simulations, providing this additional force to consider when the system updates, much less reaches a stable initial packing.

With friction built into the simulation, the grains could exert torques on each other, which can lead to the onset of rotational motion if they are unbalanced. On the other hand, if the packing is stable, such as at the beginning of the simulation, each grain must feel balanced torques from its nearest neighborhoods. In either case, a "rotational network" that characterizes rotational motion and torques exerted between grains could, for instance, indicate the role of collective and/or frustrated rotations in the cage-breaking nature of motion.

Bibliography

[1] C.-h. Liu, S. R. Nagel, D. A. Schecter, S. N. Coppersmith, S. Majumdar, O. Narayan, and T. A. Witten. Force fluctuations in bead packs. *Science*, 269:513–515, Jul 1995.

[2] Eric Hand. Ten new rosetta images that reveal comet 67p in all its glory. *Science News*, Jan 2015.

[3] J. F. Kennedy. The formation of sediment ripples, dunes, and antidunes. *Annu. Rev. Fluid Mech.*, 1(1):147–168, 1969.

[4] Heinrich M. Jaeger, Sidney R. Nagel, and Robert P. Behringer. Granular solids, liquids, and gases. *Rev. Mod. Phys.*, 68:1259–1273, Oct 1996.

[5] T Pähtz, H. J. Herrmann, and T. Shinbrot. Why do particle clouds generate electric charges? *Nature Phys.*, 6:364–368, May 2010.

[6] Andrea J. Liu and Sidney R. Nagel. Nonlinear dynamics: Jamming is not just cool anymore. *Nature*, 396:21–22, Nov 1998.

[7] Dapeng Bi, Jie Zhang, Bulbul Chakraborty, and R.P. Behringer. Jamming by shear. *Nature*, 480:355–358, Dec 2011.

[8] J. M. Ottino and D. V. Khakhar. Mixing and segregation of granular materials. *Annu. Rev. Fluid Mech.*, 32(1):55–91, 2000.

[9] Anthony Rosato, Katherine J. Strandburg, Friedrich Prinz, and Robert H. Swendsen. Why the brazil nuts are on top: Size segregation of particulate matter by shaking. *Phys. Rev. Lett.*, 58:1038–1040, Mar 1987.

[10] James B. Knight, H. M. Jaeger, and Sidney R. Nagel. Vibration-induced size separation in granular media: The convection connection. *Phys. Rev. Lett.*, 70:3728–3731, Jun 1993.

[11] Hideaki Miyamoto, Hajime Yano, Daniel J. Scheeres, Shinsuke Abe, Olivier Barnouin-Jha, Andrew F. Cheng, Hirohide Demura, Robert W. Gaskell, Naru Hirata, Masateru Ishiguro, Tatsuhiro Michikami, Akiko M. Nakamura, Ryosuke Nakamura, Jun Saito, and Sho Sasaki. Regolith migration and sorting on asteroid itokawa. *Science*, 269:513–515, Jul 1995.

[12] J.M.N.T. Gray and A.R. Thornton. A theory for particle size segregation in shallow granular free-surface flows. *Proc. R. Soc. A*, 461:1447–1473, May 2005.

[13] S. B. Savage and C. K. K. Lun. Particle size segregation in inclined chute flow of dry cohesionless granular solids. *J. Fluid Mech.*, 189:311–335, Apr 1988.

[14] D.V. Khakhar, J.J. McCarthy, and J.M. Ottino. Radial segregation of granular mixtures in rotating cylinders. *Phys. Fluids*, 9:3600–3614, Dec 1997.

[15] Vicente Garzó and James W. Dufty. Hydrodynamics for a granular binary mixture at low density. *Phys. Fluids*, 14:1476–1490, Apr 2002.

[16] D.J. Pine, J.P. Gollub, J.F. Brady, and A.M. Leshansky. Chaos and threshold for irreversibility in sheared suspensions. *Nature*, 438:997, Dec 2005.

[17] Steven Slotterback, Mitch Mailman, Krisztian Ronaszegi, Martin van Hecke, Michelle Girvan, and Wolfgang Losert. Onset of irreversibility in cyclic shear of granular packings. *Phys. Rev. E*, 85:021309, Feb 2012.

[18] James B. Knight, Christopher G. Fandrich, Chun Ning Lau, Heinrich M. Jaeger, and Sidney R. Nagel. Density relaxation in a vibrated granular material. *Phys. Rev. E*, 51:3957–3963, May 1995.

[19] Patrick Richard, Mario Nicodemi, Renaud Delannay, Philippe Ribiére, and Daniel Bideau. Slow relaxation and compaction of granular systems. *Nature Mater.*, 4:121–128, Feb 2005.

[20] Juan Carlos Quezada, Gilles Saussine, Pierre Breul, and Farhang Radja. Predicting the settlement of coarse granular materials under vertical loading. *Sci. Rep.*, 4:5707, Jul 2014.

[21] Shlomo Havlin and Daniel Ben-Avraham. Diffusion in disordered media. *Adv. Phys.*, 36(6):695–798, 1987.

[22] L. Corté, P. M. Chaikin, J. P. Gollub, and D. J. Pine. Random organization in periodically driven systems. *Nature Physics*, 4:420–424, May 2008.

[23] G. Marty and O. Dauchot. Subdiffusion and cage effect in a sheared granular material. *Phys. Rev. Lett.*, 94:015701, Jan 2005.

[24] Ido Golding and Edward C. Cox. Physical nature of bacterial cytoplasm. *Phys. Rev. Lett.*, 96:098102, Mar 2006.

[25] Jedrzej Szymanski and Matthias Weiss. Elucidating the origin of anomalous diffusion in crowded fluids. *Phys. Rev. Lett.*, 103:038102, Jul 2009.

[26] G. Oron and H. J. Herrmann. Generalization of space-filling bearings to arbitrary loop size. *J. Phys. A: Math. Gen.*, 33(7):1417, Feb 2000.

[27] Thomas C. Halsey. Motion of packings of frictional grains. *Phys. Rev. E*, 80:011303, Jul 2009.

[28] Ali R. Hadjesfandiari and Gary F. Dargush. Couple stress theory for solids. *Int. J. Solids Struct.*, 48(18):2496 – 2510, Sep 2011.

[29] Charles S. Campbell. Boundary interactions for two-dimensional granular flows. part 1. flat boundaries, asymmetric stresses and couple stresses. *J. Fluid Mech.*, 247:111–136, Feb 1993.

[30] Michel Y. Louge. Role of couple stresses in shallow granular flows down a bumpy incline. *5th International Conference on Multiphase Flow, ICMF04*, 2004.

[31] Y. C. Fung. *A First Course in Continuum Mechanics*. Prentice-Hall, 3rd edition, Jul 1994.

[32] R. Blumenfeld, S.F. Edwards, and M. Schwartz. da vinci fluids, catch-up dynamics and dense granular flow. *Euro. Phys. J. E*, 32(4):333–338, Aug 2010.

[33] Yol Forterre and Olivier Pouliquen. Flows of dense granular media. *Annu. Rev. Fluid Mech.*, 40(1):1–24, Jan 2008.

[34] N. Huang, G. Ovarlez, F. Bertrand, S. Rodts, P. Coussot, and Daniel Bonn. Flow of wet granular materials. *Phys. Rev. Lett.*, 94:028301, Jan 2005.

[35] Ryan D. Maladen, Yang Ding, Chen Li, and Daniel I. Goldman. Undulatory swimming in sand: Subsurface locomotion of the sandfish lizard. *Science*, 325(5938):314–318, Jul 2009.

[36] Hiroaki Katsuragi and Douglas J. Durian. Unified force law for granular impact cratering. *Nature Physics*, 3(6):420–423, Jun 2007.

[37] Daniel Howell, R. P. Behringer, and Christian Veje. Stress fluctuations in a 2d granular couette experiment: A continuous transition. *Phys. Rev. Lett.*, 82:5241–5244, Jun 1999.

[38] Kiri Nichol and Karen E. Daniels. Equipartition of rotational and translational energy in a dense granular gas. *Phys. Rev. Lett.*, 108:018001, Jan 2012.

[39] M. Nakagawa, S.A. Altobelli, A. Caprihan, E. Fukushima, and E.-K. Jeong. Non-invasive measurements of granular flows by magnetic resonance imaging. *Exp. Fluids*, 16:54–60, Nov 1993.

[40] L.B. Wang, J.D. Frost, and J.S. Lai. Three-dimensional digital representation of granular material microstructure from x-ray tomography imaging. *J. Comput. Civ. Eng.*, 18:28–35, Jan 2004.

[41] Jasna Brujić, Sam F. Edwards, Ian Hopkinson, and Hernán A. Makse. Measuring the distribution of interdroplet forces in a compressed emulsion system. *Physica A*, 327(3-4):201 – 212, Sep 2003.

[42] Joshua A. Dijksman, Frank Rietz, Kinga A. Lőrincz, Martin van Hecke, and Wolfgang Losert. Invited article: Refractive index matched scanning of dense granular materials. *Rev. Sci. Instrum.*, 83:011301, Jan 2012.

[43] Joshua A. Dijksman, Elie Wandersman, Steven Slotterback, Christian R. Berardi, William Derek Updegraff, Martin van Hecke, and Wolfgang Losert. From frictional to viscous behavior: Three-dimensional imaging and rheology of gravitational suspensions. *Phys. Rev. E*, 82:060301, Dec 2010.

[44] K. N. Nordstrom, E. Lim, M. Harrington, and W. Losert. Granular dynamics during impact. *Phys. Rev. Lett.*, 112:228002, Jun 2014.

[45] Steven Slotterback. *Particle Motion in Granular Materials: Three Dimensional Imaging of Slow Flows and Compaction.* PhD thesis, University of Maryland, 2012.

[46] Denis Fenistein and Martin van Hecke. Kinematics: Wide shear zones in granular bulk flow. *Nature*, 425(6955):256, Sep 2003.

[47] Denis Fenistein, Jan Willem van de Meent, and Martin van Hecke. Universal and wide shear zones in granular bulk flow. *Phys. Rev. Lett.*, 92:094301, Mar 2004.

[48] John C. Crocker and David G. Grier. Methods of digital video microscopy for colloidal studies. *J. Colloid. Interf. Sci.*, 179:298–310, Apr 1996.

[49] Nicholas T. Ouellette, Haitao Xu, and Eberhard Bodenschatz. A quantitative study of three-dimensional lagrangian particle tracking algorithms. *Exp. Fluids*, 40:301–313, Feb 2006.

[50] Anita Mehta and S.F. Edwards. Statistical mechanics of powder mixtures. *Physica A*, 157(3):1091–1100, Jun 1989.

[51] Frank L. DiMaggio and Ivan S. Sandler. Material model for granular soils. *J. Energ. Div.-ASCE*, 97(3):935–950, May 1971.

[52] M.A. Goodman and S.C. Cowin. A continuum theory for granular materials. *Arch. Rational Mech. Anal.*, 44(4):249–266, Jan 1972.

[53] David L. Henann and Ken Kamrin. A predictive, size-dependent continuum model for dense granular flows. *Proceedings of the National Academy of Sciences*, 110(17):6730–6735, Apr 2013.

[54] Per Bak, Chao Tang, and Kurt Wiesenfeld. Self-organized criticality: An explanation of the $1/f$ noise. *Phys. Rev. Lett.*, 59:381–384, Jul 1987.

[55] Per Bak, Chao Tang, and Kurt Wiesenfeld. Self-organized criticality. *Phys. Rev. A*, 38:364–374, Jul 1988.

[56] G. William Baxter and R. P. Behringer. Cellular automata models of granular flow. *Phys. Rev. A*, 42:1017–1020, Jul 1990.

[57] G. William Baxter and R.P. Behringer. Cellular automata models for the flow of granular materials. *Physica D*, 51(13):465–471, Aug 1991.

[58] P.A. Cundall and O.D.L. Strack. A discrete numerical model for granular assemblies. *Geotechnique*, 29(1):47–65, Mar 1979.

[59] Y. Tsuji, T. Kawaguchi, and T. Tanaka. Discrete particle simulation of two-dimensional fluidized bed. *Powder Technol.*, 77(1):79–87, Oct 1993.

[60] Yu Wang and Matthew T. Mason. Two-dimensional rigid-body collisions with friction. *J. Appl. Mech.*, 59(3):635–642, Sep 1992.

[61] Ning Xu, Jerzy Blawzdziewicz, and Corey S. O'Hern. Random close packing revisited: Ways to pack frictionless disks. *Phys. Rev. E*, 71:061306, Jun 2005.

[62] William H. Press, Saul A. Teukolsky, William T. Vetterling, and Brian P. Flannery. *Numerical Recipes in C++: The Art of Scientific Computing*. Cambridge University Press, 2nd edition, Feb 2002.

[63] A. W. Lees and S. F. Edwards. The computer study of transport processes under extreme conditions. *J. Phys. C: Solid State Phys.*, 5:1921, Aug 1972.

[64] William C. Swope, Hans C. Andersen, Peter H. Berens, and Kent R. Wilson. A computer simulation method for the calculation of equilibrium constants for the formation of physical clusters of molecules: Application to small water clusters. *J. Chem. Phys.*, 76(1):637–649, 1982.

[65] J. Duran, J. Rajchenbach, and E. Clément. Arching effect model for particle size segregation. *Phys. Rev. Lett.*, 70:2431–2434, Apr 1993.

[66] J.M.N.T. Gray and K. Hutter. Pattern formation in granular avalanches. *Contin. Mech. Thermodyn.*, 9:341–345, Dec 1997.

[67] Nitin Jain, Julio M. Ottino, and Richard M. Lueptow. Combined size and density segregation and mixing in noncircular tumblers. *Phys. Rev. E*, 71:051301, May 2005.

[68] Christopher R.J. Charles, Zeina S. Khan, and Stephen W. Morris. Pattern scaling in axial segregation. *Gran. Matt.*, 8:1–3, Mar 2006.

[69] Laura A. Golick and Karen E. Daniels. Mixing and segregation rates in sheared granular materials. *Phys. Rev. E*, 80:042301, Oct 2009.

[70] Yi Fan and K. M. Hill. Shear-driven segregation of dense granular mixtures in a split-bottom cell. *Phys. Rev. E*, 81:041303, Apr 2010.

[71] Lindsay B. H. May, Laura A. Golick, Katherine C. Phillips, Michael Shearer, and Karen E. Daniels. Shear-driven size segregation of granular materials: Modeling and experiment. *Phys. Rev. E*, 81:051301, May 2010.

[72] Yi Fan and K M Hill. Theory for shear-induced segregation of dense granular mixtures. *New J. Phys.*, 13(9):095009, Sep 2011.

[73] R. Khosropour, Jessie Zirinsky, H. K. Pak, and R. P. Behringer. Convection and size segregation in a couette flow of granular material. *Phys. Rev. E*, 56:4467–4473, Oct 1997.

[74] S. Dippel and S. Luding. Simulations on size segregation: Geometrical effects in the absence of convection. *J. Phys. I (France)*, 5:1527–1537, Dec 1995.

[75] L. Kondic and R. P. Behringer. Elastic energy, fluctuations and temperature for granular materials. *Europhys. Lett.*, 67(2):205, Jul 2004.

[76] J.-C. Tsai and J. P. Gollub. Slowly sheared dense granular flows: Crystallization and nonunique final states. *Phys. Rev. E*, 70(3):031303, Sep 2004.

[77] M. Herrera, S. McCarthy, S. Slotterback, E. Cephas, W. Losert, and M. Girvan. Path to fracture in granular flows: Dynamics of contact networks. *Phys. Rev. E*, 83:061303, Jun 2011.

[78] N. Murdoch, B. Rozitis, K. Nordstrom, S. F. Green, P. Michel, T.-L. de Lophem, and W. Losert. Granular convection in microgravity. *Phys. Rev. Lett.*, 110:018307, Jan 2013.

[79] Anthony Thornton, Thomas Weinhart, Stefan Luding, and Onno Bokhove. Modeling of particle size segregation: Calibration using the discrete particle method. *Int. J. Mod. Phys. C*, 23:1240014, Aug 2012.

[80] Ken Kamrin and Georg Koval. Nonlocal constitutive relation for steady granular flow. *Phys. Rev. Lett.*, 108:178301, Apr 2012.

[81] J. Zhang, T. Majmudar, A. Tordesillas, and R. Behringer. Statistical properties of a 2d granular material subjected to cyclic shear. *Granular Matter*, 12:159–172, Mar 2010.

[82] Micah Lundberg, Kapilanjan Krishan, Ning Xu, Corey S. O'Hern, and Michael Dennin. Reversible plastic events in amorphous materials. *Phys. Rev. E*, 77:041505, Apr 2008.

[83] Nathan C. Keim and Sidney R. Nagel. Generic transient memory formation in disordered systems with noise. *Phys. Rev. Lett.*, 107:010603, Jun 2011.

[84] Guo-Jie Gao, Jerzy Blawzdziewicz, and Corey S. O'Hern. Geometrical families of mechanically stable granular packings. *Phys. Rev. E*, 80:061303, Dec 2009.

[85] D. J. Durian. Foam mechanics at the bubble scale. *Phys. Rev. Lett.*, 75:4780–4783, Dec 1995.

[86] Xavier García and Ernesto Medina. Strong-weak network anisotropy switching and hysteresis in three-dimensional granular materials. *Phys. Rev. E*, 78:021305, Aug 2008.

[87] N. W. Watkins, D. Credgington, R. Sanchez, S. J. Rosenberg, and S. C. Chapman. Kinetic equation of linear fractional stable motion and applications to modeling the scaling of intermittent bursts. *Phys. Rev. E*, 79:041124, Apr 2009.

[88] Paolo Allegrini, Jack F. Douglas, and Sharon C. Glotzer. Dynamic entropy as a measure of caging and persistent particle motion in supercooled liquids. *Phys. Rev. E*, 60:5714–5724, Nov 1999.

[89] Ralf Metzler and Joseph Klafter. The random walk's guide to anomalous diffusion: a fractional dynamics approach. *Physics Reports*, 339(1):1 – 77, Dec 2000.

[90] Eric R. Weeks, J. C. Crocker, Andrew C. Levitt, Andrew Schofield, and D. A. Weitz. Three-dimensional direct imaging of structural relaxation near the colloidal glass transition. *Science*, 287(5453):627–631, 2000.

[91] Avi Caspi, Rony Granek, and Michael Elbaum. Enhanced diffusion in active intracellular transport. *Phys. Rev. Lett.*, 85:5655–5658, Dec 2000.

[92] Marcin Magdziarz, Aleksander Weron, Krzysztof Burnecki, and Joseph Klafter. Fractional brownian motion versus the continuous-time random walk: A simple test for subdiffusive dynamics. *Phys. Rev. Lett.*, 103:180602, Oct 2009.

[93] G. T. Seidler, G. Martinez, L. H. Seeley, K. H. Kim, E. A. Behne, S. Zaranek, B. D. Chapman, S. M. Heald, and D. L. Brewe. Granule-by-granule reconstruction of a sandpile from x-ray microtomography data. *Phys. Rev. E*, 62:8175–8181, Dec 2000.

[94] T. Aste, M. Saadatfar, and T. J. Senden. Geometrical structure of disordered sphere packings. *Phys. Rev. E*, 71:061302, Jun 2005.

[95] J. Zhou, S. Long, Q. Wang, and A. D. Dinsmore. Measurement of forces inside a three-dimensional pile of frictionless droplets. *Science*, 312(5780):1631–1633, Jun 2006.

[96] Patrick Richard, Pierre Philippe, Fabrice Barbe, Stéphane Bourlès, Xavier Thibault, and Daniel Bideau. Analysis by x-ray microtomography of a granular packing undergoing compaction. *Phys. Rev. E*, 68:020301, Aug 2003.

[97] Steven Slotterback, Masahiro Toiya, Leonard Goff, Jack F. Douglas, and Wolfgang Losert. Correlation between particle motion and voronoi-cell-shape fluctuations during the compaction of granular matter. *Phys. Rev. Lett.*, 101:258001, Dec 2008.

[98] K. Sakaie, D. Fenistein, T. J. Carroll, M. van Hecke, and P. Umbanhowar. Mr imaging of reynolds dilatancy in the bulk of smooth granular flows. *Europhys. Lett.*, 84(3):38001, Nov 2008.

[99] Tamás Börzsönyi, Balázs Szabó, Gábor Törös, Sandra Wegner, János Török, Ellák Somfai, Tomasz Bien, and Ralf Stannarius. Orientational order and alignment of elongated particles induced by shear. *Phys. Rev. Lett.*, 108:228302, May 2012.

[100] Sandra Wegner, Tamás Börzsönyi, Tomasz Bien, Georg Rose, and Ralf Stannarius. Alignment and dynamics of elongated cylinders under shear. *Soft Matter*, 8:10950–10958, Nov 2012.

[101] E. E. Ehrichs, H. M. Jaeger, Greg S. Karczmar, James B. Knight, Vadim Yu. Kuperman, and Sidney R. Nagel. Granular convection observed by magnetic resonance imaging. *Science*, 267(5204):1632–1634, Mar 1995.

[102] N. Huang, G. Ovarlez, F. Bertrand, S. Rodts, P. Coussot, and Daniel Bonn. Flow of wet granular materials. *Phys. Rev. Lett.*, 94:028301, Jan 2005.

[103] Xiang Cheng, Jeremy B. Lechman, Antonio Fernandez-Barbero, Gary S. Grest, Heinrich M. Jaeger, Greg S. Karczmar, Matthias E. Möbius, and Sidney R. Nagel. Three-dimensional shear in granular flow. *Phys. Rev. Lett.*, 96:038001, Jan 2006.

[104] Elie Wandersman, Joshua A. Dijksman, and Martin van Hecke. Particle diffusion in slow granular bulk flows. *Euro. Phys. Lett.*, 100:38006, Nov 2012.

[105] K. M. Hill, A. Caprihan, and J. Kakalios. Bulk segregation in rotated granular material measured by magnetic resonance imaging. *Phys. Rev. Lett.*, 78:50–53, Jan 1997.

[106] Patrice Porion, Nathalie Sommier, Anne-Marie Faugère, and Pierre Evesque. Dynamics of size segregation and mixing of granular materials in a 3d-blender by nmr imaging investigation. *Powder Technol.*, 141(1 - 2):55 – 68, Mar 2004.

[107] Matt Harrington, Joost H. Weijs, and Wolfgang Losert. Suppression and emergence of granular segregation under cyclic shear. *Phys. Rev. Lett.*, 111:078001, Aug 2013.

[108] K. Harth, U. Kornek, T. Trittel, U. Strachauer, S. Höme, K. Will, and R. Stannarius. Granular gases of rod-shaped grains in microgravity. *Phys. Rev. Lett.*, 110:144102, Apr 2013.

[109] N. V. Brilliantov, T. Pöschel, W. T. Kranz, and A. Zippelius. Translations and rotations are correlated in granular gases. *Phys. Rev. Lett.*, 98:128001, Mar 2007.

[110] JP Bardet. Observations on the effects of particle rotations on the failure of idealized granular materials. *Mech. Mater.*, 18(2):159–182, Jul 1994.

[111] Kazuyoshi Iwashita and Masanobu Oda. Rolling resistance at contacts in simulation of shear band development by dem. *J. Eng. Mech.*, 124(3):285–292, Mar 1998.

[112] S. Luding. The effect of friction on wide shear bands. *Part. Sci. Tech.*, 26(1):33–42, Mar 2007.

[113] Masanobu Oda, Junichi Konishi, and Siavouche Nemat-Nasser. Experimental micromechanical evaluation of strength of granular materials: Effects of particle rolling. *Mech. Mater.*, 1(4):269 – 283, Dec 1982.

[114] Tamás Börzsönyi, Balázs Szabó, Sandra Wegner, Kirsten Harth, János Török, Ellák Somfai, Tomasz Bien, and Ralf Stannarius. Shear-induced alignment and dynamics of elongated granular particles. *Phys. Rev. E*, 86:051304, Nov 2012.

[115] C. K. K. Lun and A. A. Bent. Numerical simulation of inelastic frictional spheres in simple shear flow. *Journal of Fluid Mechanics*, 258:335–353, Jan 1994.

[116] Frédéric da Cruz, Sacha Emam, Michaël Prochnow, Jean-Noël Roux, and Fran çois Chevoir. Rheophysics of dense granular materials: Discrete simulation of plane shear flows. *Phys. Rev. E*, 72:021309, Aug 2005.

[117] Jie Zhang, Robert P. Behringer, and Isaac Goldhirsch. Coarse-graining of a physical granular system. *Progress of Theoretical Physics Supplement*, 184:16–30, Mar 2010.

[118] L. Euler. Formulae generales pro translatione quacunque corporum rigidorum. *Novi Commentarii academiae scientiarum Petropolitanae*, 20:189–207, 1776.

[119] Herbert Goldstein, Charles P. Poole, and John L. Safko. *Classical Mechanics*. Addison-Wesley, 3rd edition, Jun 2001.

[120] J.J. Sakurai. *Modern Quantum Mechanics*. Addison-Wesley, revised edition, Sep 1993.

[121] Guy G. Marcus, Shima Parsa, Stefan Kramel, Rui Ni, and Greg A. Voth. Measurements of the solid-body rotation of anisotropic particles in 3d turbulence. *New J. Phys.*, 16:102001, Oct 2014.

[122] Robert Zimmermann, Yoann Gasteuil, Mickael Bourgoin, Romain Volk, Alain Pumir, and Jean-Franois Pinton. Tracking the dynamics of translation and absolute orientation of a sphere in a turbulent flow. *Rev. Sci. Instrum.*, 82:033906, Mar 2011.

[123] Wolfgang Kabsch. A solution for the best rotation to relate two sets of vectors. *Acta Crystallogr. A*, 32:922–923, Sep 1976.

[124] Wolfgang Kabsch. A discussion of the solution for the best rotation to relate two sets of vectors. *Acta Crystallogr. A*, 34:827–828, Sep 1978.

[125] S. Umeyama. Least-squares estimation of transformation parameters between two point patterns. *IEEE Trans. Pattern Anal. Mach. Intell.*, 13(4):376–380, Apr 1991.

[126] Kelly L. Damm and Heather A. Carlson. Gaussian-weighted {RMSD} superposition of proteins: A structural comparison for flexible proteins and predicted protein structures. *Biophys. J.*, 90(12):4558 – 4573, Jun 2006.

[127] Marc Z. Miskin and Heinrich M. Jaeger. Adapting granular materials through artificial evolution. *Nature Mater.*, 12(4):326–331, Apr 2013.

[128] Peter Scholz, Ilko Reuter, and Dirk Heitmann. Piv measurements of the flow through an intake port using refractive index matching. In *16th International Symposium on Applications of Laser Techniques to Fluid Mechanics*, Jul 2012.

[129] Tamás Börzsönyi and Ralf Stannarius. Granular materials composed of shape-anisotropic grains. *Soft Matter*, Aug 2013.

[130] Jennifer Galanis, Daniel Harries, Dan L. Sackett, Wolfgang Losert, and Ralph Nossal. Spontaneous patterning of confined granular rods. *Phys. Rev. Lett.*, 96:028002, Jan 2006.

[131] Jennifer Galanis, Ralph Nossal, Wolfgang Losert, and Daniel Harries. Nematic order in small systems: Measuring the elastic and wall-anchoring constants in vibrofluidized granular rods. *Phys. Rev. Lett.*, 105:168001, Oct 2010.

[132] Aleksandar Donev, Ibrahim Cisse, David Sachs, Evan A. Variano, Frank H. Stillinger, Robert Connelly, Salvatore Torquato, and P. M. Chaikin. Improving the density of jammed disordered packings using ellipsoids. *Science*, 303(5660):990–993, Feb 2004.

[133] Ali Mohraz and Michael J Solomon. Direct visualization of colloidal rod assembly by confocal microscopy. *Langmuir*, 21(12):5298–5306, 2005.

[134] Thallak G. Sitharam. Micromechanical modeling of granular materials: effect of confining pressure on mechanical behavior. *Mech. Mater.*, 31(10):653–665, Oct 1999.

[135] Daniel L. Blair, Nathan W. Mueggenburg, Adam H. Marshall, Heinrich M. Jaeger, and Sidney R. Nagel. Force distributions in three-dimensional granular assemblies: Effects of packing order and interparticle friction. *Phys. Rev. E*, 63:041304, Mar 2001.